MICROSTRUCTURAL ANALYSIS AND EVALUATION OF W AND W/W_2C COMPOSITES FOR FUSION APPLICATION

Andreja Šestan Zavašnik

Doctoral Dissertation
Jožef Stefan International Postgraduate School
Ljubljana, Slovenia

Supervisor: Prof. Dr. Miran Čeh, Jožef Stefan International Postgraduate School and Jožef Stefan Institute, Ljubljana, Slovenia
Co-Supervisor: Prof. Dr. Saša Novak, Jožef Stefan International Postgraduate School and Jožef Stefan Institute, Ljubljana, Slovenia

Evaluation Board:
Prof. Dr. Goran Dražić, Chair, Jožef Stefan International Postgraduate School and National Institute of Chemistry, Ljubljana, Slovenia
Prof. Dr. Boštjan Markoli, Member, Faculty of Natural Sciences and Engineering, University of Ljubljana, Slovenia
Prof. Dr. Wofgang Pantleon, Member, DTU Mechanical Engineering, Department of Mechanical Engineering, Section of Materials and Surface Engineering, Technical University of Denmark, Denmark
Dr. Aleksander Kostka, Institute for Materials Ruhr-Universität Bochum, Germany

MEDNARODNA PODIPLOMSKA ŠOLA JOŽEFA STEFANA
JOŽEF STEFAN INTERNATIONAL POSTGRADUATE SCHOOL

Andreja Šestan Zavašnik

MICROSTRUCTURAL ANALYSIS AND EVALUATION OF W AND W/W$_2$C COMPOSITES FOR FUSION APPLICATION

Doctoral Dissertation

MIKROSTRUKTURNA ANALIZA IN OCENA KOMPOZITOV W IN W/W$_2$C ZA UPORABO V FUZIJI

Doktorska disertacija

Supervisor: Prof. Dr. Miran Čeh

Co-Supervisor: Prof. Dr. Saša Novak

Ljubljana, Slovenia, June 2022

To my beloved family and friends.

Acknowledgements

I want to express my gratitude to my supervisors, Prof. Dr. Miran Čeh and Prof. Dr. Saša Novak, for their guidance, help and support during my PhD study. Thanks for your help, support, ideas and discussions during my doctoral study. At the same time, I would like to thank my co-supervisor, Prof. Dr. Saša Novak, for the guidance at work and for introducing me to the world of fusion. Thank you for including me in the Eurofusion education & training scheme.

This work has been carried out within the framework of the EURO-fusion Consortium and has received funding from the Euratom research and training programme 2014–2018 and 2019–2020 under grant agreement No. 633053. The views and opinions expressed herein do not necessarily reflect those of the European Commission. This research has also received funding from the Slovenian Research Agency (Contracts No. 1000-17-0106, J2-8165, P2-0087 and P2-0405).

During my PhD, I was given an opportunity to spend one year at Max-Planck-Institut für Eisenforschung in Düsseldorf, Germany, as a part of the student mobility for traineeship within the Erasmus^{+} Programme. I would like to thank Prof. Dr. Dehm's group for the hospitality during my stay and the wonderful research experience. Thanks also go to fusion group members of the Department for Nanostructured materials and the Department of Low and Medium Energy Physics at the Jožef Stefan Institute, especially Dr. Sabina Markelj, for research support and shared knowledge and expertise. I would like to thank Dr. Barbara Batič for the pleasant education on the EBSD technique.

Finally, the greatest thank you goes to my family and friends for all the support during my study, the encouraging words and the unwavering trust in me.

Abstract

Fusion technology has a great potential to safely provide an inexhaustible quantity of electricity without producing greenhouse gases and minimal hazardous waste compared to conventional energy sources, such as nuclear power plants. For materials intended for fusion plasma-facing applications, the essential properties are structural stability at elevated temperature, adequate thermal conductivity, strength and ductility, thermal shock and thermal fatigue resistance, and stability under neutron exposure. For such applications, tungsten and tungsten-based materials are a reasonable choice due to their advantageous combination of physical properties.

This thesis introduces three research topics with one common denominator – microstructure analysis of tungsten and tungsten-based materials developed by the Slovenian research group within the European Fusion Programme. The first research topic relates to my first-author scientific article entitled "*The role of tungsten phases formation during tungsten metal powder consolidation by FAST: Implications for high-temperature application*". In the article, my co-authors and I have explored and utilised the research methods appropriate for the microstructure analysis of tungsten consolidated by field-assisted sintering technology (FAST). In the study, *in-situ* secondary phases formation after consolidation was analysed and identified as tungsten dioxide (WO_2). The presence of oxide inclusions motivated us to explore the role of tungsten carbide (WC) as an oxygen binder for removing the oxide impurities from the tungsten matrix, as described in my second first-author scientific article entitled "*Tungsten carbide as a deoxidation agent for plasma-facing tungsten-based materials*". To completely remove the oxygen impurities and obtain a pure tungsten body, we have to introduce a minimum of 5.8 - 8.8 vol % WC as a carbon source to the initial mixture. Determined from stoichiometry calculations, the oxygen is removed in the form of carbon monoxide and carbon dioxide.

A surplus amount of WC will lead to the *in-situ* formation of a thermally stable ε-W_2C as a secondary phase in the tungsten matrix. The presence of ε-W_2C phase can influence the performance of plasma-facing materials under irradiation, which my co-authors and I experimentally explored in my third first-author article entitled "*Non-uniform He bubble formation in W/W_2C composite: Experimental and ab-initio study*", exploring the influence of helium on the microstructure of the multi-phase material, i.e., W/W_2C composite described in my previous articles. The experimental observations of helium bubble formation in the W/W_2C composite were complemented by first-principles-based density functional theory (DFT) calculations to establish a fundamental understanding of helium clustering, migration and dissolution in tungsten metal and tungsten carbide, W_2C. The study deduces that helium will be preferentially trapped by large structural defects, which in the end, severely affect the material integrity for plasma-facing applications.

Povzetek

Jedrsko zlivanje ali fuzija ima visok potencial zagotoviti varen in praktično neizčrpen vir električne energije brez nastajanja toplogrednih plinov in, v primerjavi s konvencionalnimi viri energije, kot so jedrske elektrarne, z zanemarljivo količino nevarnih odpadkov. Za materiale, ki so namenjeni za uporabo v stiku s fuzijsko plazmo, so bistvene lastnosti strukturna stabilnost pri povišani temperaturi, ustrezna toplotna prevodnost, trdnost in žilavost, odpornost na toplotni udar in toplotno utrujenost ter stabilnost pri izpostavljenosti nevtronom. Za takšno uporabo so volfram in materiali na osnovi volframa razumna izbira zaradi njihove ugodne kombinacije fizikalnih lastnosti.

Doktorsko delo obsega tri raziskovalne teme z enim skupnim imenovalcem–mikrostrukturno analizo volframa in materialov na osnovi volframa, ki jih je razvila slovenska raziskovalna skupina v okviru programa EUROfusion. Prva raziskovalna tema se nanaša na moj prvi avtorski znanstveni članek z naslovom »*The role of tungsten phases formation during tungsten metal powder consolidation by FAST: Implications for high-temperature application*«. V članku sem s soavtorji raziskala in uporabila raziskovalne metode, ki so primerne za analizo mikrostrukture volframa, zgoščenega s tehnologijo sintranja s pomočjo električnega polja (FAST). V študiji smo analizirali *in-situ* nastanek sekundarnih faz in jih identificirali kot volframov dioksid (WO_2). Prisotnost oksidnih vključkov nas je motivirala za raziskovanje vloge volframovega karbida (WC) za odstranjevanje oksidnih nečistoč iz volframove matrice, kot je opisano v drugem znanstvenem članku z naslovom »*Tungsten carbide as a deoxidation agent for plasma-facing tungsten-based materials*«. Najmanj 5.8–8.8 vol % WC kot vira ogljika je potrebno v začetno mešanico prahov vnesti, da se oksidne nečistoče med sintranjem popolnoma odstranijo kot ogljikov monoksid in ogljikov dioksid, da dobimo čisto volframovo matrico. Presežna količina WC povzroči *in-situ* nastanek termično stabilnega ε-W_2C kot sekundarne faze v volframovi matrici. Prisotnost ε-W_2C faze lahko vpliva na stabilnost materialov, izpostavljenih obsevanju, kar sem skupaj s soavtorji eksperimentalno raziskala v svojem tretjem članku z naslovom »*Non-uniform He bubble formation in W/W_2C composite: Experimental and ab-initio study*”. V članku je predstavljen vpliv helija na mikrostrukturo večfaznega kompozita W/W_2C, ki je bil raziskan v predhodnih znanstvenih člankih. Eksperimentalna opazovanja nastanka helijevih mehurčkov v kompozitu W/W_2C so nadgrajena s kvantokemijskimi simulacijami po teoriji gostotnega funkcionala (DFT), da bi vzpostavili temeljno razumevanje združevanja, migracije in raztapljanja helija v kovinskem volframu in keramičnem W_2C. Rezultati študije kažejo, da se helij prednostno ujame na velike strukturne napake, kar na koncu močno vpliva na celovitost materiala.

Contents

List of Figures

List of Tables

Abbreviations

bcc	. . .	Body-Centred Cubic
DBTT	. . .	Ductile-to-Brittle Transition Temperature
DFT	. . .	Density Functional Theory
DTA/TG	. . .	Differential Thermal Analysis / Thermogravimetric Analysis
e.g.	. . .	exempli gratia – for example
EBSD	. . .	Electron Backscatter Diffraction
EDXS or EDS	. . .	Energy Dispersive X-ray Spectroscopy
ELMs	. . .	Edge-Localised Modes
FAST	. . .	Field-Assisted Sintering Technology
fcc	. . .	Face-Centred Cubic
FEG-SEM	. . .	Field-Emission Gun Scanning Electron Microscope
FIB	. . .	Focused-Ion-Beam Scanning Electron Microscope
GB	. . .	Grain Boundary
HAADF	. . .	High-Angle Annular Dark-Field Detector
hcp	. . .	Hexagonal Close-Packed
HIs	. . .	Hydrogen Isotopes
i.e.	. . .	id est - that is
LLFPs	. . .	Long-Lived Fission Products
PFCs	. . .	Plasma-Facing Components
PFMs	. . .	Plasma-Facing Materials
S/TEM	. . .	Scanning Transmission Electron Microscope/microscopy
SEM	. . .	Scanning Electron Microscope/microscopy
TEM	. . .	Transmission Electron Microscope / microscopy
XRD	. . .	X-ray Diffraction Analysis

Symbols

[ ]	. . .	crystal plane directions; lattice vectors
°	. . .	degree symbol
a	. . .	unit cell parameter
appm	. . .	atomic parts per million
at.%	. . .	atomic percent
b	. . .	unit cell parameter
c	. . .	unit cell parameter
K	. . .	kelvin
kV	. . .	kilovolt
MeV	. . .	mega electron volt
nm	. . .	unit of length in the metric system (nanometre)
mbar	. . .	metric unit of pressure
ppm	. . .	parts per million
Tmelt	. . .	melting point
vol. %	. . .	Volume percent
wt. %	. . .	weight percent
α	. . .	alpha
β	. . .	beta
ε	. . .	epsilon
γ	. . .	gamma

Chemical Symbols

$(NH4)_2WO_4$	...	Ammonium paratungstate
Ar	...	Argon
C	...	Carbon
D	...	Deuterium
Fe	...	Iron
Ga	...	Gallium
He	...	Helium
n	...	neutron
N	...	Nitrogen
O	...	Oxygen
p	...	proton
Si	...	Silicon
T	...	Tritium
TaC	...	Tantalum Carbide
Ti	...	Titanium
TiC	...	Titanium Carbide
V	...	Vanadium
W	...	Tungsten
$W_{18}O_{49}$	...	Tungsten oxide
$W_{24}O_{68}$	...	Tungsten oxide
W_2C	...	Tungsten Carbide
WC	...	Tungsten Carbide
W_nO_{3n-1}	...	Tungsten oxide with atoms in the ratio n:3(n-1)
W_nO_{3n-2}	...	Tungsten oxide with atoms in the ratio n:3(n-1)
WO_2	...	Tungsten (IV) oxide
WO_3	...	Tungsten (VI) oxide
Y	...	Yttrium
α	...	alpha particle

Chapter 1

Introduction

Regardless of the material synthesis, consolidation method, or pre- and post-processing, thorough material characterisation is a fundamental research step in condensed matter research. Based on the results of such investigation, we can investigate and conclude on the material appropriateness for the intended application and overall performance of such materials. By careful interpretation of the material characterisation results, the manufacturing and modification step of the material treatment can be further optimised. The appropriate research methods can be selected, performed, and interpreted to obtain valid and useful results by knowing the exact intended application.

In the scope of the present PhD thesis, the microstructure research and evaluation of materials were focused on W/W_2C composites developed by the Slovenian research group within the European Fusion Programme. The metal-ceramic composites, prepared by Field-Assisted Sintering Technology (FAST) of tungsten and tungsten carbide powder mixture, demonstrate promising thermo-physical behaviour. However, the mechanism behind the formation of the advantageous microstructure was not yet fully understood. To address these issues, several different experimental and analytical methods were applied to unravel the interplay between the processing parameters, microstructure, and the material's performance under He loading.

1.1 Nuclear Fusion

The world's energy requirements are rapidly increasing while, at the same time, the traditional fossil fuel-based energy supplies are becoming more and more scarce. Nuclear fission power plants offer a good alternative, but their operation cycle produces a series of radioactive fission products that cannot be avoided. They should be treated and stored. In contrast, nuclear fusion is a virtually endless energy source without Long-Lived Fission Products (LLFPs). On Earth, the most efficient fusion reaction is achieved by fusing two hydrogen isotopes (HIs), D and T, to produce a heavier element, He, and a free neutron. D-T fusion reaction requires extremely high temperatures (~150 million K); under these conditions, the particles are ionised and susceptible to being controlled by a magnetic field. Currently, the most promising approach to control, shape, and confine the plasma is by the tokamak device, e.g., an experimental reactor ITER (International Thermonuclear Experimental Reactor, also “The Way” in Latin). The next step toward commercial exploitation by a power plant is the demonstration nuclear fusion power station – DEMO, which has already finished its pre-conceptual design phase [1].

Many technological challenges pave the roadmap toward the commercial exploitation of fusion energy, and one of the bottlenecks is the lack of materials that can withstand the reactor's operating conditions. **Few materials now are known that can withstand the expected conditions in the DEMO reactor without significant degradation, and this issue remains one of the great unsolved challenges in our quest for fusion energy.** In the case of DEMO, the components in the fusion reactor's core (Plasma-Facing Components (PFCs), e.g., divertor and first wall) need to withstand high heat-flux and transient heat loadings such as plasma disruptions and edge-localised modes (ELMs) [2]. During the unmitigated ELM or disruption, the surface temperature of the Plasma-Facing Materials (PFMs) will reach above 1500 K [2]. Moreover, PFMs will be exposed to intense neutron bombardment and HIs exposure and continuous helium production through (n, p) and (n, α) nuclear reactions in PFMs [3]. Additionally, to diminish a radioactive waste footprint, the materials used for fusion applications are limited to low activation energy elements, such as Fe, Cr, V, Ti, W, Si, and C [4].

Tungsten is so far the most promising material for PFCs applications [5] due to its high melting point, relatively benign behaviour under neutron irradiation [6], as well as low tritium inventory [7] and low sputtering yield [8]. Unfortunately, W also possesses a high DBTT [9], low ductility and poor fracture toughness [10], low machinability and fabricability [8], low-temperature brittleness [11] and, compared to the operating temperature window, a relatively low recrystallisation temperature. W is also associated with radiation-induced embrittlement, most pronounced for irradiation temperatures below ~0.3 T_{melt}, where T_{melt} is the melting temperature (tungsten ~3600K) [12]. By increasing irradiation exposure time, tungsten will be more and more affected by thermal creep and high-temperature helium embrittlement. Especially brittleness at low temperatures presents the main obstacle for implementing W as a structural material of the fusion reactor [13]. The contribution of helium produced from neutron-induced reaction depends very much on the elements' choice for the PFMs [14]. Hypothetically, if 1 at. % of tritium is retained in tungsten, we can expect 600 appm of helium to be created through tritium decay [15]. After five full-power years of neutron irradiation in a fusion reactor, we can expect to achieve 30 appm of helium in tungsten [14]. At the same time, the emitted α -particles with MeV-range energy will also generate defects in the crystal lattice, mainly by displacement damage [14], [16]. The helium-induced structure alterations will consequently also affect the macroscopic properties of the material, reflecting on altered mechanical properties such as creep and fatigue behaviour and tensile strength [17], [18]. The rapid He accumulation at elevated irradiation temperature along the grain boundaries and dislocations promotes inter-granular fracture known as helium embrittlement [19], leading to pronounced swelling, surface blistering and exfoliation [16], [20]. The main source of helium ions arises directly from the fusion reaction and indirectly by the decay of tritium [15] or by the transmutation of the first wall materials [21]. In the collision of the high-energy He ions with PFMs, the He ions will penetrate to a certain depth because of their low solubility and diffusivity in metals [22]. If the irradiation dose is high enough, He ions will merge to form bubbles [23]. Under favourable conditions, the combination of the gas pressure and shear stress can result in the plastic deformation of the metal, which exhibits on the sample’s surface by forming blisters that can eventually break and cause erosion and plasma contamination [23], [24]. Indirectly produced helium during neutron irradiation will migrate to grain boundaries and form a bubble network [19].

At elevated temperatures, W is relatively poorly oxidation resistant, presenting additional challenges in the consolidation process. Hence, tungsten sintering is usually done in a protective gas atmosphere or vacuum to suppress W-oxides' formation. Additionally, during the consolidation of W and W-based materials, one of the key issues is that even minor impurities of O and C accumulated during metal powder production and handling will reduce the mechanical properties of the final consolidated W and its composites [8]. The presence of impurities in metallic W, for instance, even as small as only trace amounts of oxygen in the range of ≤ 30 ppm, will cause the formation of oxide-rich tungsten secondary phases at the grain boundaries and consequently to enhanced embrittlement and increased DBTT [1], [25].

Considering these shortcomings, to meet the requirements for the W-based material to withstand high heat fluxes combined with ion bombardment in the proposed operation window of the DEMO reactor, further improvements of the tungsten properties are needed before it can be implemented in practical use [1]. Up to now, several W-based materials have been proposed in the scope of the DEMO concept, such as W fibre-reinforced W composite, oxide- and carbide-reinforced tungsten-based materials, and tungsten smart alloys (such as W-Cr-Y) [1], [26]. One of the approaches is implementing transition-metal carbides (e.g. TiC, TaC and W_2C) distributed at the tungsten grain boundaries, which can act as a grain-growth inhibitor and restrict dislocation motion, resulting in improved high-temperature strength and creep resistance [13], [27]–[30]. In the case of the W and W/W_2C composites, we interpreted the composite's physical properties by understanding the microstructure evolution during sintering and by micro- to nano-structure analysis of the proposed PFM on all hierarchical levels.

1.2 Tungsten and Tungsten-Based Crystalline Phases

Most of the properties and findings in the present work and published articles originate from the basic atomic-level interactions. The following section presents several important concepts and factual data on W's interactions with O, C, and He. From the W – C and W – O phase diagrams, the most relevant phases described in this work are W, WC, W_2C and WO_2.

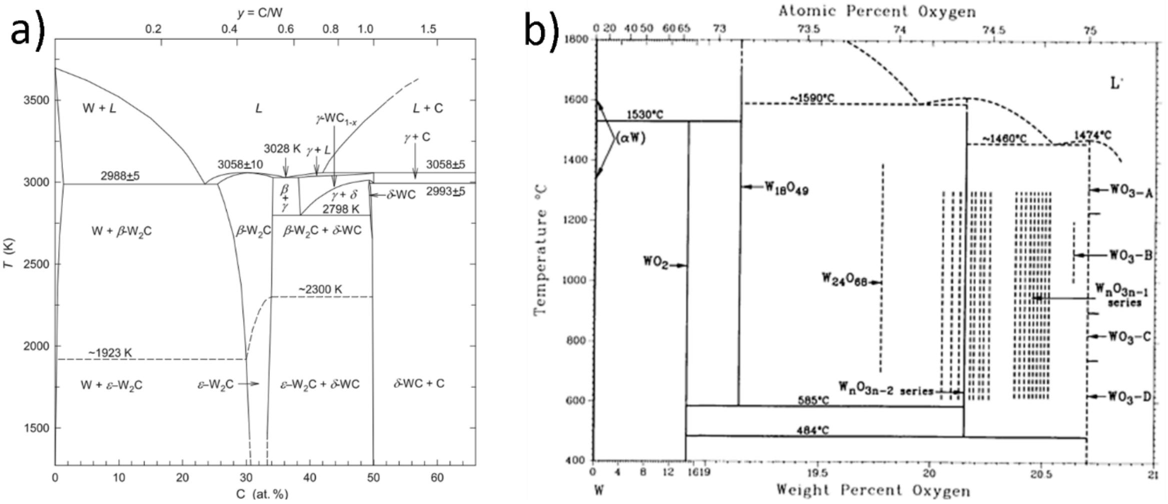

Figure 1: a) Phase diagram of W–C system. The trigonal ε-W_2C phase is thermodynamically stable in the temperature range of 1300–2300 K [31]. b) Phase diagram of W–O system. On its oxygen–poor-side, the WO_2 phases coexists with W at temperatures up to 1800 K [32].

1.2.1 Atomic structure and bonding

The electron shell structure determines the macroscopic physical properties of the solids. The electrons in the outmost orbital have the largest influence on properties, as they determine the interactions with other neighbouring atoms. In the case of noble gases (such as helium), an atom already has a fulfilled outer shell with eight electrons; therefore, its tendency to interact with other atoms is very small. All other elements that do not possess a noble gas configuration tend to accept, donate, or share the outmost valence electrons. Therefore, the atomic interactions are mainly driven by the propensity of an atom to have its outermost valence shell filled. For tungsten, the most stable atom arrangement is the *bcc* crystal structure outturn from its strong metallic bond [8]. Tungsten forms compounds in the valence states from -2, -1, 0, +2, +3, +4, +5, and +6 and tends to form compounds with C and O. The binary tungsten-carbon system has high technical importance as the main constituent of the commercial cemented carbides. On the other hand, the vast tungsten-oxide system is considered extremely complex and is one of the richest fields in structural chemistry, with many sub-stoichiometric intermediate phases [8]. Tungsten carbide phases formed in the W-C system and tungsten oxide phases in the W-O system belong to the nonstoichiometric interstitial compound group, with a combined group covalent-metallic-ionic type of chemical bond. In the nonstoichiometric compound, we can expect that thermal and electrical conductivity decreases with temperature [8], [31], as well as microhardness [33]. Additionally, the bonding behaviours of W–C compounds lead to a high melting point, high hardness, and good electric conductivity [34].

1.2.2 Crystal structure of tungsten and tungsten-based ceramic materials

Most metals and ceramics have ordered crystal structures, i.e., are crystalline. Most properties, including electrical, magnetic, thermal, and particularly mechanical properties, originate in the crystal structure. Below, several most important phases found in the investigated materials are presented, with data on the atom occupancy and crystal structure, which were used to calculate and interpret the experimentally obtained results. The structures are graphically visualised as balls-and-stick models (Figure 2-5, with the corresponding factional coordinated, Table 1-4) for direct comparison and observation of similarity and their differences.

1.2.2.1 Tungsten

Tungsten has a *bcc* structure of type *A2* (W-type), with the lattice parameters a= 0.316 nm and nearest neighbour distance of 0.276 nm, α= 90° at room temperature [8]. A *bcc* unit cell structure consists of a cubic array of atoms, where one full atom is positioned in the cube's centre, and each of the 8 corners shares a 1/8 of an atom. Therefore, the *bcc* unit cell consists of two full atoms (1 central atom and 8 × 1/8 corner atoms) . Compared to the more common face-centred cubic (*fcc*) unit cell arrangements, the atoms in the *bcc* unit cell are less closely packed. The loose atom-packing type makes the *bcc* structure harder and less malleable than *fcc* materials.

Basic crystallographic data for W: cubic crystal system, Hall notation: $\bar{I}423$, Point group: m$\bar{3}$m, Hermann Mauguin: Im$\bar{3}$m, No. 229. Lattice parameters: a = b = c = 0.316469 nm, $\alpha = \beta = \gamma = 90°$, V = 0.031695 nm^3.

Table 1: Fractional coordinates of W.

W		
a	b	c
0	0	0

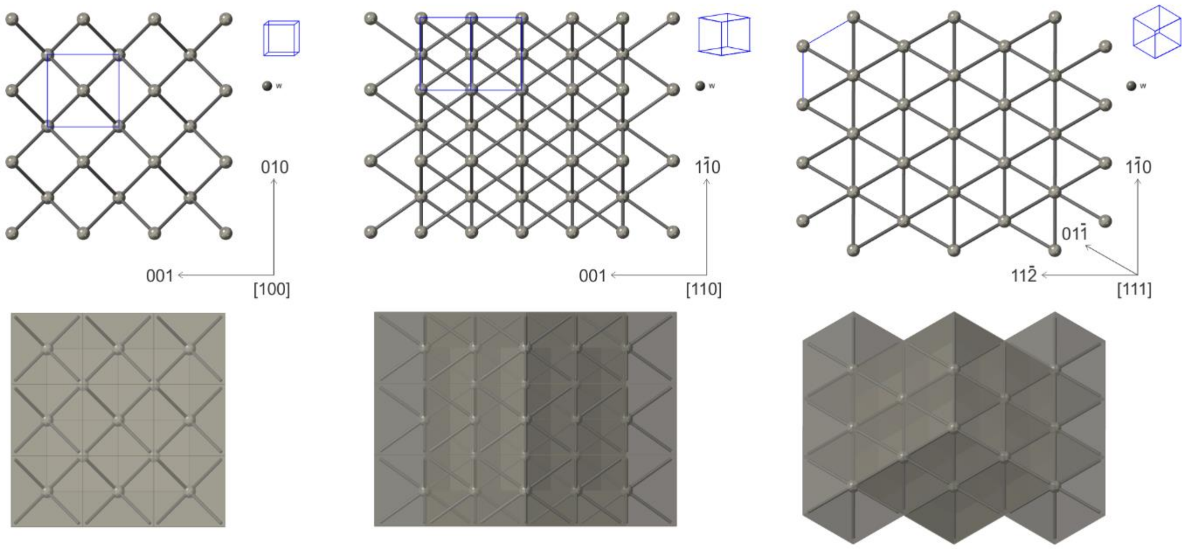

Figure 2: Crystal structure of W in [100], [110] and [111] orientation, with marked unit cell (blue square, in legend slightly tilted off-axis) and orientation of crystal axes. The bottom row presents the octahedral model constructed around the W atoms.

1.2.2.2 Tungsten carbide

Ceramic materials are primarily bonded by ionic bonds between metals and non-metals, particularly carbon (carbides) and oxygen (oxides). The coordination of the atoms in the crystal structure depends on the size and type of the atoms; therefore, different crystal structures in ceramics materials are abundant. For example, tungsten with a *bcc* structure forms carbides with cubic or hexagonal metallic sublattices [31]. Based on this information, we can already conclude on physical properties, as it is well-known that crystal structures with low symmetry tend to be brittle [31], [35].

The W-C system comprises two main phases: W_2C and WC. Each has a number of structural modifications that are only stable in a limited stoichiometry and temperature range [31] – here, only polymorphs identified in the investigated materials will be explained in detail. Mono-carbide tungsten (WC) has two different structural modifications: hexagonal (space group P$\bar{6}$m2) and cubic (space group Fm$\bar{3}$m). In the hexagonal modification of WC (h-WC or δ-WC or α-WC or simply WC), the W and C atoms form a simple hexagonal layer, and both the tungsten and carbon atom sites are trigonal prismatic. The structural types of the tungsten semi-carbide modifications (α, β, γ, ε-W_2C) can be described based on the simple *hcp*-tungsten sublattice, where one of the halves of trigonal-prismatic interstices is occupied with C atoms in various ways. For example, in ε-W_2C, each C-vacancy is surrounded by six C atoms, and accordingly, each C atom is surrounded by six C-vacancies [31], [36]. The structure polymorphs of WC and W_2C show a lower melting point than pure *bcc* tungsten but are still high enough to be considered for applications at temperatures achieved in the fusion reactor operation window.

Basic crystallographic data for WC: hexagonal crystal system, Hall notation: P$\bar{6}$2, Point group $\bar{6}$m2, Hermann Mauguin: P$\bar{6}$m2, No.187. Lattice parameters: a = b = 0.2928 nm, c = 0.2853 nm, α = β = 90°, γ = 120°, V = 0.021186 nm^3.

Table 2: Fractional coordinates of W and C in WC.

<table>
<tr><th colspan="3">W</th></tr>
<tr><td>a</td><td>b</td><td>c</td></tr>
<tr><td>0</td><td>0</td><td>0</td></tr>
<tr><th colspan="3">C</th></tr>
<tr><td>a</td><td>b</td><td>c</td></tr>
<tr><td>0.6667</td><td>0.3333</td><td>0.5</td></tr>
</table>

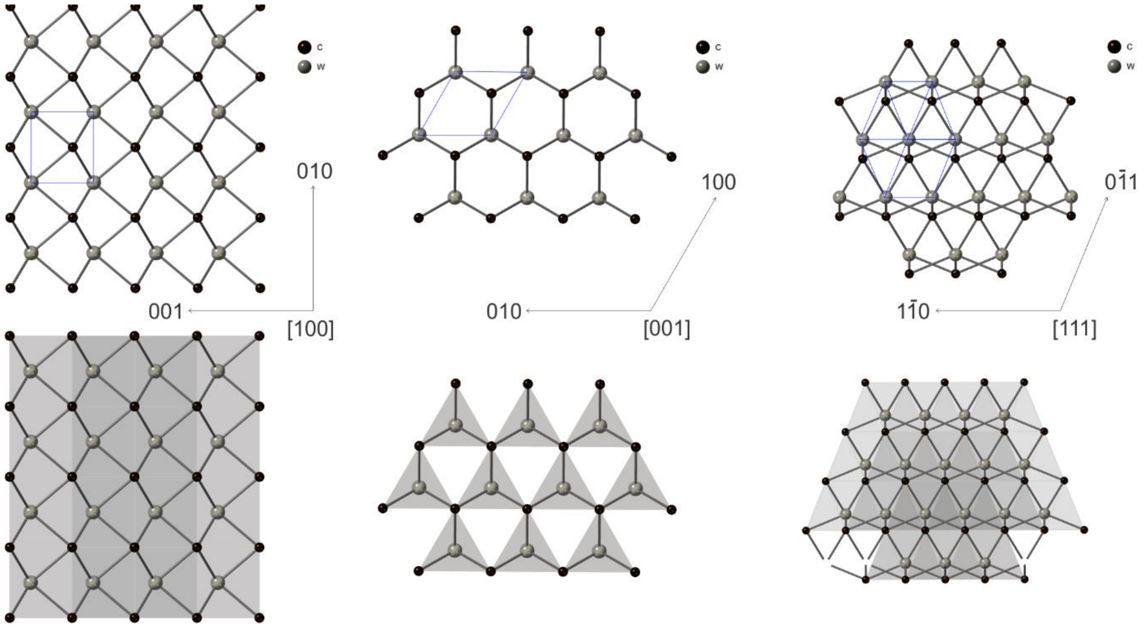

Figure 3: Crystal structure of h-WC in [100], [001] and [111] orientation, with marked unit cell (blue lines). The bottom row shows the tetrahedral model constructed around central W and edge C atom arrangements.

Basic crystallographic data for ε-W_2C: trigonal crystal system, Hall notation: $\bar{P}$32'', Point group: $\bar{3}$m, Hermann Mauguin: P: $\bar{3}$m1, No. 164. Lattice parameters: a = b = 0.3070 nm, c = 0.4678 nm, α = β = 90°, γ = 120°, V = 0.038187 nm^3.

Table 3: Fractional coordinates of W and C in W_2C.

W		
a	b	c
0.3333	0.6667	0.2537
0.6667	0.3333	0.7463
C		
a	b	c
0	0	0

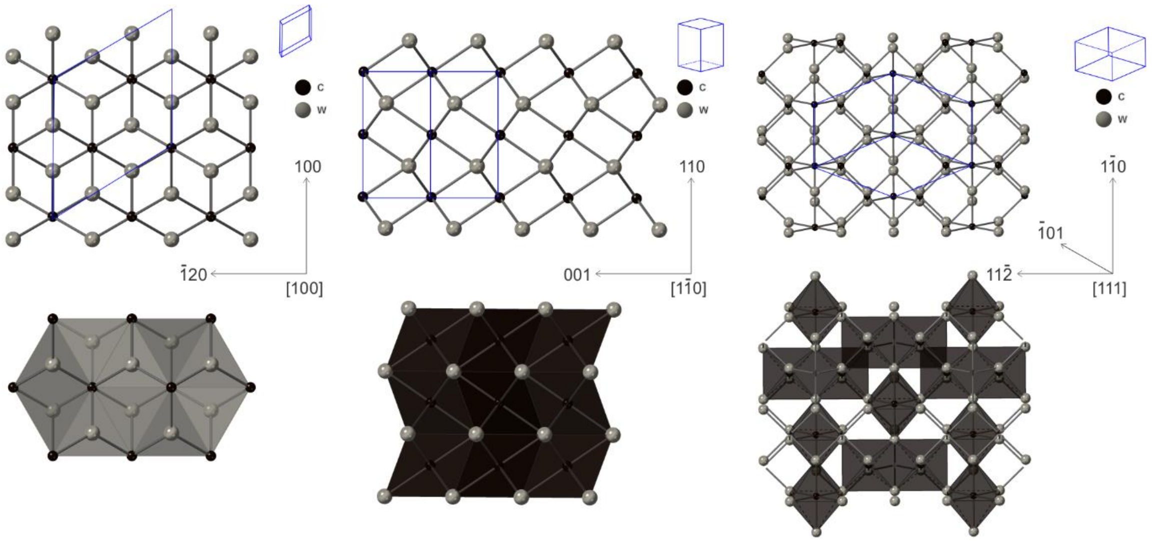

Figure 4: Crystal structure of W_2C in [100], [001] and [111] orientation, with marked unit cell (blue square, slightly tilted in legend). The bottom row shows the octahedral model constructed around the central W atom for [100], and around the central C atom for [1$\bar{1}$0] and [111].

1.2.2.3 Tungsten dioxide

In addition to W and oxygen (O), the W-O system includes the solid equilibrium phases of the W-O system that are: a *bcc* terminal solid solution (α-W), the monoclinic oxides (such as WO_2, $W_{18}O_{49}$, $W_{24}O_{68}$, W_nO_{3n-2}, and W_nO_{3n-1}) and the oxide WO_3, of which at least 11 modification types were reported [32]. Tungsten-rich-oxide phases have a lower melting point in comparison with *bcc* W[8]. In our experiments, only WO_2 was identified.

Basic crystallographic data for WO_2: monoclinic crystal system, Hall notation: P21/c, Hermann Mauguin: P21/c, No. 14. Lattice parameters: a = 0.5563 nm, b = 0.4896 nm, c = 0.5663 nm, $\alpha = \beta = 90°$, $\gamma = 120.47°$, V = 0.132939 nm^3.

Table 4: Fractional coordinates of W and O in WO_2.

W		
a	b	c
0.2278	0.0102	0.0111
O_1		
a	b	c
0.119	0.2186	0.2334
O_2		
0.39	0.0102	0.0111

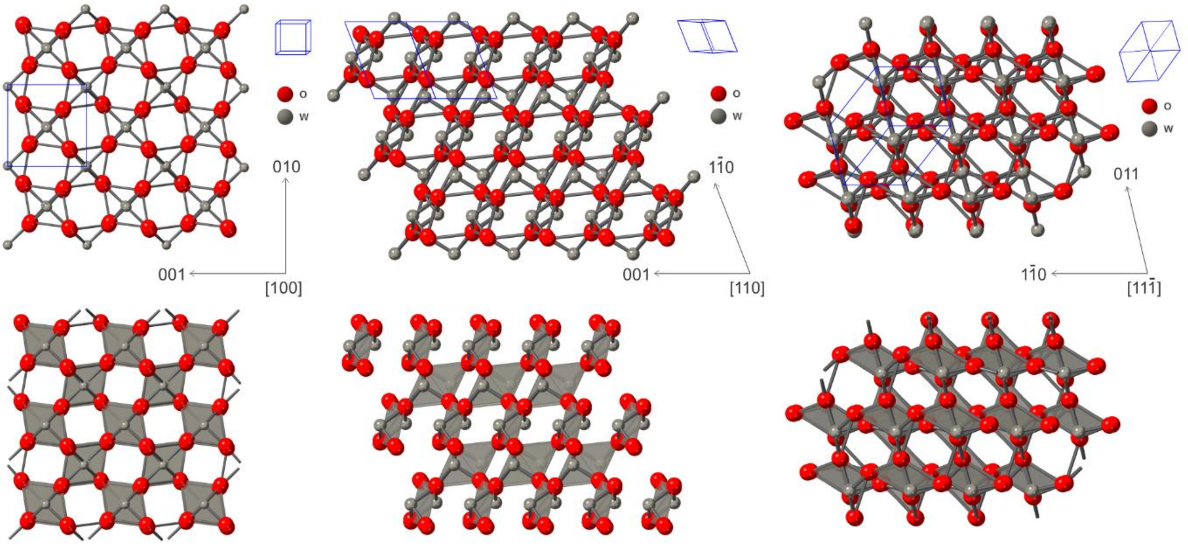

Figure 5: Crystal structure of WO2 in [100], [001] and [111] orientation, with marked unit cell (blue square, slightly off-axis in legend). The bottom row shows the octahedral model constructed around the W central atom, with edge O atoms.

1.3 Crystal Defects

Although for calculations, simulations and visualisation, the crystalline systems are often simplified and considered perfect lattices, the atomic arrangement is heavily subjected to various imperfections and defects in real-world samples. In polycrystalline materials, the grain boundaries present the largest defect and often dictate the overall physical properties. Nevertheless, the imperfections and defects inside the individual grain (crystallite), especially in metals, affect the overall physical properties, often interacting with each other as well as with the grain boundaries, making the whole system an interesting result of synergistic effects.

On the micro- and nano-structure level, lattice distortions can be categorized into four main groups: ***point defects***, namely vacancies, self-interstitial atoms and impurity atoms, ***line defects*** in the form of dislocations, ***plane defects*** such as grain boundaries or phase boundaries and ***volume defects*** (clusters, voids, and bubbles) [35]

Apart from impurities representing the perfect crystal's disorder, there are principally two types of ***point defects***, namely *vacant lattice site* (vacancy), where an atom is missing from one of the lattice sites, and *interstitial site* (interstitial atoms), where the placement of an atom in an unoccupied site in the crystal structure [35]. Point defects can also combine or unite in special configurations. For example, a vacancy can occur when a subsurface atom leaves its lattice site by a diffusional jump to the surface, creating an empty space behind it. Repeating this action, vacancies become distributed homogeneously throughout the crystal [35]. Impurities with the smaller atomic radii as the host atom are placed in the interstitial position in the lattice, i.e., interstitial impurities. Such impurities induce lattice distortion, affecting the mechanical properties and are described by the size similarity of the host atom.

In contrast, impurities in size similar to the host atom are usually placed in the substitutional position in the lattice and are also known as substitutional impurities. Interstitial impurities in tungsten can occupy octahedral and tetrahedral interstitial sites (e.g., He) [37]. On the other hand, a Frenkel defect or Frenkel pair is built when an atom is displaced from its regular lattice site to an interstitial site [35]. In crystalline ionic compounds, either Frenkel defects or pairs of vacancies are generated, and these pairs are referred to as Schottky defects [35].

Dislocations are crystallographic ***line defects*** within a crystal structure and present disruption of the perfect crystal along a line, where a crystallographic plane terminates in a crystal. We distinguish two main types of dislocations: *edge dislocation and screw dislocation* [35]. Edge dislocation is the termination of an atomic plane [35]. Screw dislocation can be visualised as displacing a crystal along a lattice plane and sliding one half across the other by atomic spacing [35]. Moreover, a dislocation can also change its character from screw to edge dislocation. A dislocation can also occur in a crystal in a closed-loop configuration. Such a *dislocation loop* can be visualised by cutting the interior of the crystal along a specific plane. On the other hand, the presence of impurities can also affect the dislocation arrangement. The presence of carbon atoms in the vicinity of dislocation in tungsten lattice can induce reconstruction, affecting the mechanical properties (i.e. carbon embrittlement) [25], [38].

Among the ***plane defects***, the *grain boundary* (GB) is determined as two individual single crystals of different orientations joining into an interface. Most materials are polycrystalline, composed of multiple grains and grain boundary types. The relative orientation of individual grain is defined by the rotation angle α around a specific axis c [39]. The misorientation of two crystals with three degrees of freedom can be represented by the minimum rotation angle (misorientation angle (β)) between two grains corresponding to the standard stereographic triangle. In addition, two degrees of freedom with respect to the spatial location of the grain boundary plane must be considered for an unambiguous description of the grain boundary plane. Combined, a total of 5 parameters are required for an unambiguous description of the grain boundary; hence several classifications are proposed to simplify the description. For example, the relationship between two grains and rotation axis c defines a tilt grain boundary when rotating around the same crystallographic axis. When two grains are rotated around the axis normal to the GB, the twist grain boundaries type can be obtained [35]. At the same time, the GBs containing both tilt and twist components are called “mixed”. The misorientation angle β defines a small angle GB (SAGB) for $\beta \leq 15°$ or a high angle GB (HAGB) for $\beta \geq 15°$ [40]. Moreover, a realistic grain boundary contains crystal defects that introduce disruption of periodicity within the intergranular structure, and these defects are responsible for most of the unusual grain boundary properties. The density of point defects, such as vacancies and interstitial or substitutional atoms, is generally higher in the grain boundaries than in bulk.

According to the nature of the forces causing local enrichment in solutes, i.e., grain boundary segregation [41], we can distinguish two basic types: equilibrium (thermal or thermo-mechanical treatment) and non-equilibrium grain boundary segregation (quenching and irradiation) [42], with the latter consisting of the interaction of solute atoms with the excess of vacancies in the system. A solute concentration is thus built up around the boundary because of dragging the vacancy-solute pairs. Segregation of light elements, such as oxygen and helium at tungsten grain boundaries, will cause a significant decrease in the ductility of the materials, known as embrittlement [16], [25]. It is worth mentioning that monocrystalline tungsten-based materials have both high-temperature strength and plasticity, which makes them most suitable for use under high temperatures and high mechanical stresses compared to polycrystalline tungsten materials [43].

Compared to the structure of grain boundaries, the structure of *phase boundaries* (PB) is even more complex as the adjacent crystallites can, besides different crystallographic orientations, also have a different crystal structure. A *coherent phase boundary* is defined as undisturbed passing from lattice planes [35]. In some cases, not all lattice planes are continuously transferred across the interface; such type is referred to as *partially coherent.* If two grains have different chemical and crystal structures, the coherency of the interface is lost and is defined as an *incoherent phase boundary* [35].

Helium is a ubiquitous impurity in nuclear materials, and in terms of lattice imperfection classification, it falls under point defects (impurity atoms). As it can be highly mobile in the W lattice and requires a short explanation of its origin, it is presented independently here at the end of the chapter. In the fusion reactor materials, (n, α) reactions, ion implantation, or radioactive decay of tritium, which has permeated into the metal, can lead to the production of alpha particles. These particles can accumulate to form helium gas [44]. Helium has a closed-shell electronic structure and exhibits a very weak tendency for chemical bonding with the host material but tends to accumulate on pre-existing defects [16], [45]. Generally, due to its electronic nature, helium prefers first to occupy the defects with large space, in the following order: grain boundaries > dislocation > point defect [46]. Accumulations of He in the crystal lattice lead to significant changes in the mechanical properties of the structural materials. The effects of helium accumulations on metals, known as helium embrittlement, present a potential limitation to the useful lifetime of fusion reactor materials [47]. A few strategies are suggested to mitigate helium embrittlement [16]. One of them is suggested to be related to a fragmented microstructure of the ferritic/martensitic steels containing fine carbide precipitates in the ferritic matrix positioned at the low-angle boundaries. It is proposed that such microstructure, i.e., microstructure refinement, can provide a high density of trapping sites for He atoms at the phase boundaries and consequently decrease the helium concentration on high-angle grain boundaries [48].

1.4 Processing Methods of Tungsten and Tungsten-Based Materials

The microstructure of the consolidated materials strongly depends on the processing methods. One of the most basic parameters is the presence of impurities. The initial tungsten powder used in the experiments relevant to my thesis is reported to be obtained from three different W compounds: $(NH4)_2WO_4$, WO_3, and $W_{18}O_{49}$ by hydrogen reduction in the temperature range of 700 to 1100 K [8]. The purity of the so-obtained tungsten powder is >99.97 %.

On an industrial scale, tungsten powder is compressed into bars and pre-sintered at approx. 1200 K. Larger ingots are heated indirectly by contact molybdenum strips at temperatures of about 2700 K and need precisely controlled temperature ramping to prevent oxidation at lower temperatures, as well as mitigating thermal stress at higher temperatures. The sintering of about

10 h is typically required for densification. Smaller samples are then sintered in a hydrogen atmosphere by direct electric-current heating at about 3000 K, with a 30-60 min holding time.

On a micron laboratory scale, thin or thick tungsten films on substrates can be obtained by chemical vapour deposition (CVP), physical vapour deposition (PVD), or plasma spraying and the subsequent working (recrystallisation, annealing, etc.) [8], [49]. In the current ITER divertor design, almost the whole divertor inner surface is covered by tungsten, together weighing more than 100 tons. The inner armour is also planned to be replaced 5 to 8 times during operation. We can extrapolate that metallurgic processing of powder consolidation is the most available processing method for tungsten densification. Nevertheless, metallurgic processing requires high temperature and involves mechanical treatment such as rolling and forging to achieve the desiderate bulk density. In the early 1990s, Field Assisted Sintering Technology (FAST) became commercially available, and today is available as a large-scale consolidation technique, with several FAST devices on the market capable of different powder consolidation systems in demanded scope [50]. FAST is an advanced sintering technique utilising uniaxial force and direct electrical current that enables high-speed consolidation of the powder. With these unique features, FAST has been reported to improve densification and minimise grain growth in various materials, including metals and composites [30], [51]. In the scope of the present thesis, the base materials, compounds and FAST-consolidated W and W/W_2C samples were developed within the European Fusion Programme and were provided by the Slovenian research group from the Jožef Stefan Institute, Department for Nanostructured Materials (K7 – JSI) [27], [30].

1.4.1 Sintering

In the scope of the materials projected for use in the fusion reactor, very dense materials are desirable to achieve the properties such as high thermal conductivity and adequate mechanical properties. Consolidation of tungsten has several specific limitations, such as a tendency for rapid oxidation at high temperatures, which restricts possible production techniques. Nevertheless, for a full understanding of the microstructure, the background information on the sintering processes is provided in the following paragraphs.

1.4.1.1 Densification process

Sintering is a fabrication technique for the production of bulk materials from powders. In the most basic case, we expose compacted powder particles to elevated temperatures to promote bonding among particles through atomic diffusion. The sintering temperature is typically in the **range of 50 % to 75 % of the material's melting point** [52]**. Optimisation of the sintering** conditions can tailor the final products with variable degrees of porosity. Furthermore, near-net-shaped products can be obtained right after sintering by using shaped dies. In solid-state sintering, densification is achieved by rearranging atoms in a solid state, and these phenomena can be described using the two-sphere sintering model. In this model, two spheres are placed in close contact, and the bonding develops at the particle interface in the neck area. During the sintering process, each particle (sphere) centre moves towards the other. With sufficient time, two particles will fully merge into a single large sphere with a lower surface area than the two starting particles and the total density approaching a theoretical value. The driving force of sintering is to minimise the surface free energy per volume of the material system by atomic diffusion. Particulate materials (powders) have a larger surface area than bulk materials of the same volume, consequently also larger surface free energy per volume than bulk materials. With a relatively high driving force for sintering, smaller starting pores, and shorter diffusion distance, finer particle systems tend to undergo sintering at lower temperatures.

1.4.1.2 Sintering stages

Idealised geometrical models can be used to describe the *early*, *intermediate*, and *final stages* of sintering [53]. The *initial stage* of sintering is characterised by a rapid neck growth between two particles due to the large differences in surface curvature between the particle surface and the neck area. The particle contacts are replaced by the neck- and grain-boundary formation. As the neck grows, the curvature of the neck or pore increases, further reducing neck growth and particle shrinkage. The initial stage ends when the multiple necks on each particle start to interfere with each other at a value of around 40-50 % of the particle radius. We can observe only a minimal increase in density in the initial sintering stage. The *intermediate stage* is characterised by pore rounding, grain growth, and densification. The effect of densification is explained by shrinking the cross-section of the tube-like pores, where a volume change occurs. The grain boundary rearrangement is required to compensate for volume change during grain growth, which is achieved by grain twisting and rotation. During the intermediate stage, the cross-section of the pores keeps shrinking until the pores become unstable and transform into isolated pores. The intermediate stage is responsible for the major part of the sintering process. The relative density obtained at the end of this stage is around 90 % of the theoretical value. In the *final sintering stage*, the pores become isolated as spheres, and the relative density has reached approx. 95 %. The pores continuously shrink and may disappear if they are still attached to grain boundaries. In the final stage, grain growth starts to become a significant factor. If the grain boundaries are separated from the pores, the pores will remain trapped inside the grains.

1.4.1.3 Field Assisted Sintering Technology (FAST)

Besides the field-assisted sintering technique (FAST), several other names are used in the literature, such as pulsed electric current sintering (PECS) or spark plasma sintering (SPS) [50]. In the past decade, FAST has become one of the most popular fast-sintering methods for processing metal-based ceramic composites and highly refractory metals [30][54]. Unlike other conventional sintering processes, FAST can achieve extremely high heating rates by passing a current through the compacted powder and mould assembly, resulting in a fast Joule heating effect, where the heating effect strongly depends on the electrical resistance. A combination of low-voltage, high-amperage, pulsed direct current (DC) and uniaxial pressure is usually employed [50]. The initial powder is wrapped into the graphite foil and placed in a graphite mould (although several different tooling arrangements were suggested in the literature, a graphite setting was used to produce the samples investigated in this work). During the sintering, the pressure and electric current are applied to facilitate the densification of the powder into the bulk. A few different mechanisms were proposed for sintering enhancement attributed to the effect of heating rate, pressure, current, and localised heating [54]. Rapid heating minimises particle coarsening before the sintering temperature is reached. At the same time, the simultaneously applied pressure mechanically contributes to the sintering process by improving particle rearrangement, breaking agglomerates, collapsing pores, and accelerating the driving force for sintering. In a particle system, electrical resistance seems to be highest at the particle contacts leading to the localised heating at the particle contacts. This heat has been speculated to be high enough to melt or evaporate impurities at the surface, promoting direct contact between particles, and leading to mass transport [55].

1.4.2 Reactive processes for oxygen removal during sintering

For polycrystalline tungsten, even trace amounts of oxygen impurities associated with the processed powders can induce the formation of tungsten-oxide secondary phases [56]. To reduce grain-boundary oxide formation, a direct carburisation process using carbon or carbon-containing compounds can be applied to prevent undesirable secondary phase formation at elevated temperatures [8]. Recently, it was also observed that transition metal carbide MeC (Me-metals) exhibited the ability to reduce oxides during sintering [57]. The carbon balance in the system is difficult to control and often leads to incomplete reduction, or the final sample contains carbide residues that can affect the mechanical properties [8], [25].

For the thermal decomposition analysis of the W-based mixtures, I worked together with colleagues from Jožef Stefan Institute, Advanced Materials Department (K9 – JSI).

1.5 Microstructure

The properties of materials are affected by the specific arrangement of different phases (grains, precipitates, pores, etc.) known under the term microstructure. The phases are distinguished from each other by their degree of crystallinity (known as crystalline, semi-crystalline or amorphous structures) when visualised by an optical or electron microscope [58]. Specimen preparation is crucial for both types of microscopies and must be truly representative of the sample; and involves metallographic preparation processes to expose the features of interest [59]. With optical methods, we obtain insight into microstructure on a micro-scale. Still, for the advanced microstructure characterisation in combination with analytics, electron-based microscopic techniques such as scanning electron microscopy (SEM) and transmission electron microscopy (TEM) with accompanying spectroscopic methods are needed to provide qualitative and quantitative information on morphology, structure, and chemical composition on micro, nano and atom scale. A detailed description of the microscopy techniques applied in the scope of the present thesis can be found in the subsequent Chapter 3: Materials and Method.

Chapter 2

Aims and Hypothesis

Doctoral dissertation entitled "Microstructural analysis and evaluation of W and W/W_2C composites for fusion application" focuses on understanding the evolution of the microstructure during sintering, the role of secondary phases formed during the sintering, and on analysis and evaluation of proposed composite materials as PFMs. The aim of this dissertation is to explore the physico-chemical properties of W and W/W_2C, prepared via powder technologies by the Slovenian research group [27], [30] within the European Fusion Programme.

My dissertation aims to contribute to developing an improved W-based material for the fusion applications proposed by the Slovenian research group within the European Fusion Programme. The key to establish a fundamental understanding of the correlation between synthesis, microstructure, and properties of processed materials is to characterise the materials on all structural and chemical hierarchical levels and, in the end, to accurately assess the effect of the helium implantation with subsequent annealing as a proxy for running plasma. Within the scope of research work, the following aims are addressed:

1. Development of sample preparation protocols for microstructural analysis of the samples,
2. Implementation of research methods capable of providing reliable results on chemical composition and crystal structure of the W-based materials with high accuracy and statistical significance,
3. Determination of the role of W carbides in the process of the consolidation treatments,
4. Mitigation of the oxide formation by a direct reduction process at elevated temperature, using carbon or carbon-containing compounds,
5. Evaluation of the damage and modifications of the microstructure induced by energetic He-ions as a proxy for running plasma,
6. Identification and characterisation of the He behaviour in the crystal lattice of the W and W-based metal-ceramic composites,
7. Identification of possible accommodation sites for He ions within the crystal structure of the W-W_2C host material.

In the first step of the research, I will identify a proper methodology (aim 1, aim 2). These procedures will be implemented and tested on W/W-based composites (aim 3, aim 4). The results will provide feed-back information on the initial sample synthesis stage for further material optimisation. In the next stage, the performance of the materials and the influence of the light-elements implantation will be assessed and evaluated (aim 5, aim 6), with the theoretical prediction of the He behaviour in W/W_2C materials (aim 7).

The investigation, analyses, and modifications of the W/W_2C composites will be based on the following hypotheses:

I. Sintering by powder processing of the W and W-based composites results in the formation of additional minor oxide phases due to the small amounts of present oxygen in the commercially available starting powder. Due to the lower thermal stability of oxides (below the suggested nominal operation temperature), their presence should be mitigated as much as possible. The identification and analysis of the oxides will provide feed-back information for appropriate tailoring of the processing steps in order to eliminate undesired oxides.

II. During co-sintering of W and WC, the latter acts as a reducing agent that will prevent the formation of oxide phases. With the thermo-dynamical study of the sintering process, the proper amount of carbon introduced into the starting materials can be determined to avoid oxide formation.

III. During the high-temperature sintering of W and WC powders, WC decomposes and forms W_2C, a thermally stable phase. The formation of the W_2C dispersoids (precipitates) at specific positions within the microstructure will enhance the physical properties of these materials, as per the theory of Particle-Reinforcement where particulates prevent the movement of the dislocation through the Orowan mechanism.

IV. He implantation will induce physical damage in the W-matrix and W_2C particulates. Possible bubble formation can therefore be expected at elevated temperatures.

Implementation of research tools and techniques for microstructural characterisation of W and W-based composites and results obtained herein are expected to advance the fundamental understanding of materials projected for fusion applications. The research is expected to have an impact on the following research topics and fields:

- *Implementation of methodology and techniques for the research of metal-ceramic composites.* Due to the intrinsic properties of metal-ceramic composites, the microstructure research using standard evaluation methods is highly demanding; therefore, new approaches in sample preparation, surface treatment, and analyses have to be developed. The methods proposed for the research of W/W_2C composites are transferrable to other systems, e.g., Cr/Cr-carbides.
- *Refractory and other materials for high-temperature applications.* The mitigation and possible removal of the thermally-nonstable sintering side products like oxides can reveal new practical applications of such materials for operation at elevated temperatures, over the decomposition temperature of the oxide phases limiting their use.
- *Development of the W-carbides for technological application.* Currently, bonded W-carbides are widely used for tooling, and the research on the *in-situ* formation of carbides in the metal matrix opens new opportunities for material design and applications. The research of inter-granular dependencies, exsolutions, and precipitation on grain boundaries is an important aspect of the R&D of carbides.
- *Accommodation of the light elements in tungsten metal and composites.* The study of the crystal structure and possible incorporation positions, migration, and coalescence of light elements in solids have important practical aspects for vacuum applications, welding, and metal corrosion.

Chapter 3

Materials and Methods

3.1 Materials

3.1.1 Starting materials and He-implanted materials

The Slovenian research group within the European Fusion Programme provided the base materials and compounds, as stated in Chapters 3.2.2. (sample preparation). The synthesis of the W and W-based materials, optimisation, and chemical modification was prepared by FAST powder consolidation at elevated temperature under moderate vacuum. The tungsten-based composite samples were implanted with 1 MeV $^4He^+$ ions at room temperature [60] using a tandem-type ion accelerator [61]. For characterisation and evaluation of the physico-chemical properties of the initial powders, powder mixtures and W-based composites, several advanced characterisation techniques were used, summarised in the following subchapters.

3.2 Methods

3.2.1 X-ray diffraction

X-ray diffraction is a non-destructive analysis technique. In material science, it is commonly used for the determination of crystal structure, identification of crystalline phases and their orientation, and the determination of structural properties such as phase composition and lattice parameters. For the purpose of this thesis, the X-ray diffraction data of the–samples were collected on D4 Endeavor (Bruker AXS GmbH) diffractometer using monochromated X-rays produced by a Cu-target (λ= 0.15406 nm). The scan range in Bragg angles was from 20° to 80° 2θ, and the final XRD data were analysed with HighScore Plus XRD analysis software. The detection limit of laboratory XRD instruments is approximately 2 wt. % [62].

3.2.2 Sample surface preparation for microstructure characterization

The samples for SEM analysis were prepared following a conventional metallographic procedure by rough formatting and cutting, followed by grinding and polishing. The grinding and polishing were performed on the automatic metallographic specimen preparation device – Struers LaboPol. After each grade change, the samples were cleaned in an ultrasonic bath to ensure clean surfaces before further polishing with a higher-grade polishing paper. For the EBSD analyses, the samples were initially polished with 1 µm grade diamond paste, followed by a final 5 vol. % H_2O_2 solution of colloidal silica. A carbon tape was used for powder mounting on the sample holder, and a silver paste was used for bulk sample mounting.

The samples for the TEM analyses were prepared by a combination of mechanical and Ar-ion milling processes (Disc grinder Mod. 623 / Mod. 656, Gatan, and PIPS 691, Gatan). Typical settings for Ar-ion milling of tungsten and tungsten-based materials were: gun impact angles at 8° with a double-sided (top-bottom) milling geometry. The initial ionization voltage was set at 5 kV for rough milling until sample perforation, followed by final polishing at 2 kV for 5 minutes. The milling process was monitored via the optical lens system coupled with a CCD camera. The process resulted in the final TEM sample with large electron transparent regions around the perforation area. For the site-specific TEM samples, the thin electron-transparent foils of tungsten-based materials were realised by a focused ion beam (FIB) lift-out technique [63] on a dual-beam SEM-FIB device (Helios Nanolab 600, Thermo Fisher Scientific). The initial lift-out was done by using 30 keV Ga^+ ions, while during milling and final thinning, the accelerating voltage was decreased to 5 keV to mitigate re-deposition and surface damage of the sample.

3.2.3 Optical microscope analysis

An optical microscope (OM, Zeiss Imager.Z1m, Zeiss GmbH) in reflective mode was used for initial surface features characterisation of samples.

3.2.4 Electron microscopy and electron-matter interactions

The electron microscopes are based on several concepts, with a common intent to provide a magnified image of an analysed object; the final magnification range can vary from micrometre to an atomic scale. The fundamental principle which applies to all versions of electron microscopes is electron-matter-interaction [64][65]. When the primary electron beam hits the sample, several different interactions can occur. These interactions can further facilitate different signals, which can be recorded, processed, and analysed for the purpose of, *e.g.,* morphology or chemical and phase composition of the investigated material. For signal recording, various detectors are introduced into the electron microscope in designated positions.

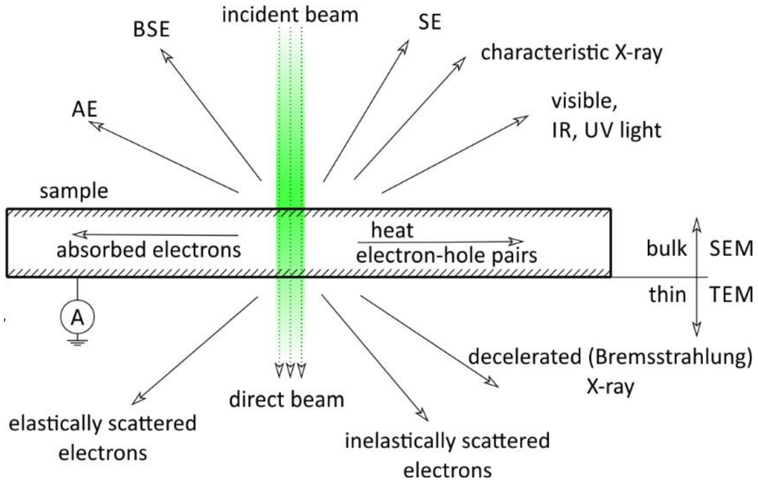

Figure 6: Schematic representation of possible interactions between the primary electron beam and the sample; adopted from [66].

Common inelastic and elastic scattering interactions between electrons and the sample and resulting signals are summarized in Figure 6. The elastically scattered electrons (known as backscattered electrons, BSE) are deflected on the periodic arrangement of atoms in the crystal lattice [65]. The characteristic of the elastically scattered electrons is that they only change their trajectory while their energy is preserved. On the contrary, the inelastically scattered electrons will preserve their trajectory, but some of their energy will be lost during the electron-sample interaction. The energy from this imbalance will emerge from the surface of the observed specimen in the form of electrons as secondary and Auger electrons, or as photons (bremsstrahlung and characteristic X-rays).

The inelastically scattered electrons will generate secondary electrons (SE), which are produced when an electron from the incident beam ejects an electron from one of the outermost shells of an atom of the specimen. During this course, the primary electron transfers a non-specific amount of its energy to the secondary electron. As the amount of energy is arbitrary, no characterisation can be deduced by spectroscopic methods. On the contrary, the energy of the Auger electrons and X-rays can be directly associated with the interacting atom; the energy of the released signal is element-specific and can be used for elemental spectroscopy analysis. Both Auger and bremsstrahlung effects occur when an atom with an electron vacancy in the innermost shell readjusts itself by ejecting electrons. In general, light elements will typically produce Auger electrons, while heavy elements tend to generate X-rays.

3.2.4.1 Scanning electron microscopy

In SEM, an electron source emits electrons which are accelerated and focused into a convergent beam through electromagnetic condensers and objective lenses. This probe is scanned over the sample by scan coils, and the resulting signals are detected point-by-point with different detectors. Figure 7a shows a schematic representation of the typical SEM set-up. The most common signals (imaging modes) recorded by conventional SEM are backscattered electrons (BSE) with an energy ranging from 50 eV up to the energy of the primary beam, and secondary electrons (SE) with energies below 50 eV. BSE originates in numerous elastic scattering events, and its intensity is directly related to the atomic number [65]. By contrast, SE have a smaller escape depth and are more sensitive to morphological features because of their lower energy, as summarized in Figure 7b.

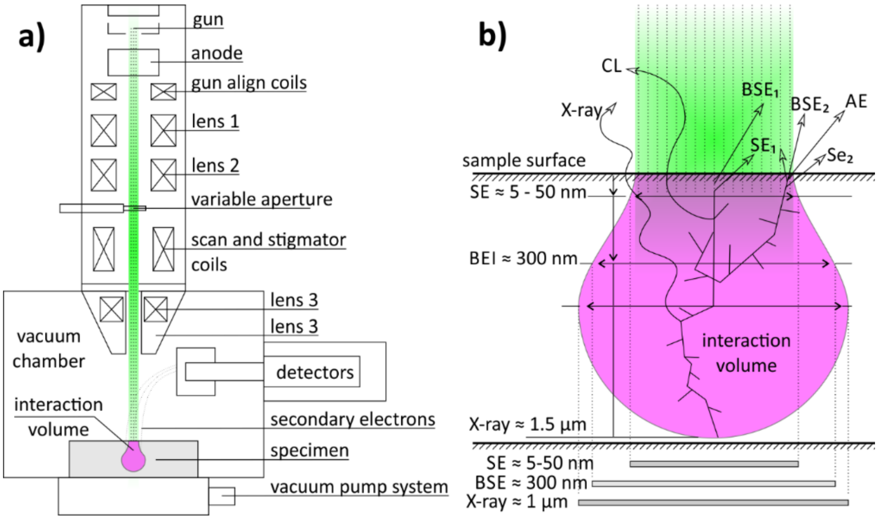

Figure 7: a) Schematic cross-section representation of a basic SEM and b) interaction volume and electron-decay products in SEM; adopted from [66].

Bulk samples are usually studied in a scanning electron microscope (SEM); therefore, the signals we can detect are only produced from the surface. Consequently, the SEM detectors are mounted above the sample. Emitted electrons from the surface interaction between the primary beam and the specimen can be distinguished regarding their different origins and energies.

The microstructural characterisation and compositional analyses in this thesis were performed on FEG-SEM (JSM-7600F, JEOL, and Zeiss Auriga Crossbeam, Carl Zeiss Microscopy) and dual-beam FIB-SEM (Helios Nanolab 650i, FEI). In SEM, the local chemical composition was assessed by Energy-dispersive X-ray spectroscopy – EDS (Octane Elect, EDAX AMETEK, and X-MaX, Oxford Instruments). Quantitative microstructural crystallographic analysis in the SEM was performed by Electron backscatter diffraction – EBSD (Hikari Super, EDAX AMETEK and Nordlys II, Oxford Instruments) and interpreted by the OIM Matrix™ and Channel 5™ (HKL Technology).

3.2.4.1.1 Energy-Dispersive X-ray Spectroscopy (EDS)

The ability of SEM to run the electron beam in stationary or in scanning mode enables us to perform microanalysis using a combination of precise control of the electron beam, adjoined with dedicated detectors. In my thesis, the samples' chemical composition was studied by energy-dispersive X-ray spectroscopy (EDS) [65]. As discussed in chapter 3.2.4, many electron-matter interactions occur when the primary electron beam interacts with the sample. Some of these interactions lead to the excitation of X-rays in the form of Bremsstrahlung and characteristic X-rays. Bremsstrahlung is electromagnetic radiation arising due to a deceleration of the primary electrons at the Coulomb field of the atoms in the sample and forming a continuous background signal in the energy spectrum. The formation of characteristic X-rays, used for assessing the chemical composition by EDS, can be explained as follows: when high-energy electrons hit an atom, they can remove the electrons' inner shell from their positions – either by excitation into a higher energy level or even by knocking it out completely. However, unoccupied states in inner shells are energetically unfavourable and will therefore be filled by an outer shell electron. As this electron has higher energy than required, the excess energy can be released as an X-ray. Because the energy difference between different shells of an atom is specific for the element, the released X-rays are called characteristic X-rays and allow the chemical identification of elements. Dependent on the involved electron states, the X-rays are denoted accordingly. For example, for a transition of an electron from the L to the K shell, the received X-ray line is called K_α, for a relaxation from the M to the K shell K_β, etc. As more than one relaxation process is possible at once, especially for the L lines, so-called families of lines arise. For example, for the L lines, there are five distinct lines.

For the materials considered in the present thesis, it is important to note that some of the energy lines of W overlap with the characteristic energy line of C (W N-lines (N4 255.9 eV and N5 243.5 eV) with C K-line (298.2 eV)), making the EDS method, and especially spatial chemical element distribution analysis (so-called "EDS mapping") rather challenging.

3.2.4.1.2 Electron Backscatter Diffraction (EBSD)

The ability of SEM to record point-by-point a characteristic electron backscatter diffraction pattern, combined with computer-assisted interpretation of the so-recorded signal, enables the interpretation and analysis of the crystallographic features of the investigated sample.

The characteristic EBSD patterns originate in primary-beam electron scattering on the crystal planes. The typical backscatter Kikuchi pattern feature is the regular ordering of bright parallel and traverse lines, stripes and bands [40]. From the intersections of Kikuchi bands, we can conclude on the zone axes in terms of a gnomonic projection of the crystal lattice [40]. By software processing of the experimental data and by comparing the recorded characteristic electron backscattered patterns with a database of crystallographic structure information for phases of interest, we can use EBSD data to identify and analyse the microstructure features such as grain size, boundaries, orientation, and their interdependencies, texturing, defects, and similar. In the case of our materials, we successfully extended the method for the identification of W and W_2C phases based on their crystal structure, which solved the shortcomings of the EDS method. The resolution of the EBSD method is mainly limited by the ability of the SEM to form a finely focused electron probe. For the field-emission SEMs, as used in this thesis, the spatial resolution in the XY plane can be below 100 nm [40].

3.2.4.2 Transmission electron microscopy

While SEM samples demand a carefully prepared sample surface to avoid artefacts, the samples for TEM need even further processing to achieve a final thickness of 100 nm or less; only in this case the primary electrons can at the same time interact and transmit the sample.

The main elements of the conventional TEM are displayed in Figure 8: the primary electron beam, originating from the electron source, passes through the sample, and most of the emerging signals are detected and recorded below the sample [64]. The standard TEM operation modes can be categorised as *conventional TEM* (C-TEM) and *high-resolution* or *phase-contrast TEM* (HR-TEM) modes [64]. In conventional TEM mode, a parallel electron beam illuminates the electron-transparent specimen. Here, only non-deflected elastically scattered electrons are employed for observation of the electron-sample interactions. The electron-sample interaction depends on the crystal structure and chemical composition of the sample: darker regions are usually composed of heavy elements and well-crystallized material, while brighter regions are usually amorphous and composed of lighter elements. The contrast in the final micrograph is a complex combination of thickness, mass, and diffraction contrast, with the latter prevailing. In C-TEM mode, electrons diffracted at a wide angle are cut off by an objective aperture, and the transmitted electrons will form an image based on an amplitude contrast [64]. Aperture is not used in the HR-TEM mode; therefore, all deflected electrons contribute to the final image, which is composed of both amplitude and phase contrast. When samples are thin enough to be considered weak-phase objects, we can deduce that the electron wave's amplitude stays constant and only its phase changes. Consequently, it is not possible to directly correlate the HR-TEM micrographs with the actual positions of the atoms in the sample only from the recorded contrast variations [64]. Such correlations are possible only by employing a computer simulation of the electron and crystal structure interactions, e. g., by using commercially available software, and comparing and correlating the simulated and experimental micrographs [64].

In the scope of the thesis, the thin samples for TEM analyses were prepared either by the FIB site-specific lift-out technique or by a combination of mechanical thinning and ion etching. C-TEM mode was used to screen large regions to analyse, for example, the phase composition and the distribution of the He bubbles. The HR-TEM mode was used to analyse the local crystal structure of the secondary phases found in the bulk sample and was extended by electron diffraction analyses. Using a selected area electron diffraction (SAED) aperture, we cam limit the area of interest from where electron diffraction patterns are recorded. As SAED patterns were pre-calibrated by MAG*I*CAL traceable calibration reference standard, the crystal structure of the bulk and subordinate compounds and phases (i.e. carbides and oxides) were directly calculated from the selected-area electron-diffraction patterns.

Most contemporary TEM devices can operate either in TEM or scanning STEM mode. STEM operation mode is similar to a operation principle of the scanning electron microscope, where a fine sub-nm spot of a focused electron beam is scanned over an investigated region of a sample [64]. Due to the systematic scanning of the electron spot over the sample, it is possible to correlate the emerging signals with the spatial position of the electron spot, which is the basic presumption for the analytical scanning TEM.

For STEM visualisation, two main imaging detectors system are used: bright field (BF) and annular dark field (ADF) detectors) [64]. The difference in detecting the semi-angle of diffracting electrons defines the nature of electrons contributing to the contrast in the micrograph. The BF detector record only the directly transmitted electrons and is highly sensitive for the structural defects. The intensity in the micrographs collected by the dark field detectors is related to the orientation of the crystals in the sample (annular dark field (ADF)-STEM) or to the average atomic number of the elements ($I \sim Z^2$ in the high-angle annular dark field (HAADF)-STEM micrographs). In this work, the HAADF detector was used to distinguish between heavy bulk metal phases and lighter metal-oxide-based phases. The BF-STEM mode was used to visualise the dislocations and other defects present in the crystal structure.

In the scope of this work, TEM analyses of the samples were performed on a conventional 200 kV TEM (JEM-2100, JEOL), while HR-TEM and STEM analyses were done on 300 keV S/TEM (Titan Themis G^2, FEI) and 200 kV S/TEM (JEM-2010F, JEOL). Acquired TEM micrographs were processed and interpreted by Digital Micrograph, ImageJ [67] and QGIS [68].

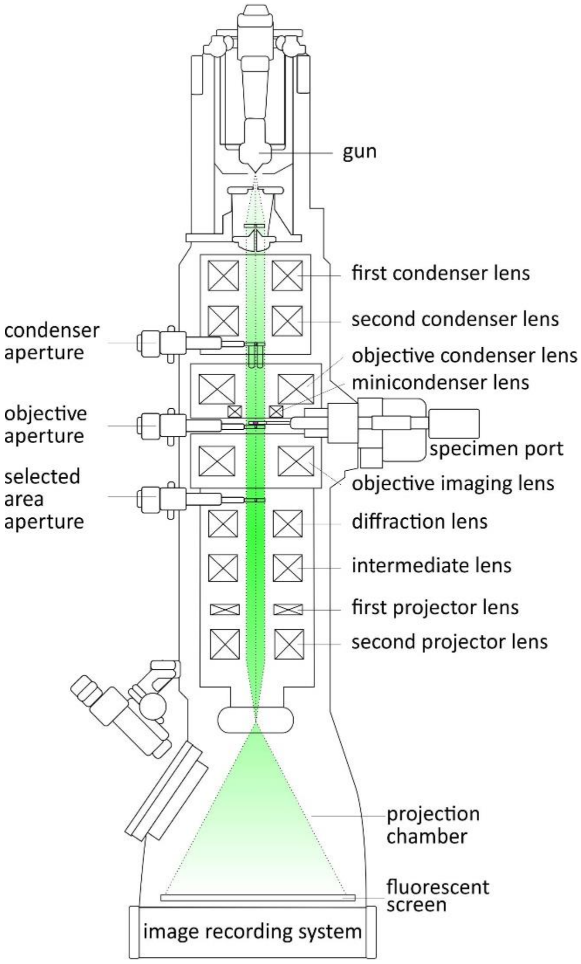

Figure 8: Schematic cross-section representation of a conventional TEM system with marked main elements; adopted from [64], [66].

3.2.5 Differential thermal analysis (DTA) and thermo-gravimetric analyses (TGA)

The thermal decomposition of the initial tungsten-based mixtures was studied by differential thermal analyses and thermogravimetric analyses (Netzsch Jupiter 449 simultaneous thermal analysis instrument coupled with Netzsch QMS 403C Aeolos quadrupole mass spectrometer).

Chapter 4

Results and Discussion

This chapter summarises the results of microstructural analysis and evaluation of W and W/W$_2$C composites for fusion applications. The results are presented in the form of articles published in international peer-reviewed topic-relevant scientific journals. The Results and Discussion part of the thesis are divided into three different topics that comprise three first-author articles. The first section of the Results and Discussion is presented by an article entitled *"The role of tungsten phases formation during tungsten metal powder consolidation by FAST: Implications for high-temperature applications"*. The article explores the methods for microstructure analysis and peculiarities of the FAST consolidation of the W powders. The second research topic is presented in the article entitled *"Tungsten carbide as a deoxidation agent for plasma-facing tungsten-based materials"*. The article summarises the optimisation of sintering processes and explores the use of tungsten carbide (WC) as a deoxidation agent for plasma-facing tungsten-based materials. The third research topic is presented in the article entitled *"Non-uniform He bubble formation in W/W$_2$C composite: Experimental and ab-initio study"*, which explores and evaluates the effect of He irradiation on the material presented in the first two articles.

The material was developed at the Jožef Stefan Institute, Department for Nanostructured Materials (K7, JSI) and was analysed on microscopes operated at the Centre for Electron Microscopy and Microanalysis (CEMM, JSI). The DT/TGA analyses were made in collaboration with researchers from Advanced Materials Department (K9, JSI). The He implantation experiments were performed at the Department for Low and Medium Energy Physics (F2, JSI). The DFT and other computational analyses were executed in collaboration with Max-Planck-Institut für Eisenforschung (MPIE, Düsseldorf, Germany).

4.1 The Role of Tungsten Phases Formation During Tungsten Metal Powder Consolidation by FAST: Implications for High-Temperature Applications

The following section presents an article entitled *"The role of tungsten phases formation during tungsten metal powder consolidation by FAST: Implications for high-temperature applications"*, authored by A. Šestan, P. Jenuš, S. Novak Krmpotič, J. Zavašnik, and M. Čeh, which was published in scientific journal *Materials Characterisation* [69].

Although many tungsten and tungsten-based materials are already reported, and well-described, the attempts to further optimise these materials for their use in fusion applications are ongoing. In this work, the challenges posed by oxygen accumulation during metal powder production and consolidation are addressed. The secondary phases formed during powder consolidation are nano-sized and scarce; therefore, the current approach to address this problem involves using several state-of-the-art characterisation techniques. Moreover, the main drawback of tungsten produced by FAST is the use of graphite parts that are in contact with W powder during the consolidation process. An external shell formed between W powder and graphite tool can be expected due to the carburisation of W powder [70].

After tungsten powder consolidation by FAST, we identified the presence of *bcc* W (Im-3m) [8] and secondary oxide phases, which were determined to be monoclinic WO_2 ($P2_1/c$) [71] located along tungsten grain boundaries. Although W should exhibit stability up to ~3695 K, the high-temperature experiment showed that the bulk material degradation starts already above 1800 K. We connected this premature degradation to W-oxide particulates embedded in bulk W. The *in-situ* formed external carbon-rich shell was recognised as a tungsten and tungsten carbide mixture. The article's subject addressed the wide scientific community as the presence of trace impurities plays an important role in metal manufacture and processing. The introduction of defects (porosity, inclusions, etc.) affects the dislocation movement in bulk, consequently influencing the materials' overall performance and physical properties.

My contribution to the article was: I designed the research and experiments and prepared the samples for the SEM and TEM analyses. For SEM-based analyses, I calculated the electron beam interaction as a function of accelerating voltage simulations, performed the chemical analyses by SEM-EDS, the crystallography analyses and identification of the phases present in the materials based on SAED and XRD raw data, the interpretation of the data and prepared the structural data for the SEM-EBSD analysis and data interpretation. I wrote the manuscript draft, coordinated the process between the co-authors and implemented their corrections and interpretation into the final version of the manuscript. I submitted the manuscript, prepared a revised version, coordinated the input from the co-authors, and published the research. A copy of the article and the article's s supplementary information are presented on the following pages.

Materials Characterization 138 (2018) 308–314

Contents lists available at ScienceDirect

Materials Characterization

journal homepage: www.elsevier.com/locate/matchar

The role of tungsten phases formation during tungsten metal powder consolidation by FAST: Implications for high-temperature applications

Andreja Šestan[a,b,*], Petra Jenuš[c], Saša Novak Krmpotič[c], Janez Zavašnik[a,d], Miran Čeh[a,b,c]

[a] *Centre for Electron Microscopy and Microanalysis, Jožef Stefan Institute, 1000 Ljubljana, Slovenia*
[b] *Jožef Stefan International Postgraduate School, 1000 Ljubljana, Slovenia*
[c] *Department for Nanostructured Materials, Jožef Stefan Institute, 1000 Ljubljana, Slovenia*
[d] *Max-Planck-Institut für Eisenforschung GmbH, 40237 Düsseldorf, Germany*

ARTICLE INFO

Keywords:
Fusion
FAST
Tungsten
Tungsten oxide
Electron microscopy
Microstructure

ABSTRACT

Tungsten is a candidate material for the demonstration fusion power plant DEMO. To ensure high density and structural stability, Field-Assisted Sintering Technique (FAST) is proposed as a consolidation method. This study discusses the formation of phases during sintering of tungsten by the FAST. Scanning electron microscopy, X-ray diffraction and transmission electron microscopy were used to evaluate the microstructure in tungsten-based materials. The results of microscopic examinations revealed the *in-situ* formation of tungsten oxide and a formation of tungsten carbide shell around tungsten core. Tungsten carbide-rich shell is formed due to the carbon diffusion from the graphite die used in the FAST into tungsten at high temperatures. In contrast to easy removal of tungsten carbide shell by mechanical grinding, the formation of tungsten oxide in the W-matrix can influence the performance of such material when used as plasma-facing material in the fusion reactor. High-temperature experiments at 1873 K showed that tungsten-oxide phase starts to decompose, which results in material degradation and formation of voids and surface blisters.

1. Introduction

It is expected that fusion power will significantly contribute to clean and safe energy supply for future generations [1]. To achieve high efficiency and safe operation of future fusion power plants, researchers are putting much effort into the selection and optimisation of suitable functional materials capable of withstanding the extreme conditions within the fusion reactor [2]. One of the key challenges is to find a suitable plasma-facing material for the divertor [3], which will be exposed to high transient thermal events, neutron irradiation and helium and hydrogen isotopes irradiation. Tungsten (W) is a promising material for fusion applications due to its high melting point (3695 K), high thermal conductivity (174 $\mathrm{Wm^{-1}\,K^{-1}}$ at 300 K), low thermal expansion coefficient ($4.32 \times 10^{-6}\,\mathrm{K^{-1}}$ at 300 K), low sputtering yield and low tritium retention [4]. Its main disadvantage is relatively poor oxidation resistance; hence, hydrogen reduction atmosphere or vacuum conditions during sintering are required. Vacuum-assisted sintering is used to provide, oxygen-free atmosphere, reduced adsorption of oxygen on the surface of starting W powder, which should consequently result in a defect-free single phase tungsten microstructure. This type of sintering effects the mechanical properties of tungsten by improvement in hardness, yield strength and ultimate tensile strength [5]. Densification of W by a conventional solid-state sintering process in the reductive atmosphere requires high temperatures and lengthy sintering time due to the high melting point of W. However, this often results in W microstructure with an included porosity which will decrease the mechanical properties, such as strength at elevated temperatures [2,4]. To improve the material's density, additional processing such as forging, swaging or rolling is required [4,5].

Recently, an alternative sintering method, named ***Field-Assisted Sintering Technique*** (FAST), was proposed to improve the sinterability of W and to minimise grain growth during the sintering process. FAST offers vacuum environment under uniaxial compression and rapid consolidation of powders, which are heated directly by a low-voltage, high-intensity current flowing through the die and through the sample itself [5–7]. Short sintering time, the order of magnitude shorter than in conventional sintering prevents or minimises tungsten grain growth during the sintering [5–7]. Finer grain size can improve mechanical properties, such as microhardness and bending strength [2]. Furthermore, sintering under an applied pressure leads to higher materials' densities. However, FAST sintering of W has also some drawbacks, such as the formation of the external shell from the FAST graphite tooling

---

* Corresponding author.
E-mail addresses: andreja.sestan@ijs.si (A. Šestan), petra.jenus@ijs.si (P. Jenuš), sasa.novak@ijs.si (S.N. Krmpotič), janez.zavasnik@ijs.si (J. Zavašnik), miran.ceh@ijs.si (M. Čeh).

https://doi.org/10.1016/j.matchar.2018.02.022
Received 5 December 2017; Received in revised form 14 February 2018; Accepted 14 February 2018

setup [7]. Moreover, secondary phases, if formed during the FAST sintering of tungsten, are usually nano-sized and scarce; therefore, their detection and identification may be rather difficult. Nevertheless, the identification of such phases and their structural stability at elevated temperatures is a prerequisite for materials used in fusion plasma-applications [2]. The normal operation temperature of tungsten is currently thought to be limited on one side by the ductile to brittle transition temperature (DBTT), which defines the minimum operation temperature, and the recrystallization of W, which on the other side defines an upper limit in the range of ~1473–1573 K [8]. The presence of impurities, such as trace amounts of oxygen (30 ppm) in tungsten can lead to the formation of a second phase at the grain boundary and consequently lead to embrittlement and increased the DBTT [9]. The “burst out” of the plasma (plasma disruption and ELMs) during fusion reactor operation is considered as a severe accident during off-normal operation condition and needs to be avoided or at least mitigated as far as possible. Thermal overloading by such undesirable, but maybe not entirely avoidable, transient events in experimental prototypes such as ITER will be discarded on the divertor [2]. The expected temperature gradient within the limited volume near the loaded material surface during off-normal events, such as ELMs will be in the range of hundreds to several thousand Kelvin, but still below the melting limit of tungsten [2,6,8]. Currently suggested reinforcing secondary phases (such as La_2O_3 [10]) in W-based materials have a far lower melting point than tungsten, so during disruptions this can lead to early melting and increased evaporation, causing the formation of pores and depleted surface layer [2]. The presence of oxide particles with a lower melting point as tungsten has a negative effect on the erosion resistance and can be potentially replaced by carbide dispersoids with higher melting point (such as HfC) [5]. In the present study, we first characterise and then discuss the formation of secondary phases formed during the FAST sintering of W powder, carried out at 2173 K and 60 MPa. To investigate the high-temperature structural stability of the phases formed during FAST, we performed the additional thermal treatment at 1873 K to investigate how the secondary phase decomposition affects the microstructure of W.

2. Materials and Methods

2.1. Sample Preparation

A commercially available 99.9% pure tungsten powder with an average grain size of 0.7 μm (MPO7R; Global Tungsten & Powder, USA) was used as a starting material. For sintering experiments, we employed field-assisted sintering device (FAST; Dr. SINTER SPS SYNTEX 3000, Fuji Electronic Industrial, Japan). The W powder was loaded into a graphite die (inner diameter 16 mm), while additional 0.3 mm graphite foil was used to prevent adhesion of the W on the die wall (Fig. 1). Prior to sintering the FAST chamber was thoroughly purged with N_2 (99.996% pure) and evacuated (0.3 mbar–0.5 mbar). The samples were sintered at an applied pressure of 60 MPa with a heating rate of 100 K/min. To investigate the effect on microstructure, sintering time was 5 min (sample W1) and 10 min (W10).

To verify the structural stability of FAST sintered W at high temperatures, additional thermal treatments were performed in a high-temperature vacuum furnace (Astro, Thermal Technology LLC., USA) at 1873 K for 30 min or 24 h with 5 K/min heating rate. Before each experiment, the furnace was thoroughly purged with Ar (99.998% pure) and evacuated (0.2 mbar–0.35 mbar). The samples' surface was mechanically ground and polished before additional thermal treatments. To prevent carbon contamination, tungsten die was used.

2.2. Material Characterisation

For the characterisation of as-received tungsten powder, we used X-ray powder diffraction analysis, using CuKα radiation at room temperature (XRD; AXS D4 Endeavor, Bruker AXS GmbH, Germany). The other details for all the characterised samples are as follows: 20° to 80° 2θ range, step size 0.02, and 1 s per channel acquisition time. The diffracted (*hkl*) planes of reference W (ICSD collection code #167904) [11] are shown in Fig. 2 on the top of each peak. The W powder morphology was assessed with a field-emission scanning electron microscope (FE-SEM, JSM-7600F, Jeol Inc., Japan). Carbon tap was used for powder mounting on the holder. After FAST treatment, the graphite foil from the wrapping was removed by surface grinding. The crystal structure from the surface layer - carbon-contaminated layer induced by graphite die used during FAST, was evaluated by X-ray diffraction (Fig. 3a). Before the bulk sintered samples were analysed by XRD to evaluate the phase-composition (Fig. 3b), the contaminated surface layer was removed by grinding and polishing. Microstructural observation and chemistry of the synthesised product were assessed by FE-SEM. The chemical composition of the secondary phases was studied by energy-dispersive X-ray spectroscopy (EDS; X-Max, Oxford Instruments plc., UK), while their microstructure and crystallinity were studied by electron-backscatter diffraction (EBSD; Nordlys II, Oxford Instruments plc., UK) (Figs. 4 and 7). Samples for FE-SEM, EDS and EBSD analyses were prepared by mechanical grinding and polishing. To achieve an adequate surface quality and to remove a mechanically-induced damaged layer, a final polishing with 5 vol% H_2O_2 solution in colloidal silica was applied. Before high-temperature structure-stability tests, the surface of the samples was prepared by mechanical grinding and polishing. Due to the detection limit of the laboratory XRD machines [12], co-formed secondary phases were additionally investigated by transmission electron microscopy (TEM, JEM-2100, Jeol Inc., Japan) and scanning transmission electron microscopy (S/TEM, JEM-2010F, Jeol Inc., Japan). STEM images were obtained in Schottky-type field emission electron gun TEM, equipped with UHR pole piece (Cs = 0.48 mm, focal spread Δf = 8 nm), while the inner and outer annular angles for the HAADF detector were set by the optical settings of the microscope to 100 mrad and 200 mrad, respectively, while the probe semi-angle was 20 mrad. Prior to TEM observation (Figs. 5 and 6), the samples were prepared by conventional mechanical thinning and subsequently etched in ion-mill using high-energy Ar^+ until electron transparency (PIPS 691, Gatan Inc., USA).

3. Results and Discussion

3.1. Phase Identification

Grain size and morphology of the starting W powder were investigated by FE-SEM. From secondary electron images in SEM (SEI-SEM) we assessed that the size of the starting tungsten particles was < 1 μm. Tungsten particles tend to form larger agglomerates (Fig. 2a). W particles exhibit an irregular shape. XRD diffractogram of initial powder corresponds to pure tungsten with body-centered cubic structure (a = 3.165 Å, Im-3 m SG: 229) [11] (Fig. 2b). Very narrow diffraction peaks indicate crystalline material and particle size in the micron range.

During the FAST consolidation of the W powder, carbon diffuses from the graphite foil and die into the sample, forming two additional layers on the surface of the sintered specimen as shown in Fig. 1. While the first layer is a thin graphite foil from the wrapping that can be removed easily, the second layer, which has a different texture, is a hard, thick crust, enclosing the W sintered sample (Fig. 3a1). XRD analysis (Fig. 3a) revealed that this second layer is a mixture of W [11] and $W_2C_{0.85}$ [13]. The investigation of the fractured sample showed that this carburised layer is approximately 200 μm thick (Fig. 3a1), and that it is formed during sintering due to direct contact of the specimen with the graphite-foil and graphite die; this carburised layer is assumed to grow in a parabolic manner with time [7]. The thickness of this tungsten carbide-rich layer is important regarding the further sample preparation, before any microstructure characterisation, this remaining

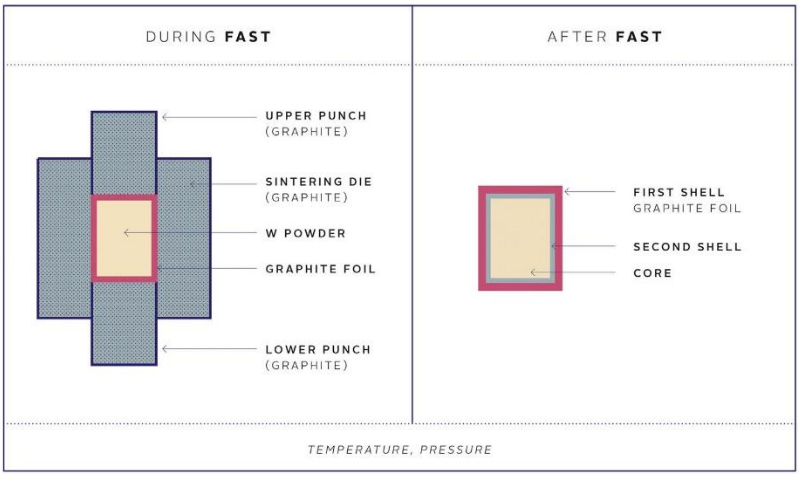

Fig. 1. Schematic representation of the FAST die and sample during and after consolidation.

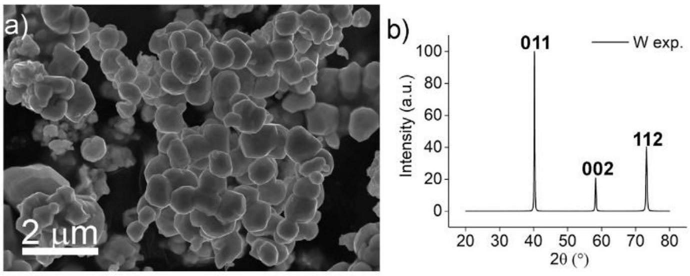

Fig. 2. a) SEI image of starting W powder, b) experimental X-ray diffractogram of starting W powder (W exp.).

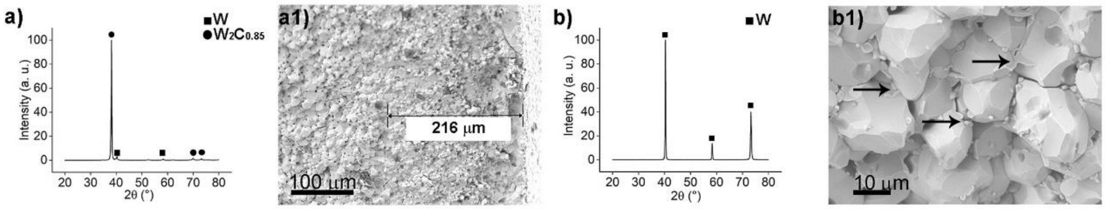

Fig. 3. a) Experimental X-ray diffractogram of the second layer, a1) fractured W1 sintered sample after the graphite foil has been removed from the surface, showing outer tungsten carbide-rich layer surrounding the W-core, b) X-ray diffractogram of the W-core and b1) W-core with a secondary phase (marked with arrows).

processing artefact has to be removed to avoid possible misinterpretation of the results.

After removal of the carburised layer, close-up inspection of the pellets' core revealed W-matrix grains with a small fraction of secondary phase in the shape of small grains along grain boundaries of W grains (Fig. 3b1). An attempt to identify the unknown phase by XRD analysis was not successful, as the only phase detected is the bcc-W of the matrix [11], meaning that the overall concentration of the secondary phase is below the detection limit of the laboratory XRD (Fig. 3b). In an attempt to increase grain growth of the observed unknown phase, we extended the FAST sintering time to 10 min, while other conditions ($P = 60$ MPa, $T = 2173$ K, $r = 100$ K/min) remained unaltered; again the carbide layer was ground away, and the microstructure of the tungsten pellet core was investigated by SEM. The prolonged sintering time at high temperature indeed resulted in merging and growth of neck-shaped unknown phase, which made it possible to identify it as an oxygen-rich W phase by semi-quantitative EDS mapping, as shown in Fig. 4. To avoid contamination and alteration of the sample, the surface was Ar^+ etched before analysis.

The morphology and crystal structure of this unknown oxide-rich W phase was further investigated by TEM. The initial overview of the W10 sample using bright-field TEM imaging (Fig. 5a, b) revealed the presence of individual W grains with a size of approximately 10 µm. No visible planar defects could be observed within the W grains (Fig. 6a). On the other hand, the oxygen-rich W phase exhibits ceramic-like Ar^+ etching patterns [14], which already makes it easy to distinguish it from the W grains. In general, two different types of oxygen-rich W phase could be observed; namely intragranular single-crystal oxygen-

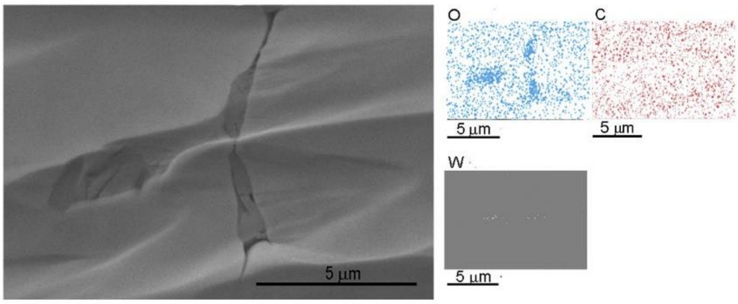

Fig. 4. a) Grain boundary secondary phase observed in the W10 sample (backscattered electron imaging in SEM) with the corresponding EDS mapping for O, C and W.

rich W phase with well-developed morphology and size of about 1 μm (Fig. 5a) and neck-like polycrystalline oxygen-rich W phase between individual tungsten grains (Fig. 5b), similar as observed already by SEM (Fig. 3). Both phases, namely W grains and the oxygen-rich W phase, can be even easier distinguished using HAADF STEM imaging (Fig. 5c, d), where the contrast in the image is contributed mainly by high angle, incoherently scattered electrons and thus the contrast of individual phase is approximately proportional to Z^2 [15].

Crystal structure of W-matrix was determined from selected area electron diffraction pattern (SAEDP). The diffraction pattern corresponds to W bcc (Im-3m (SG: 229) (Fig. 6a1) [11], which is in agreement with XRD analyses obtained from the starting powder and after the FAST treatment.

The crystal structure of the oxygen-rich W phase was determined to be a simple monoclinic WO_2 $P2_1/c$ (SG: 14) structure (Fig. 6b1) [16] by interpretation of single-crystal SAED patterns, recorded in different orientations. Fig. 6. present HR-TEM micrograph (Fig. 6c1) of the undisturbed WO_2 $P2_1/c$ (SG: 14) in [211] orientation with the further illustrated atomic structure model in [211] orientation (Fig. 6c2). Based on our structure determination we were able to prepare a database for

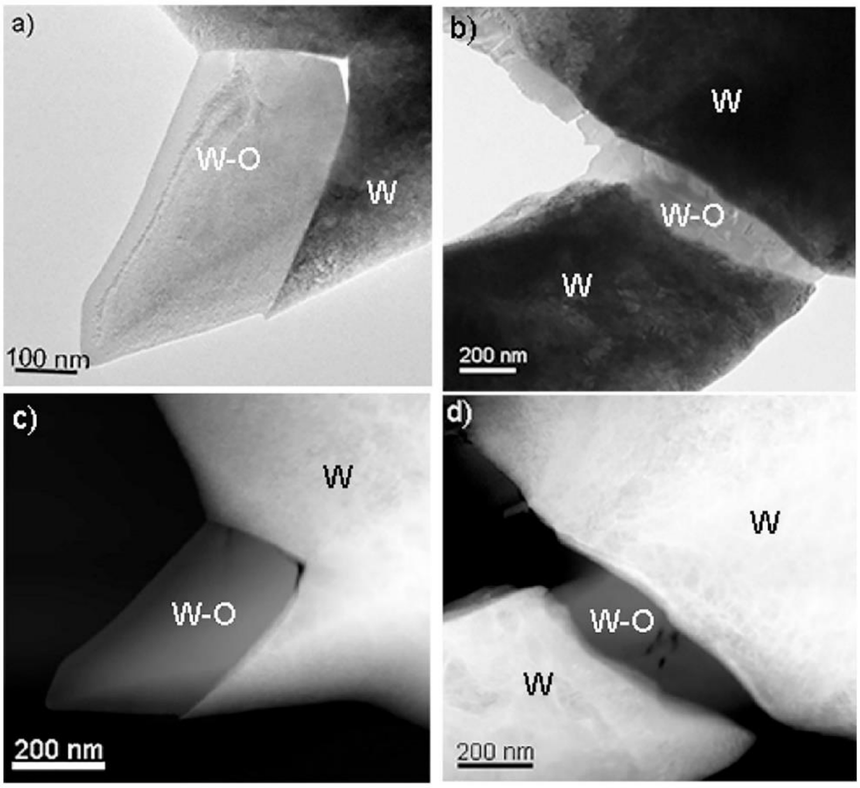

Fig. 5. (a, b) Bright-field TEM micrographs of W10 sample showing W grains and oxygen-rich W phase. The latter can be observed as a standalone crystalline phase or as neck-like grain boundary phase. (c, d) HAADF STEM micrographs are showing the same region as in a and b. The difference in contrast between W grains and oxygen-rich W phase is largely increased due to reduced average atomic number Z of the oxygen-rich W phase.

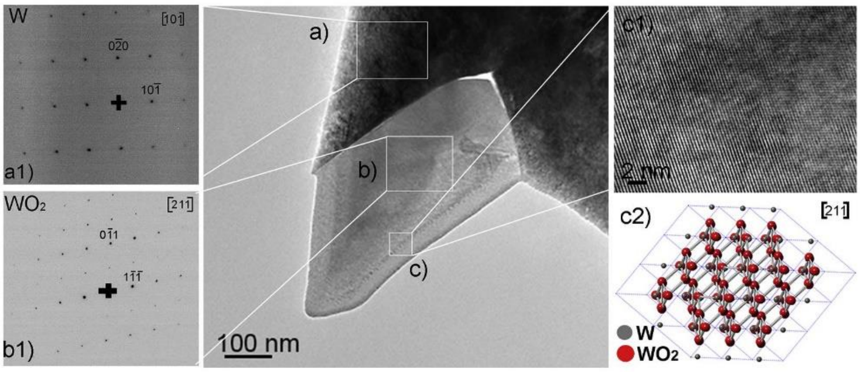

Fig. 6. BF-TEM micrograph and corresponding electron diffraction patterns (SAEDP) of the bcc W-matrix (a1) and monoclinic WO_2 (b1); HR-TEM of the WO_2 and corresponding structure model in the same orientation (c2).

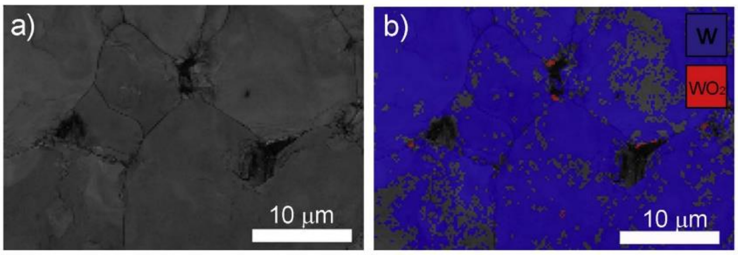

Fig. 7. Electron backscatter diffraction images of a) band contrast map, b) phase composition with distribution for cubic W (blue) and monoclinic WO_2 phase (red). (For interpretation of the references to colour in this figure legend, the reader is referred to the web version of this article.)

electron backscatter diffraction (EBSD) analyses as a way of phase recognition. Since the signal in the EBSD analysis depends on the crystal structure of the investigated grain, the resulting compositional map presents unique and precise information on spatial distribution of both W and WO_2 phases in the sample. Since the differentiation of the phases is based on two different structures: namely, cubic W and monoclinic WO_2, the resulting band contrast map allocates the grains and grain boundaries easily (Fig. 7a), while phase composition (Fig. 7b) shows the presence of WO_2 phase around W grains. It is necessary to mention that the preparation of the surface for EBSD analysis is crucial, since the diffracted electrons, forming the signal, originate only from a few ten nm thin surface region of W. With grinding and polishing mechanically induced deformation layer is formed, which must be removed by final finish polishing using chemical etchants, like H_2O_2. In the two phases system (W and WO_2), the main problem is preferential etching of oxide-rich W phase [5], which strongly affect the results. In work presented here the mechanically damaged layer was removed by etching with H_2O_2 for 15 min, which already removed most of the intra-granular WO_2 grains, but preserved most of the neck-like shaped WO_2 around W grains. The regions, which are not identified, are voids formed during the sintering process.

The presence of tungsten oxide phases in the FAST consolidated tungsten can enhance tungsten embrittlement, respectively a dramatic increase of the DBTT. Tungsten is sensitive to oxygen concentration at high temperature (1000–1600 K) and low oxygen pressure (1×10^{-6} Torr oxygen) [9,14]. The probable source of oxygen is the residual oxygen (water vapour or. humid air) in the sintering chamber or the oxygen present in the as-received W metal powder. The oxygen atoms from the water molecules diffuse into the tungsten metal, and form oxide compound [4] and the graphite dies can provide a reducing environment to reduce WO_3 to WO_2 [14]. Thus, to improve the performance of the tungsten processed by FAST, it is necessary to prevent the formation of tungsten oxide either by pre-processing of initial tungsten powder by H_2 reduction at atmospheric pressure [6] or by reducing oxygen content in a vacuum by using protective purging high-purity gas and by using higher vacuum [5]. The use of carbon deoxidation as a chemical reduction in a vacuum might lead to carbon contamination, and an even minor trace of it (36 ppm) can lead to the formation of the second phase and substantial increase of DBTT [9]. Base on this is necessary to prevent the carbon diffusion into the W bulk during FAST consolidation. Boron nitride is known to block carbon diffusion during FAST, but due to the high solubility of carbon in W, the reduction of the thickness of tungsten carbide layer was not achieved [7]. The re-design of the FAST liner and dies would lead to significantly higher production cost.

3.2. High-Temperature Structures Stability

To assess the suitability of the FAST sintered W as a material for fusion reactor divertor, we performed the high-temperature structure-stability test. The formed WO_2 phase has a much lower melting point compared to pure W (WO_2 = 1803 K, W = 3695 K [4]). Therefore, the temperature was set to 1873 K to determine the influence of WO_2 decomposition on bulk material. In the first experiment, the FAST sintered sample was held for 30 min at 1873 K in vacuum-furnace. At this temperature, the recrystallisation of mechanically induced deformation layer started (Fig. 8a). During this process, a set of defect-free smaller grains are formed while outlines of initial grain are still visible. The miss-orientation of individual grains is visible due to the channelling effect on backscattered electron images (Fig. 8a). After 30 min of high-temperature exposure, the material surface starts to degrade; voids are formed at the W grain-boundaries and blisters bursting on the surface

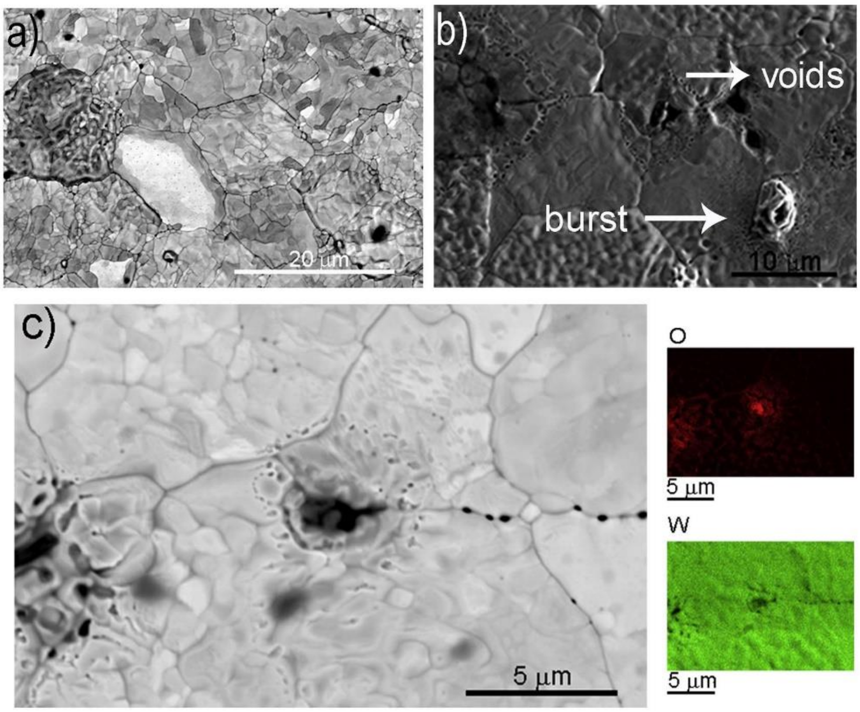

Fig. 8. a) Electron backscatter image of the mechanical induce deformation layer after ageing. b) Voids and outbursting are visible on the grain boundary of the W sample after annealing (SEI-SEM) with c) the corresponding EDS mapping for O and W.

(Fig. 8b), where the tungsten oxide grains were, before annealing (Fig. 8c).

In the second high-temperature experiment, the annealing time was increased from 30 min to 24 h at 1873 K. The main difference was the total absence of W-oxides particle's at the grain boundaries (Fig. 9).

Under accident condition ergo under off-normal operation regime in the fusion reactor, if the temperature will increase above the melting point of WO_2 the surface degradation of the material will occur.

4. Conclusion

In-situ secondary phases formation during tungsten powder consolidation in FAST must be taken into account when considering fusion applications. Due to the low concentration of secondary phases in the sample, the information obtained from imaging, electron diffraction and microanalysis have to be combined to allow detailed insight into the properties and behaviour of such composites. The two-phase system was identified in the FAST sintered W samples *via* structural and chemical characterisation performed by SEM and TEM, and the corresponding cubic W and monoclinic WO_2 structures were determined. *In-situ* formation of the secondary phase, WO_2, can be attributed to the level of impurities (mainly oxygen content) in the starting W powder and residual oxygen in the furnace. In the FAST furnace, the presence of high current [5] may affect phase transformation temperature, nucleation and grain growth rates and deformation behaviours of material, leading to morphological differences of WO_2 (*e.g.* intragranular single-crystal WO_2 and neck-like polycrystalline W-oxide).

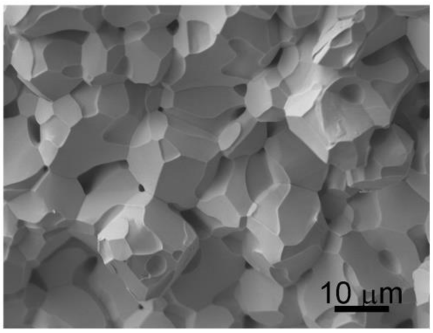

Fig. 9. SEM micrograph of the fractured surface of the sample after ageing at 1873 K for 24 h.

During phase-stability tests at 1873 K, the WO_2 phase formed in W-matrix starts to decompose. At holding times higher than 30 min, the material' degradation starts. Namely, blisters and voids form at the positions of WO_2 grains. With the holding time of 24 h, a complete absence of WO_2 particles at the W-grains was observed.

Acknowledgements

This work has been carried out within the framework of the EUROfusion Consortium and has received funding from the Euratom research and training programme 2014–2018 under grant agreement No 633053. The views and opinions expressed herein do not necessarily reflect those of the European Commission. Mr. Matej Kocen (Jožef Stefan Institute and Jožef Stefan International Postgraduate School) is acknowledged for assisting with the experimental part.

References

[1] D. Maisonnier, D. Campbell, I. Cook, L. Di Pace, L. Giancarli, J. Hayward, A. Li Puma, M. Medrano, P. Norajitra, P. Sardain, M.Q. Tran, D. Ward, Power plant conceptual studies in Europe, Nucl. Fusion 47 (11) (2001) 1524–1532.

[2] G. Pintsuk, R.J.M. Konings (Ed.), Comprehensive Nuclear Materials 4.17 - Tungsten as a Plasma-Facing Material, 4 Elsevier, Oxford, 2012, pp. 551–581.

[3] A.S. Kukushkin, H.D. Pacher, G. Janeschitz, A. Loarte, D.P. Coster, G. Matthews, D. Reiter, R. Schneider, V. Zhogolev, Basic divertor operation in ITER-FEAT, Nuclear Fusion 42 (2002) 187–191.

[4] E. Lassner, W.-D. Schubert, Tungsten: Properties, Chemistry, Technology of the Element, Alloys, and Chemical Compounds, Springer US, New York, 1999.

[5] Z.Z. Fang, Sintering of Advanced Materials, Elsevier Science, 2010.

[6] J. Choi, H.-M. Sung, K.-B. Roh, S.-H. Hong, G.-H. Kum, H.-N. Han, Fabrication of sintered tungsten by spark plasma sintering and investigation of thermal stability, Int. J. Refract. Met. Hard Mater. 69 (2017) 164–169.

[7] G. Lee, J. McKittrick, E. Ivanov, E.A. Olevsky, Densification mechanism and mechanical properties of tungsten powder consolidated by spark plasma sintering, Int. J. Refract. Met. Hard Mater. 61 (2016) 22–29 no. Complete.

[8] J.W. Coenen, S. Antusch, M. Aumann, W. Biel, J. Du, J. Engels, S. Heuer, A. Houben, T. Hoeschen, B. Jasper, F. Koch, J. Linke, A. Litnovsky, Y. Mao, R. Neu, G. Pintsuk, J. Riesch, M. Rasinski, J. Reiser, M. Rieth, A. Terra, B. Unterberg, T. Weber, T. Wegener, J.-H. You, C. Linsmeier, Materials for DEMO and reactor applications—boundary conditions and new concepts, Phys. Scr. T167 (2016) 014002.

[9] J.R. Stephens, “Effects of Interstitial Impurities on the Low-Temperature Tensile Properties of Tungsten,” NASA Technical Note D-2287, Washington, D. C. (1964).

[10] A. Muñoz, M.A. Monge, B. Savoini, M.E. Rabanal, G. Garces, R. Pareja, La_2O_3-reinforced W and W–V alloys produced by hot isostatic pressing, J. Nucl. Mater. 417 (1–3) (2011) 508–511.

[11] A. Friedrich, B. Winkler, L. Bayarjargal, A. Juarez, A. Erick, W. Morgenroth, J. Biehler, F. Schroeder, J. Yan, S.M. Clark, In situ observation of the reaction of tantalum with nitrogen in a laser-heated diamond anvil cell, J. Alloys Compd. 42 (17) (2010) 5–12.

[12] B.D. Cullity, Elements of X-ray diffraction, J. Chem. Educ. 34 (4) (1957) 178.

[13] A. Harsta, S. Rundqvist, J.O. Thomas, A neutron powder diffraction study of W_2C, Acta Chem. Scand. 32 (1987) 891–892.

[14] L. Huang, L. Jiang, T.D. Topping, C. Dai, X. Wang, R. Carpenter, C. Haines, J.M. Schoenung, In situ oxide dispersion strengthened tungsten alloys with high compressive strength and high strain-to-failure, Acta Mater. 122 (2017) 19–31.

[15] R. Brydson, L.M. Brown, Development of STEM, In Aberration-Corrected Analytical, John Wiley & Sons Ltd., Chichester, 2011, pp. 39–53.

[16] D.J. Palmer, P.G. Dickens, Tungsten dioxide: structure refinement by powder neutron diffraction, Acta Crystallogr. Sec. B 35 (9) (1979) 2199–2201.

Supplementary data

The role of tungsten phases formation during tungsten metal powder consolidation by FAST: Implications for high-temperature applications

Andreja Šestan [1, 2], Petra Jenuš [3], Saša Novak Krmpotič [3], Janez Zavašnik [1, 4], Miran Čeh [1, 2, 3]

[1] Centre for Electron Microscopy and Microanalysis, Jožef Stefan Institute, 1000 Ljubljana, Slovenia

[2] Jožef Stefan International Postgraduate School, 1000 Ljubljana, Slovenia

[3] Department for Nanostructured Materials, Jožef Stefan Institute, 1000 Ljubljana, Slovenia

[4] Max-Planck-Institut für Eisenforschung GmbH, 40237 Düsseldorf, Germany

1. Calculating penetration depth of the electrons into W for the EBSD analyses

For EBSD analyses, high quality of the sample surface is demanded. Since EBSD signal originates in sample's crystal structure, the main priority is to avoid the mechanical defects, induced during sample grinding and polishing. According to our simulations, in bulk W sample majority of the EBSD signal originates in the depth of 0-50 nm, hence high demands for removing the deformation layer that formed during grinding and polishing.

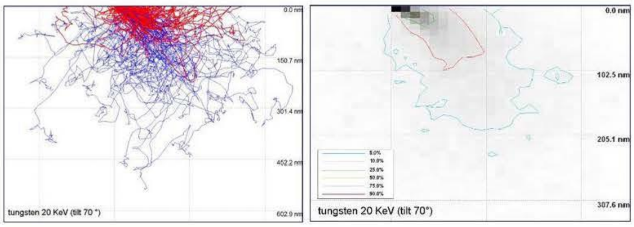

Simulation conditions:
Monte Carlo program CASINO @ 20 kV, beam radius 10 nm
Analytical model of tungsten substrate

Figure 1: Calculated penetration depth of the electrons into the W sample at operating accelerating voltage (20 keV) is approximately 50 nm.

Software used: Casino Monte Carlo simulation for e-beam/sample interactions. [1]

2. Simulation of EDS spectra for the W-C-W_2C composites

Reliable EDS analysis on the mixed W, C and W_2C materials is challenging, since besides a large difference in k-factors, the main problem arises due to the overlapping of tungsten N-lines (N4 255.9 eV, N5 243.5 eV) with carbon K-line (298.2 eV). Although this can be taken into account for spot analysis by proper calibration using standards in a similar manner as for WDS analysis, for the appropriate EDS mapping of individual element therefore we had to limit the energy-window, used for mapping, to very narrow slit.

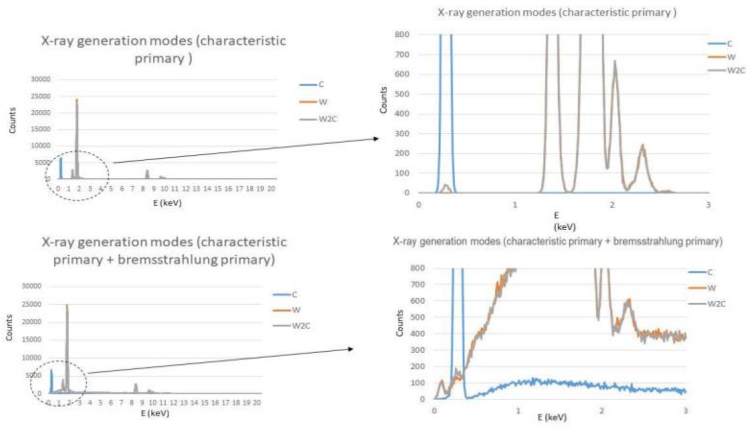

Figure 2: A simulation of C, W and W_2C EDS spectra (left) with the inserted simulated spectra from 0-3 keV.

Software used for simulation: NIST DTSA-II by Material Measurement Laboratory [2].

3. Diffraction patterns of different tungsten dioxide

Table 1: d-values calculated from experimental TEM-SAEDP.

	Measured R_i (Å)	Calculated d_i (Å)	Calculated d-values WO_2 $P2_1/c$ (reference)	*hkl* WO_2 $P2_1/c$	*Ref.* d-values WO_2 $P2_1/c$
R_1	5.78	3.4(6)	3.4542	-111	[3]
R_2	5.83	3.4(3)	3.4542	011	[3]
R_3	18.49	1.0(8)	1.0906	240	[3]
Zone axis				211	

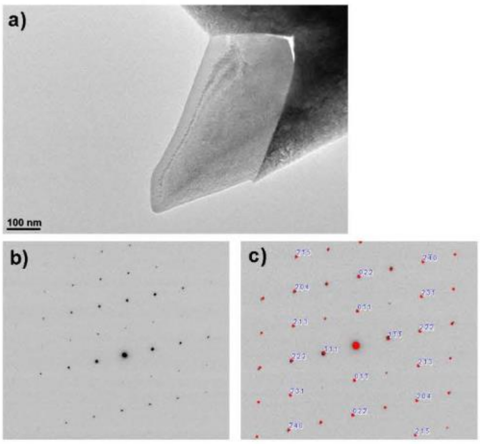

Figure 3: BF-TEM micrograph (a) with the corresponding electron diffraction pattern (SAEDP) of WO2 (b) and simulated electron diffraction pattern of monoclinic $P2_1/c$ [4] crystal system (c).

Table 2: Experimental d-values calculated from TEM-SAEDP and reference d-values for different crystal systems of WO_2.

Crystal system	Space group (SG)	SG number	Calculated d-values (reference)	*hkl*	Calculated d-values	ICSD collection code	Ref. ICSD collection code
					3.4(6)		
tetragonal	$P4_2/mnm$	136	3.4400	110		#647647	[5]
orthorhombic	Pnma	62	3.815	111		#74774	[6]

Crystal system	Space group (SG)	SG number	Calculated d-values (reference)	*hkl*	Calculated d-values	ICSD collection code	Ref. ICSD collection code
					3.4(3)		
tetragonal	$P4_2/mnm$	136	/	/		#647647	[5]
orthorhombic	Pnma	62	/	/		#74774	[6]

Crystal system	Space group (SG)	SG number	Calculated d-values (reference)	*hkl*	Calculated d-values	ICSD collection code	Ref. ICSD collection code
					1.0(8)		
tetragonal	$P4_2/mnm$	136	2.39	101		#647647	[5]
orthorhombic	Pnma	62	2.1666	231		#74774	[6]

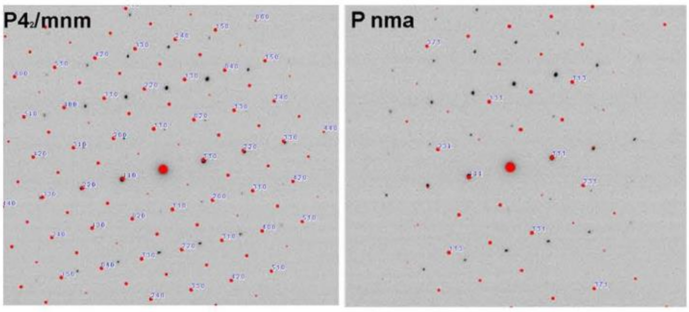

Figure 4: Comparison between simulated electron diffraction pattern of WO_2 for tetragonal $P4_2/mnm$ [5] and orthorhombic Pnma [6] crystal system (red), superimposed on experimental data (black).

Software used for simulation: Crystallography software CrystalMaker® [7].

4. Multiple phases in the W-C system. X-ray simulations of crystal system of W_2C.

Table 3: Literature date for W_2C crystal system and W crystal system.

Crystal system	Space group (SG)	SG number	Chemical formula	ICSD collection code
trigonal/rhombohedral	P -3m1	164	W_2C	167897 [8]
orthorhombic	P bcn	60	W_2C	167898 [8]
trigonal/rhombohedral	P -31m	162	$W_2C_{0.85}$	167900 [8]
hexagonal	P 63/mmc	194	W_2C	185937 [9]
cubic	I m-3m	229	W	167904 [10]

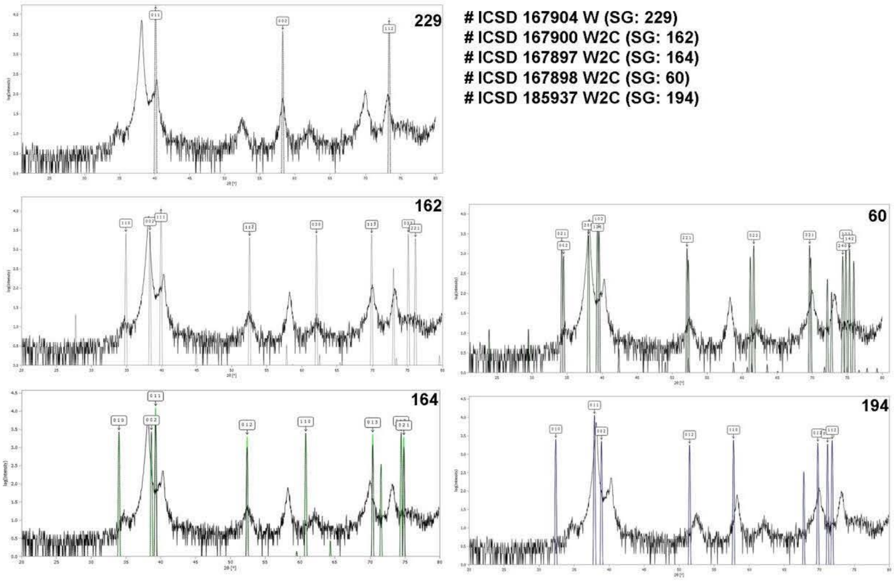

Figure 5: Simulations of diffraction peaks from the corresponding calculated d-values for W and W_2C from reference data.

Software reference: *Crystallography software* CrystalMaker® [7].

References

[1] R. Gauvin, "Casino Monte Carlo simulation for e-beam/sample interactions. The Monte Carlo program CASINO has been programmed by the research team of Raynald Gauvin (Ph.D., Full professor at Université de Sherbrooke, Québec, Canada). Version 2.0 of the simulation soft," [Online]. Available: URL. http://www.gel.usherb.ca/casino.

[2] N. Ritchie, "Spectrum Simulation in DTSA-II," *Microscopy and Microanalysis,* vol. 15, no. 5, pp. 454-468, 2009.

[3] A. Magneli, G. Andersson, B. Blomberg and L. Kihlborg, "PDF card 5-452," *Analytical Chemistry,* vol. 1998, p. 24, 1952.

[4] A. A. Bolzan, B. J. Kennedy and C. J. Howard, "Neutron powder diffraction study of molybdenum and tungsten dioxides," *Australian Journal of Chemistry,* vol. 48, pp. 1473-1477, 1995.

[5] V. M. Goldschmidt, T. Barth, D. Holmsen, G. Lunde and W. Zachariasen, "Geochemische Verteilungsgesetze der Elemente. VI. Ueber die Krystallstrukturen vom Rutiltypus, mit Bemerkungen zur Geochemie zweiwertiger und vierwertiger Elemente," *Skrifter utgitt av det*

Norske Videnskaps-Akademi i Oslo 1: Matematisk-Naturvidenskapelig Klasse, vol. 1926, no. 1, pp. 5-21, 1926.

[6] M. R. Sundberg, P. E. Werner and I. P. Zibrov, "X-ray powder crystal structure analysis of high pressure tungsten dioxide. On the information in weak reflections," *Zeitschrift fuer Kristallographie (1979-2010),* vol. 209, pp. 662-666, 1994.

[7] D. C. Palmer, "CrystalMaker," *CrystalMaker Software Ltd,* Vols. Begbroke, Oxfordshire, England, 2014.

[8] Y.-F. Li, Y.-M. Gao, B. Xiao, T. Min, Z.-J. Fan, S.-Q. Ma and L.-L. Xu, "Theoretical study on the stability, elasticity, hardness and electronic structures of W-C binary compounds," *Journal of Alloys and Compounds,* vol. 502, pp. 28-37, 2010.

[9] F. Z. Abderrahim, H. I. Faraoun and T. Ouahrani, "Structure, bonding and stability of semi-carbides M2 C and sub-carbides M4 C (M= V, Cr, Nb, Mo, Ta, W)," *Physica B, Condensed Matter,* vol. 407, no. 18, pp. 3833-3838, 2012.

[10] A. Friedrich, B. Winkler, L. Bayarjargal, E. A. Juarez Arellano, W. Morgenroth, J. Biehler, F. Schroeder, J.-Y. Yan and S. M. Clark, "In situ observation of the reaction of tantalum with nitrogen in a laser heated diamond anvil cell," *Journal of Alloys and Compounds,* vol. 502, pp. 5-12, 2010.

4.2 Tungsten Carbide as a Deoxidation Agent for Plasma-Facing Tungsten-Based Materials

This section presents the optimisation of sintering processes and explores tungsten carbide as a deoxidation agent for plasma-facing tungsten-based materials. The results are presented via the scientific article entitled *"Tungsten carbide as a deoxidation agent for plasma-facing tungsten-based materials",* authored by A. Šestan, J. Zavašnik, M. Maček Kržmanc, M. Kocen, P. Jenuš, S. Novak, M. Čeh, and G. Dehm. The article was published in the *Journal of Nuclear Materials* [72].

In this article, the high-temperature consolidation in a vacuum using a field-assisted sintering technique discloses the *in-situ* formation of a secondary tungsten-oxide phases in the tungsten matrix during consolidation process. In this research, trace amounts of oxide impurities were identified and successfully removed during sintering by *in-situ* reduction through WC decomposition, acting as a source of carbon. The oxide impurities will be removed in the form of CO and CO_2. A surplus amount of WC in the powder mixture leads to the formation of a thermally stable ε-W_2C [34] as a secondary phase after high-temperature powders mixture consolidation (2173 K), following the reaction [73]:

$$aW + bWC \rightarrow (a\text{-}b)W + bW_2C$$

Based on thermodynamic and kinetic considerations, we set the optimum theoretical amount of WC in primary powders to prevent the *in-situ* formation of tungsten dioxide. To completely remove the oxygen impurities from the W body, at least 5.8 – 8.8 vol % WC must be introduced into the initial powder mixture, which was calculated based on the thermodynamically preferred reaction that can occur during FAST processing:

$$W + O_2 = WO_2$$
$$2WC + WO_2 \rightarrow 3W + 2CO$$
$$WC + WO_2 \rightarrow 2W + CO_2$$

In the article, we show that the high-temperature vacuum consolidation by field-assisted sintering technique (FAST) can be successfully used to produce tungsten-based composite materials with a very high melting point, relevant for plasma-facing applications.

In the scope of the research article, my article contribution was: I designed the research and experiments and performed the SEM, EBSD, and TEM sample preparation. I performed the chemical analyses by SEM-EDS and crystallography analysis of the phases by SEM-EBSD, and data interpretation. I performed thermodynamic calculations and DTA-TG data interpretation. I wrote a manuscript draft, coordinated the input from the co-authors, and prepared the revised version of the manuscript. I assembled the final revised version, submitted it, and published the research. A copy of the article and the article's s supplementary information are presented on the following pages.

Journal of Nuclear Materials 524 (2019) 135–140

Contents lists available at ScienceDirect

Journal of Nuclear Materials

journal homepage: www.elsevier.com/locate/jnucmat

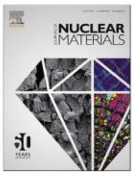

Tungsten carbide as a deoxidation agent for plasma-facing tungsten-based materials

Andreja Šestan [a, b, c], Janez Zavašnik [c, d, f, *], Marjeta Maček Kržmanc [e], Matej Kocen [b, f], Petra Jenuš [f], Saša Novak [f], Miran Čeh [a, b, f], Gerhard Dehm [c]

[a] Centre for Electron Microscopy and Microanalysis, Jožef Stefan Institute, 1000, Ljubljana, Slovenia
[b] Jožef Stefan International Postgraduate School, 1000, Ljubljana, Slovenia
[c] Max-Planck-Institut für Eisenforschung GmbH, 40237, Düsseldorf, Germany
[d] Gaseous Electronics, Jožef Stefan Institute, 1000, Ljubljana, Slovenia
[e] Advanced Materials Department, Jožef Stefan Institute, 1000, Ljubljana, Slovenia
[f] Department for Nanostructured Materials, Jožef Stefan Institute, 1000, Ljubljana, Slovenia

HIGHLIGHTS

- W-oxide phase formation from oxygen impurities during FAST.
- WC nanoparticles capacity to remove W-oxide phase.
- Surplus amount of WC will lead to the formation of W_2C phase.

GRAPHICAL ABSTRACT

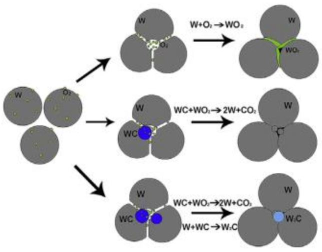

ARTICLE INFO

Article history:
Received 16 April 2019
Received in revised form
29 May 2019
Accepted 18 June 2019
Available online 20 June 2019

Keywords:
Tungsten
Tungsten carbide
Tungsten oxide
FAST
FUSION

ABSTRACT

Tungsten (W) and various composites are being considered as the primary plasma-facing materials for fusion reactors. Like all engineering materials, they contain certain levels of impurities, which can have an important impact on mechanical properties. In the present work, oxygen was identified as a major impurity in our starting tungsten powder. At elevated temperatures, the presence of interstitial elements such as oxygen leads to the formation of an oxide-rich tungsten phase at the tungsten grain boundaries. In this study, we determined the capacity of tungsten carbide (WC) nanoparticles to remove the oxide impurities from a tungsten body. Tungsten composites with 0.05, 0.25 and 0.51 wt. % carbon (C) in the form of WC were sintered using a field-assisted sintering technique (FAST) at 1900 °C for 5 min. The sintered samples were characterized using field-emission scanning and transmission electron microscopy. Thermodynamic and kinetic considerations allowed us to determine the optimum theoretical amount of WC to prevent the *in-situ* formation of WO_2.

1. Introduction

Nuclear fusion is one of the most promising, clean and safe energy-producing technologies for future generations [1]. The extreme conditions in a fusion reactor require the development of suitable materials to achieve the highest possible resistance to heat,

---

* Corresponding author. Jožef Stefan Institute, Jamova cesta 39, 1000, Ljubljana, Slovenia.
E-mail address: janez.zavasnik@ijs.si (J. Zavašnik).

https://doi.org/10.1016/j.jnucmat.2019.06.030
0022-3115/

particle and neutron loads [2]. Tungsten (W) is a candidate material for the divertor part of the demonstration fusion reactor (DEMO) [3]. As tungsten is relatively poorly resistant to oxidation at elevated temperatures, the sintering is carried out in a protective gas atmosphere or in vacuum conditions [4]. Different powder-metallurgy processes can be used to produce high-density tungsten. However, high temperatures and protracted sintering times are required because of tungsten's high melting point. A field-assisted sintering technique (FAST) was proposed to improve the sintering process for tungsten and to minimise the grain growth during the sintering. FAST processing takes place under vacuum or in an inert atmosphere (i.e., nitrogen or argon) while an electrical current is applied through the starting powder to generate heat, simultaneously with the application of uni-axial pressure. Using FAST we can achieve very high heating rates, leading to an order-of-magnitude-shorter sintering cycle compared to conventional sintering. It has been reported that high-density tungsten products are achievable at a relatively low sintering temperature when they are processed using FAST [5,6]. The FAST sintering of tungsten also has some drawbacks, such as direct carbon contamination from the FAST graphite tooling setup [4,6] and the *in-situ* formation of a secondary oxides, i.e., WO_2, due to the oxygen originating either from the raw powders or introduced during metal processing [7,8].

Interstitial elements play an important role in the technology of refractory metals such as tungsten, since they can have a strong effect on the low-temperature strength and the brittleness. At elevated temperatures, the presence of interstitial elements such as oxygen leads to the formation of secondary phases at the tungsten grain boundaries and consequently to embrittlement [9]. Moreover, the materials for fusion reactor that will be used as plasma-facing components (PFCs) require high-temperature stability (>2000 °C [3]), such as W, which is stable up to 3422 °C [10]. The presence of less-temperature-stable phase, such as WO_2 (1530 °C) can decrease the required performance of PFCs for fusion application. Oxide impurities could be removed by using a suitable additive, in order to achieve a cleaner grain boundary. To restrict the formation of any tungsten-oxide-rich phase at elevated temperatures, a direct carburization process using carbon or carbon-containing compounds can be used. The carbon balance is difficult to control and in most cases the reduction is either incomplete or the metal powder contains carbides [10]. Nevertheless, the formation of carbides in a tungsten matrix can have a positive influence on the properties of such a composite for fusion applications. For instance, the use of dispersed carbides (TaC, TiC and W_2C) that are distributed at the grain boundary or in the grain itself can restrict the tungsten-matrix grain growth and dislocation motion, both of which lead to improved high-temperature strength and creep resistance [11–13]. More recently, it was found that a tungsten carbide (WC) additive plays a crucial role in the densification of tungsten composites [14]. Based on these findings, the aim of our study was to explore and clarify the role of WC while removing oxide impurities from the tungsten matrix.

2. Experimental

To assess the ability of WC to bind oxygen during composite synthesis, tungsten and WC powders in different ratios were homogenised and heated with the simultaneous application of uni-axial pressure. The initial powder mixtures of W and WC (W−0.05 wt% C, W−0.25 wt% C, and W−0.51 wt% C), were calculated by stoichiometry (Table 1) based on our estimations of the free oxygen in the starting powders. The starting materials were commercially available pure tungsten powder (99.9% purity and particle size ≤ 1.5 μm, Global Tungsten & Powder) and submicron particles of WC (99% purity and a particle size in the range 0.15−0.2 μm, Sigma-Aldrich). The impurity contents of both used powders are listed in the supplementary data. The mixtures of WC and tungsten powders were homogenised in cyclohexane using an ultrasonic processor (UP400S, Hielscher Ultrasonic) operating at 24 kHz for 3 min at 50% amplitude. To preserve the obtained homogeneity after mixing, the suspension was freeze dried using liquid nitrogen. Prior to the sintering the cyclohexane was removed from the mixture by sublimation under reduced pressure.

For the consolidation of the powders, field-assisted sintering technology (FAST, model Dr SINTER SPS SYNTEX 3000, Fuji Electronic Industrial) was used. The powder mixtures were loaded into a graphite die with an inner diameter of 16 mm. Graphite foil was used to prevent die wear from any chemical reaction with the tungsten-based powder. Prior to sintering, the FAST chamber was purged with N_2 (99.996 % pure) and then evacuated (0.3−0.5 mbar). The sintering process was carried out under vacuum conditions. The samples were heated to 1900 °C at a heating rate of 100 °C/min, with a holding time of 5 min and a uniaxial pressure of 60 MPa.

The crystal phases of the products after the FAST consolidation were identified by X-ray diffraction (XRD, AXS D4 Endeavor, Bruker AXS), using Cu−Kα radiation at room temperature with a diffraction angle of $2\theta = 20–80°$, a step of 0.02° and an acquisition time of 1.0 s/step. As already reported in our previous experiments, the reaction of the sample with the graphite liner during sintering was observed on the surface of the sintered products [7]. To remove these artefacts, the surface reaction layer was ground off before any further analyses.

As a consequence of the expected binary-phase composition of the product, the bimodal size distribution of the grains and due to the well-known challenges of W_2C phase determination using X-ray diffraction [15–17], electron crystallography was additionally employed for an accurate phase determination. The electron diffraction was performed in a 200 kV transmission electron microscope (TEM, JEM-2100, Jeol). The crystal structures of the phases were calculated from selected-area electron-diffraction patterns (SAEDPs), and these data were used in the subsequent analyses and microstructure optimizations. The samples for the TEM analyses were prepared using a combined mechanical (Disc grinder Mod. 623 and Dimple Grinder Mod. 656, Gatan) and Ar-ion thinning process (PIPS 691, Gatan).

The morphology of the fractured samples was studied using a scanning electron microscope (SEM, JSM-7600F, Jeol) operating at 15 kV. For the observations of the samples' surfaces we used an Everhart-Thornley-type detector for low-energy (<50 eV) secondary electrons (SEs), generated by inelastic scattering interactions with the primary electrons. Due to their low energy, the SEs

Table 1
Stoichiometry of the prepared W-WC powder mixtures, expected carbon content, and calculated expected composition after FAST consolidation.

	Sample "name"		
	W−0.05 W C	W−0.25 W C	W−0.51 W C
Carbon content (wt %) in the starting mixture	0.05	0.25	0.51
Carbon content (at %) in the starting mixture	0.70	3.70	7.30
Volume fraction of WC in the mixture (vol %)	W-1.1 vol % WC	W-4.9 vol % WC	W-9.9 vol % WC
Volume fraction of W_2C in the composite after sintering (vol %)	W-1.9 vol % W_2C	W-8.4 vol % W_2C	W-17.7 vol % W_2C

originate only from a depth of a few nm below the sample surface.

The chemical compositions of the secondary phases were studied by SEM (Zeiss Auriga Crossbeam, Carl Zeiss Microscopy), employing energy-dispersive X-ray spectroscopy (EDXS; Octane Elect, EDAX AMETEK). The compositions of the phases and their spatial distributions were assessed by electron-backscatter diffraction (EBSD; TEAM EBSD, Hikari Super, OIM Analysis software, EDAX AMETEK). Both types of experiments were conducted at an accelerating voltage of 20 kV. During the image post-processing, data with a confidence index lower than 0.1 were omitted. The samples were prepared according to standard metallographic procedures by cutting, grinding and polishing. For the EBSD analyses, the samples were sequentially polished with 1-μm diamond paste, and for the final polishing a 5 vol % H_2O_2 solution of colloidal silica was applied.

The thermal decomposition of the tungsten-based mixtures was studied by differential thermal analyses (DTA) and thermo-gravimetric analyses (TGA) (Netzsch Jupiter 449 simultaneous thermal analysis instrument coupled with Netzsch QMS 403C Aëolos quadrupole mass spectrometer (MS)). Prior to the analysis, the chamber was thoroughly purged with high-purity argon (99.999 at %) and finally evacuated to 0.01 mbar. The analysis was performed using an Al_2O_3 crucible with a lid under a protective Ar atmosphere, in the temperature range 25 °C–1400 °C. The temperature was ramped at heating and cooling rates of 25 °C/min.

3. Results and discussion

The XRD diffractograms of the initial powders correspond to pure tungsten with a body-centred cubic (bcc) structure (a = 3.165 Å, Im-3m, SG: 229) and pure WC with a hexagonal structure (a = b = 2.906 Å, c = 2.837 Å, P-6m2, SG: 187) (Fig. 1).

For the consolidated samples with the initial compositions W–0.05 W C, W–0.25 W C and W–0.51 W C we calculated an overall carbon content of 0.7 at %, 3.7 at %, and 7.3 at %, respectively (Table 1). From the W-C phase diagram [20] the samples with such carbon contents would be within the W + WC two-phase region at room temperature and in the W + W_2C two-phase region after sintering at a temperature higher than 1250 °C, following the reaction [14]:

$$aW + bWC \rightarrow (a{-}b)W + bW_2C \tag{1}$$

After the FAST consolidation, the phases formed in the bulk samples were identified. The X-ray diffraction results of the consolidated bulk samples (Fig. 2a) reveal strong reflections of the bcc tungsten. Surprisingly, in the sintered samples W–0.05 W C and W–0.25 W C only bcc tungsten was detected. This implies that the amount of second phase is below the detection limit of the laboratory XRD instrument (approx. 2 wt % [17]). In the sintered samples with the highest carbon content (W–0.51 W C), both phases, tungsten and W_2C (ICSD #167900 [21]), could be detected.

An investigation of the morphology of the fracture surfaces of the sintered samples revealed different fracture modes: inter-granular and trans-granular fracture were observed on the fracture surface (Fig. 2c and d), while only inter-granular fracture was observed in the sample W–0.05 W C (Fig. 2b). A close inspection of the fractured composites revealed tungsten matrix grains and a secondary phase located at the tungsten grain boundaries (Insets in Fig. 2b, c and d). Using semi-quantitative EDXS mapping (Fig. 3), this secondary phase in the W–0.05 W C and W–0.25 W C was identified as an oxygen-rich tungsten compound.

In the sample W–0.51 W C, where W_2C was detected (Fig. 2a), the morphology and crystal structure of this secondary phase were further investigated by TEM. The TEM was performed on particles located within the grains and on those at the grain boundaries. Bright-field (BF) TEM images of the W–0.51 W C composite are presented in Fig. 4. Large tungsten grains containing single-crystal spherical grains, approximately 200 nm in diameter (Fig. 4a and b), were resolved and identified by SAEDP as W_2C (insert in Fig. 4a and b). The SAEDP along the [0001] and [01–10] zone axes, with the further illustrated atomic structure models in [0001] and [01–10] (Fig. 4c), from the intra-granular W_2C grains, were further indexed as a primitive trigonal/rhombohedral crystal system (lattice parameter: a, b = 5.1 ± 0.5 Å and c = 4.7 ± 0.5 Å; SG: P-31 m [21]), also known as ε-W_2C with the ε-Fe_2N structure.

In accordance with the crystal-structure determination, W_2C databases were prepared for electron-backscatter-diffraction (EBSD) analyses, making it possible to resolve this phase on a larger scale. Since the differentiation of the phases is based on two different crystallographic structures, i.e., cubic tungsten and trigonal W_2C, the resulting phase map represents the spatial distribution of the W_2C in the tungsten matrix (Fig. 4c). ε-W_2C does not undergo a solid-phase decomposition at 1250 °C and is stable at room temperature, which was also observed after different sintering processes [14,20,22].

In accordance with the data obtained from the different phase and chemical analyses, it is clear that there is a deficit of W_2C phase in the tungsten-based composites studied in this research (Table 1). The presence of an oxygen-rich tungsten compound after sintering suggests that oxidation occurs during the consolidation with FAST. A previous study of the surface-oxidation behaviour of tungsten

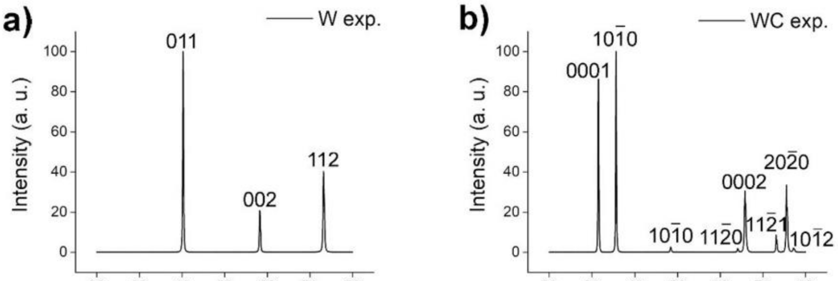

Fig. 1. Experimental X-ray diffractograms of the (a) starting W (W exp.) and (b) WC powders (WC exp.). The diffracted planes of the W (ICSD #167904) [18] and WC (ICSD #5212) [19] are shown above the corresponding peaks.

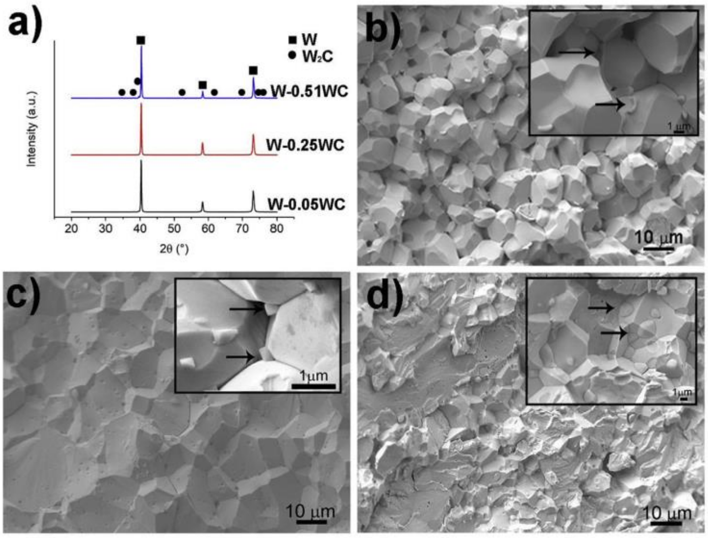

Fig. 2. (a) XRD patterns of W composites with different contents of WC. FE-SEM images of the fractured surface of (b) W−0.05 W C, (c) W−0.25W and (d) W−0.51W samples. The secondary phase is marked with arrows.

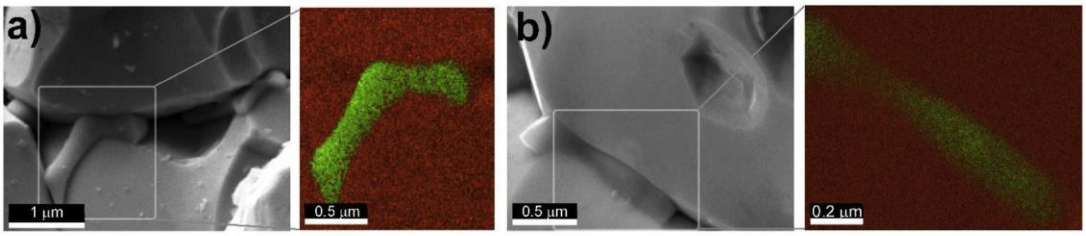

Fig. 3. Secondary oxide phase adjoining the W grains (SEM, SE), with the corresponding EDXS mapping for O (green) and W (red) (a) W−0.05 W C sample and (b) W−0.25 W C sample.

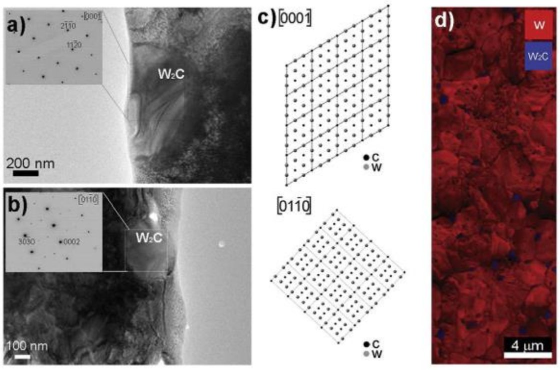

Fig. 4. TEM-BF micrographs of the W sample, containing W_2C grains embedded in W grains (a, b); inset shows: (a) [0001] and (b) [01−10] zone axis SAEDP of W_2C, (c) with the corresponding structure model in the same orientation. (d) SEM-EBSD phase-map composition with IQ maps of W (red) and W_2C (blue), constructed from crystallographic data, obtained by TEM-SAEDP, presenting the spatial distribution of W_2C grains in the W matrix. (For interpretation of the references to colour in this figure legend, the reader is referred to the Web version of this article)

demonstrated that a WO_2 oxide layer grows on the tungsten surface when annealed between 727 and 1327 °C, even in an environment with a low oxygen pressure of 8×10^{-6} mbar, indicating that tungsten has a relatively poor oxidation resistance at elevated temperatures [23]. Furthermore, we previously reported that oxygen impurities in the feedstock powder could also contribute to the formation of WO_2 [7]. This is attributed to the non-equilibrium conditions during the short sintering time in FAST [8]. The thermodynamically preferred reaction that can occur during the FAST consolidation of the tungsten and WC powders is the formation of WO_2:

$$W + O_2 = WO_2 \tag{2}$$

The calculation of the standard Gibbs free energy (ΔG°) for WO_2 formation from thermodynamic data (ΔH°, ΔS°) gave the following relationship: $\Delta G^\circ = -589.7 + 0.1873T$ $KJmol^{-1}$. Based on the negative ΔG°, this reaction is thermodynamically feasible and the experiments confirmed that it is also kinetically possible [7].

When a surplus of carbon-rich additive was used (W−0.51 W C), the oxygen-rich tungsten phase disappeared, which can be attributed to the reducing effect of the WC. The use of graphite dies additionally ensures a reducing environment in the FAST chamber during the sintering process. To clarify these phenomena, thermo-analytical techniques were employed to determine the thermal effects, evolved gases and quantify the mass loss during heating in the powder mixture W–0.51 W C, for which no oxide phase was observed. Moreover, the possible reactions were considered in terms of the thermodynamics.

For the powder mixture W–0.51 W C the thermo-gravimetric (TGA) curve (Fig. 5a) revealed several regions of weight changes. As confirmed by the mass spectrometry (MS) the first region from 25 to 350 °C with a mass loss of 0.06 % corresponds to the removal of the adsorbed water molecules from the surface of the powder mixture (Fig. 5b). In the temperature range 350–780 °C, we observed a weight gain of 0.1 %, which is associated with the surface oxidation. The subsequent two steps with a total mass loss of 1.08 % were observed from 800 to 1250 °C. The MS revealed that both CO ($m/z = 28$) and CO_2 ($m/z = 44$) evolved in this temperature range. It is known that the fragment peak at $m/z = 28$ could belong to CO_2 and CO. Based on the difference in the peak shape and the higher intensity of the peak for $m/z = 28$ than for $m/z = 44$, the major contribution to the intensity of the $m/z = 28$ peak came from the CO and not from the CO_2. Namely, for the CO_2 the fragment $m/z = 28$ exhibits a lower intensity than the fragment $m/z = 44$.

In the mixture of W-xWC, WC as a source of carbon will act as a reducing agent during sintering [24]. The tungsten oxide (metal oxide; MeO_2) is expected to be removed chemically by its reaction with WC, similar to that already reported for the reaction of WC with other MeO_2 (Me-metal); $3WC + MeO_2 \rightarrow MeC + 3W + 2CO$ [25].

For the reaction of WC with WO_2, the following two reactions are proposed:

$$2WC + WO_2 \rightarrow 3W + 2CO \tag{3}$$

$$WC + WO_2 \rightarrow 2W + CO_2 \tag{4}$$

Thermodynamic considerations of both reactions revealed $\Delta G^\circ = 449.7–0.378T$ kJ mol^{-1} and $\Delta G^\circ = 236.7–0.1971T$ kJ mol^{-1} for reactions 3 and 4, respectively. Reaction 3, in which CO is evolved, becomes thermodynamically feasible at $T \geq 916$ °C, while the evolution of CO_2 through reaction 4 is possible at $T \geq 928$ °C. The slightly more negative ΔG° of reaction 3 ($\Delta G^\circ = -70$ kJ mol^{-1}) compared to that of reaction 4 ($\Delta G^\circ = -33$ kJ mol^{-1}) at 1100 °C, where the reaction rate of both processes reached the maximum, implied that reaction 3 prevailed over reaction 4. This is also qualitatively supported by the higher intensity of the peak for $m/z = 28$ than for $m/z = 44$. The endothermic process suggested by the above thermodynamic equations for both reactions was confirmed by the endothermic peak in the DTA curve. The formation of CO_2 is possible through the combustion of C (graphite dies) or WC.

$$C + O_2 \rightarrow CO_2 \tag{5}$$

$$½WC + O_2 \rightarrow ½WO_2 + ½CO_2 \tag{6}$$

Thermodynamic analyses showed $\Delta G^\circ = -393.7–0.00306$ T kJ mol^{-1} and $\Delta G^\circ = -472.35–0.089$ T kJ mol^{-1} for the reactions 5 and 6, respectively. Both reactions are exothermic, which is not in accordance with the DTA results (Fig. 5a), implying that these two reactions were not dominant, although they are thermodynamically feasible ($\Delta G^\circ < 0$).

By merging the proposed reactions with the data obtained from the mass spectrometry of the sample W–0.51 W C, at least 5.8 vol % WC (reaction 3) to 8.8 vol % WC (reaction 4) must be introduced into the starting mixture to completely remove the oxygen impurities in the form of CO_x and to obtain pure tungsten.

During the FAST consolidation of tungsten powder at elevated temperature, the *in-situ* formation of an oxide-rich tungsten phase was observed, as also reported by other researchers [7–9]. The degradation of tungsten-based composites containing an oxide-rich tungsten phase at elevated temperature may influence the performance of such material when used as a plasma-facing material for fusion applications [7]. For the future designing of plasma-facing material, we need to mitigate the influence of small amounts of oxygen or completely remove it through a carburization reaction. During an accident in a fusion reactor, such as a failure of the cooling system, the nuclear decay heat can cause the materials to heat up significantly. If air enters the fusion-reactor chamber, tungsten will start to form highly volatile tungsten oxide compounds that, in the worst case, can even escape from the chamber [3]. The development of a self-passivating tungsten-based composite can improve the intrinsic safety of future fusion facilities. A previous study suggested that W_2C as a source of carbon can also remove other metal oxide species via the reaction $W_2C + MeO_2 \rightarrow MeC + 6W + 2CO$ [25]:

$$2W_2C + WO_2 \rightarrow 5W + 2CO \tag{7}$$

Based on $\Delta G^\circ = 431.3 + 0.504$ T kJ mol^{-1} the reaction $2W_2C + WO_2 \rightarrow 5W + 2CO$ is thermodynamically feasible at $T \geq 582$ °C.

Materials for fusion application face a multitude of interlinked challenges during their lifetime. Materials that will be in direct contact with the hot plasma environment inside the fusion reactor will be affected by high heat-loads, neutrons and by impacting ions [8]. For suitability of a tungsten/W_2C composite, we need further tests to estimate the materials lifetime after damage caused by plasma-material interactions. Nevertheless, the W_2C phase shows a higher temperature stability than WO_2 [10].

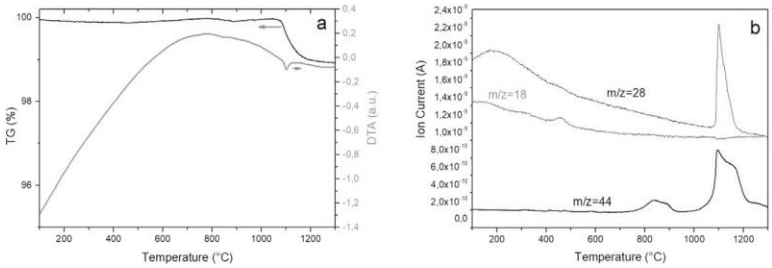

Fig. 5. Thermo-gravimetric (TGA) and differential thermal analysis (DTA) curves (a) and MS of evolved gases (b) for W–0.51 W C powder composition.

4. Conclusion

The *in-situ* formation of an oxide-rich tungsten phase in the tungsten matrix during high-temperature vacuum consolidation in FAST must be taken into account when considering fusion applications. In this work, trace amounts of oxide impurities were identified and removed through the use of carbon in the form of a WC deoxidation agent. Based on the calculation, at least 5.8–8.8 vol % WC must be introduced into the starting mixture to completely remove the oxygen impurities in the form of CO and CO_2 and to obtain pure tungsten. Surplus amount of WC will lead to the formation of a thermally stable W_2C as a second phase at 1900 °C.

Acknowledgements

This work has been carried out within the framework of the EUROfusion Consortium and has received funding from the Euratom research and training programme 2014–2018 and 2019–2020 under grant agreement No 633053. The views and opinions expressed herein do not necessarily reflect those of the European Commission. The authors acknowledge financial support of Slovenian Research Agency, project J2-8165: "W- and WC-based composites for high thermally loaded parts in the fusion demonstration power plant DEMO" and bilateral project between the Slovenian Research Agency and Deutscher Akademischer Austauschdienst, BI-DE/57450885 and BI-DE/19-20-002: "Investigation of helium retention in plasma facing materials using advanced analytical methods".

Appendix A. Supplementary data

Supplementary data to this article can be found online at https://doi.org/10.1016/j.jnucmat.2019.06.030.

Data availability

The raw and processed data required to reproduce these findings are available from the corresponding author upon reasonable request.

References

[1] D. Maisonnier, D. Campbell, I. Cook, L. Di Pace, L. Giancarli, J. Hayward, A. Li Puma, M. Medrano, P. Norajitra, P. Sardain, M.Q. Tran, D. Ward, Power plant conceptual studies in Europe, Nucl. Fusion 47 (11) (2007) 1524–1532.

[2] G. Pintsuk, in: R.J.M. Konings (Ed.), Tungsten as a Plasma-Facing Material. Comprehensive Nuclear Materials, vol. 4, Elsevier, Amsterdam, 2012, pp. 551–581. https://doi.org/10.1016/B978-0-08-056033-5.00118-X.

[3] J.W. Coenen, S. Antusch, M. Aumann, W. Biel, J. Du, J. Engels, S. Heuer, A. Houben, T. Hoeschen, B. Jasper, F. Koch, J. Linke, A. Litnovsky, Y. Mao, R. Neu, G. Pintsuk, J. Riesch, M. Rasinski, J. Reiser, M. Rieth, A. Terra, B. Unterberg, Th. Weber, T. Wegener, J.-H. You, Ch. Linsmeier, Materials for DEMO and reactor applications—boundary conditions and new concepts, Phys. Scripta (2016), 014002. https://doi.org/10.1088/0031-8949/2016/T167/014002.

[4] Z.Z. Fang, Sintering of Advanced Materials - Fundamentals and Processes, Woodhead Publishing, Cambridge, UK, 2010.

[5] J. Choi, H.-M. Sung, K.-B. Roh, S.-H. Hong, G.-H. Kum, H.-N. Han, Fabrication of sintered tungsten by spark plasma sintering and investigation of thermal stability, Int. J. Refract. Met. H 69 (2017) 164–169. https://doi.org/10.1016/j.ijrmhm.2017.08.013.

[6] G. Lee, J. McKitrick, E. Ivanov, E.A. Olevsky, Densification mechanism and mechanical properties of tungsten powder consolidated by spark plasma sintering, Int. J. Refract. Met. H. 61 (2016) 22–29. https://doi.org/10.1016/j.ijrmhm.

[7] A. Šestan, P. Jenuš, S.K. Novak, J. Zavašnik, M. Čeh, The role of tungsten phases formation during tungsten metal powder consolidation by FAST: implications for high-temperature applications, Mater. Char. 138 (2018) 308–314. https://doi.org/10.1016/j.matchar.2018.02.022.

[8] L. Huang, L. Jiang, T.D. Topping, C. Dai, X. Wang, R. Carpenter, C. Haines, J.M. Schoenung, In situ oxide dispersion strengthened tungsten alloys with high compressive strength and high strain-to-failure, Acta Mater. 122 (2017) 19–31. https://doi.org/10.1016/j.actamat.2016.09.034.

[9] J.R. Stephens, Effects of interstitial impurities on the low-temperature tensile properties of tungsten, in: NASA Technical Note D-2287, 1964 (Washington, D. C).

[10] E. Lassner, W.-D. Schubert, Tungsten: Properties, Chemistry, Technology of the Element, Alloys, and Chemical Compounds, Springer US, New York, 1999.

[11] X.-Y. Tan, L.-M. Luo, Z.-L. Lu, G.-N. Luo, X. Zan, J.-G. Cheng, Y.-C. Wu, Development of tungsten as plasma-facing materials by doping tantalum carbide nanoparticles, Powder Technol. 269 (2015) 437–442. https://doi.org/10.1016/j.powtec.2014.09.039.

[12] G.M. Song, Y. Zhou, Y.J. Wang, The microstructure and elevated temperature strength of tungsten-titanium carbide composite, J. Mater. Sci. 37 (16) (2002) 3541–3548. https://doi.org/10.1023/A:1016583611632.

[13] P. Jenuš, A. Iveković, M. Kocen, A. Šestan, S. Novak, W_2C-reinforced tungsten prepared using different precursors, Ceram. Int. 45 (6) (2019) 7995–7999. https://doi.org/10.1016/j.ceramint.2018.11.187.

[14] S. Chanthapan, A. Kuklkarni, J. Singh, C. Hains, D. Kapoor, Sintering of tungsten powder with and without tungsten carbide additive by field assisted sintering technology, Int. J. Refract. Met. H. 31 (2012) 114–120. https://doi.org/10.1016/j.ijrmhm.2011.09.014.

[15] T. Epicier, J. Dubois, C. Esnouf, G. Fantozzi, P. Convert, Neutron powder diffraction studies of transition metal hemicarbides M2C1-x—II. In situ high temperature study on W2C1-x and Mo2C1-x, Acta Metall. 36 (8) (1988) 1903–1921. https://doi.org/10.1016/0001-6160(88)90293-3.

[16] A.S. Kurlov, A.I. Gusev, Neutron and x-ray diffraction study and symmetry analysis of phase transformations in lower tungsten carbide W2C, Phys. Rev. B 76 (17) (2007), 174115. https://doi.org/10.1103/PhysRevB.76.174115.

[17] D.L. Bish, J.E. Post, Modern Powder Diffraction, Mineralogical Society of America, 1989.

[18] A. Friedrich, B. Winkler, L. Bayarjargal, A. Juarez, A. Erick, W. Morgenroth, J. Biehler, F. Schroeder, J. Yan, S.M. Clark, In situ observation of the reaction of tantalum with nitrogen in a laser-heated diamond anvil cell, J. Alloy. Comp. 502 (1) (2010) 5–12. https://doi.org/10.1016/j.jallcom.2010.04.113.

[19] Q. Fang, W. Bai, J. Yang, X. Xu, G. Li, N. Shi, M. Xiong, H. Rong Qusongite (WC), A new mineral, Am. Mineral. 94 (2–3) (2009) 387–390. https://doi.org/10.2138/am.2009.3015.

[20] A.S. Gusev, A.I. Gusev, Tungsten carbides: structure, properties and application in hardmetals, in: C.J.R. Hull, R.M. Osgood, J. Parisi, Z.M. Wang (Eds.), Springer Series in Materials Science, vol.184, Springer International Publishing, 2013.

[21] Y.-F. Li, Y.-M. Gao, B. Xiao, T. Min, Z.-J. Fan, S.-Q. Ma, L.-L. Xu, Theoretical study on the stability, elasticity, hardness and electronic structures of W-C binary compounds, J. Alloy. Comp. 502 (2010) 28–37. https://doi.org/10.1016/j.jallcom.2010.04.184.

[22] T. Li, Q. Li, J.Y.H. Fuh, P.C. Yu, C.C. Wu, Effects of lower cobalt binder concentrations in sintering of tungsten carbide, Mater. Sci. Eng. A 430 (1) (2006) 113–119. https://doi.org/10.1016/j.msea.2006.05.118.

[23] K. Radican, I.S. Bozhko, S.-R. Vadapoo, S. Ulucan, H.-C. Wu, A. McCoy, I.V. Shvets, Oxidation of W(110) studied by LEED and STM, Surf. Sci. 604 (19) (2010) 1548–1551. https://doi.org/10.1016/j.susc.2010.05.016.

[24] J. Zou, H.-B. Ma, A. D'Angio, G.-J. Zang, Tungsten carbide: a versatile additive to get trace alkaline-earth oxide impurities out of ZrB2 based ceramics, Scripta Mater. 147 (2018) 40–44. https://doi.org/10.1016/j.scriptamat.2017.12.033.

[25] G.-J. Zhang, H.-T. Liu, W.-W. Wu, J. Zou, D.-W. Ni, W.-M. Guo, J.-X. Liu, X.-G. Wang, Reactive processes for diboride-based ultra-high temperature ceramics, in: W.G. Fahrenholtz, E.J. Wuchina, W.E. Lee, Y. Zhou (Eds.), Ultra-High Temperature Ceramics: Materials for Extreme Environment Applications, Wiley, 2014.

Supplementary data

Tungsten carbide as a deoxidation agent for plasma-facing tungsten-based materials

Andreja Šestan [a, b, c], Janez Zavašnik [c, d,f,*], Marjeta Maček Kržmanc [e], Matej Kocen [b, f], Petra Jenuš [f], Saša Novak [f], Miran Čeh [a, b, f], Gerhard Dehm [c]

[a] Centre for Electron Microscopy and Microanalysis, Jožef Stefan Institute, 1000 Ljubljana, Slovenia
[b] Jožef Stefan International Postgraduate School, 1000 Ljubljana, Slovenia
[c] Max-Planck-Institut für Eisenforschung GmbH, 40237 Düsseldorf, Germany
[d] Gaseous Electronics, Jožef Stefan Institute, 1000 Ljubljana, Slovenia
[e] Advanced Materials Department, Jožef Stefan Institute, 1000 Ljubljana, Slovenia
[f] Department for Nanostructured Materials, Jožef Stefan Institute, 1000 Ljubljana, Slovenia

1. Chemical composition of the starting powder provided by the manufacturer

Chemical composition of initial tungsten (Table 1) and tungsten carbide (Table 2) powder.

Table 1: Tungsten power (MPO7R; Global Tungsten & Powder, USA)

impurities	ppm
O	1050
Al	<10
Ca	1
Co	<1
Cr	2
Cu	1
Fe	2
K	2
Mg	<1
Mn	2
Mo	9
Na	2
Ni	3
Pb	<5
S	1

Table 2: Tungsten carbide power (Sigma-Aldrich, USA)

impurities	ppm
V	26
Al	60
Ca	1
Co	26
Cr	3885
Cu	0.5
Fe	29
K	1.1
Mg	4
Mn	3.3
Mo	0.5
Na	3.2
Ni	1.1
Pb	1.2
Ti	0.3
Zr	1.6

2. XRD patterns of W-0.51WC plotted in log-scale.

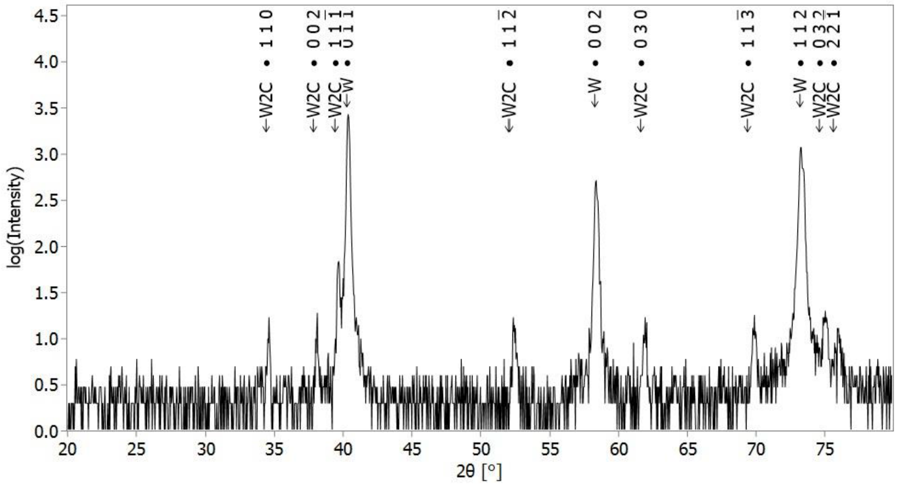

3. Corresponding diagrams for the chemical reaction that can occur during FAST

Thermodynamically preferred reactions between tungsten and oxygen during FAST consolidation are the formation of WO_2 (Fig. 1).

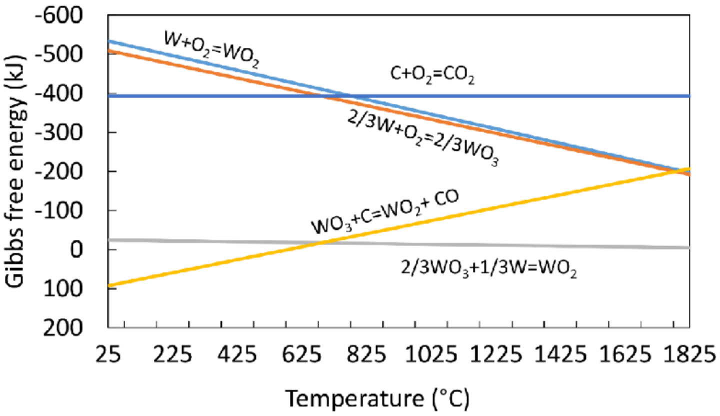

Figure 1: Diagram for the chemical reactions that can occur during FAST of tungsten powder.

Gibbs free energy of formation was calculated from the corresponding value for the entropy and enthalpy of formation at 298 K [1, 2].

$\Delta S° = \sum nS_f°{}_{\text{products}} - \sum mS_f°{}_{\text{reactants}}$

$\Delta H° = \sum nH_f°{}_{\text{products}} - \sum mH_f°{}_{\text{reactants}}$

$\Delta G° = \Delta H° - \Delta S°T$

4. Calculation of Gibbs free energy of formation for the reactions 3-7.

Gibbs free energy of formation for the reaction 3, 4, 5, 6 and 7, was calculated from the corresponding value for the entropy and enthalpy of formation at 298 K [1-6].

$\Delta S° = \sum nS_f°{}_{\text{products}} - \sum mS_f°{}_{\text{reactants}}$

$\Delta H° = \sum nH_f°{}_{\text{products}} - \sum mH_f°{}_{\text{reactants}}$

$\Delta G° = \Delta H° - \Delta S°T$

References:

1. W. M. Haynes, D. R. Lide and, T. J. Bruno, (2016). *CRC handbook of chemistry and physics: a ready-reference book of chemical and physical data.* 2016-2017, 97th Edition / Boca Raton, Florida: CRC Press.
2. R. J. L. Andon, J. F. Martin, K. C. Mills, and T. R. Jenkins, *Heat capacity and entropy of tungsten carbide.* The Journal of Chemical Thermodynamics, 1975. **7**(11): p. 1079-1084. https://doi.org. /10.1016/0021-9614(75)90241-4
3. D. K. Gupta and L. L. Seigle, *Free energies of formation of WC and W2C, and the thermodynamic properties of carbon in solid tungsten.* Metalurgical Transactions A- Physical Metallurgy and Materials Science, 1975. **6A**: p. 1939-1944.
4. G.-J. Zhang, H.-T. Liu, W.-W. Wu, J. Zou, D.-W. Ni, W.-M. Guo, J.-X. Liu, and X.-G. Wang, Reactive Processes for Diboride-Based Ultra-High Temperature Ceramics, in: W.G. Fahrenholtz, E. J. Wuchina, W. E. Lee, and Y. Zhou (Eds.), *Ultra-High Temperature Ceramics: Materials for Extreme Environment Applications*, Wiley, 2014.
5. H. Jehn, G. Bar, E. Best, and E. Koch, *W Tungsten: Supplement Volume A 5 b Metal, in:* J. v. Jouanne, E. Koch and E. Koch (Eds), *Chemical Reactions with Nonmetals Nitrogen to Arsenic, Gmelin Handbook of Inorganic and Organometallic Chemistry - 8th edition, W. Wolfram. Tungsten (System-Nr. 54)*, Springer Science & Business Media, 2013.
6. L. D. McGraw, H. Seltz, and P. E. Snyder, T*he Heat of Combustion of Tungsten Carbide, WC1.* J. Am. Chem. Soc. 1947. **69**(2): p. 329–331. https://doi.org. /10.1021/ja01194a050

4.3 Non-Uniform He Bubble Formation in W/W_2C Composite: Experimental and Ab-Initio Study

This work shows the influence of energetic $^4He^+$ ions implanted in the W/W_2C composite, which was investigated and optimized through previous publications. More on this topic is provided in the article entitled *"Non-uniform He bubble formation in W/W_2C composite: Experimental and ab-initio study"*, authored by A. Šestan, L. Sreekala, S. Markelj, M. Kelemen, J. Zavašnik, C. H. Liebscher, G. Dehm, T. Hickel, M. Čeh, S. Novak, and P. Jenuš, and published in the scientific journal *Acta Materialia* [74].

Currently, there is no available operational fusion reactor for irradiation of laboratory-scale materials in the prototype stage. On the other hand, it is already well established that He-implantation by linear accelerator can be utilised to a certain extent to mimic conditions in the fusion reactor during operation. The tungsten-tungsten carbide (W/W_2C) composites are currently considered possible candidates for the plasma-facing materials in future fusion reactors. To clarify the material behaviour under He irradiation, we investigated the microstructure evolution of polycrystalline W − W_2C composite consolidated by FAST. The sample was implanted at room temperature by 1 MeV $^4He^+$ at the fluence of 8×10^{16} ions cm^{-2}. After implantation, the sample was additionally annealed at 1873 K for 20 minutes to induce coalescence of implanted He and the formation of nano-scale bubbles. Due to the small size of the features, the sample was analysed by scanning and conventional TEM. We found that in tungsten grains, the monomodal He bubbles in size of 30-80 nm are mainly associated with point defects. A 150 nm thick void denuded zone was observed at the grain boundaries. In the W_2C grains, the bubbles do not form. Instead, we observed considerably larger He voids at the phase interface between tungsten grains and tungsten carbide. The formation of He bubbles in W grains can be explained as He-He self-trapping effect, which will result in decohesion in W grains, e.g., bubbles. The incapability of helium clusters to form a free surface can explain the absence of helium induced-defects in W_2C.

The observed features were complemented by the computational quantum mechanical modelling method (Density-functional theory) to achieve a fundamental understanding of helium behaviour and migration in W and W_2C. By coupling the experimental data with computational predictions, we made a significant step forward in assessing the material resistivity under plasma surface interaction.

In the scope of the research article, my contribution was: I designed the research and experiments, prepared the samples for SEM analysis, collected and interpreted diffraction data from SAED, and performed crystallography analysis of the phases by SEM-EBSD and interpreted the data. I calculated and interpreted the data for the simulations of electron penetration into W and W_2C and performed optical microscopy and SEM-FIB investigation of the irradiated and pristine samples. I wrote a manuscript draft, coordinated the input with co-authors, wrote the final manuscript and submitted, revised, and published the research. A copy of the article and the article's s supplementary information are presented on the following pages.

Acta Materialia 226 (2022) 117608

Contents lists available at ScienceDirect

Acta Materialia

journal homepage: www.elsevier.com/locate/actamat

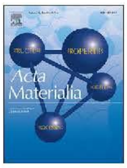

Non-uniform He bubble formation in W/W_2C composite: Experimental and *ab-initio* study

Andreja Šestan[a,b,*], Lekshmi Sreekala[b], Sabina Markelj[a], Mitja Kelemen[a], Janez Zavašnik[a,b], Christian H. Liebscher[b], Gerhard Dehm[b], Tilmann Hickel[b,d], Miran Čeh[a,c], Saša Novak[a,c], Petra Jenuš[a]

[a] *Jožef Stefan Institute, Jamova c. 39, 1000 Ljubljana, Slovenia*
[b] *Max-Planck-Institut für Eisenforschung, Max-Planck-Straße 1, 40237, Düsseldorf, Germany*
[c] *Jožef Stefan International Postgraduate School, Jamova c. 39, 1000, Ljubljana, Slovenia*
[d] *Federal Institute for Materials Research and Testing (BAM), Richard-Willstätter-Straße 11, 12489, Berlin, Germany*

ARTICLE INFO

Article history:
Received 22 September 2021
Revised 4 December 2021
Accepted 28 December 2021
Available online 6 January 2022

Keywords:
tungsten
ditungsten carbide
FAST
helium implantation
density functional theory

ABSTRACT

Tungsten-tungsten carbide (W/W_2C) composites are considered as possible structural materials for future nuclear fusion reactors. Here, we report on the effect of helium (He) implantation on microstructure evolution of polycrystalline W/W_2C composite consolidated by field-assisted sintering technique (FAST), homogenously implanted at room temperature with 1 MeV $^4He^+$ ions at the fluence of 8×10^{16} ions cm^{-2} and annealed at 1873 K for 20 minutes. Samples were analysed by scanning and transmission electron microscopy to study the presence and size of He bubbles. Monomodal He bubbles in W (30-80 nm) are limited to point defects and grain boundaries, with a considerable void denuded zone (150 nm). Bubbles do not form in W_2C, but at the W|W_2C interface and are considerably larger (200-400 nm). The experimental observations on He behaviour and migration in W and W_2C were assessed by density functional theory (DFT) calculations, suggesting He migration and accumulation in the composite are determined by the effective He-He binding in clusters, which will give rise to decohesion. In the presence of He clusters, the decohesion of bulk W into free surfaces is energetically highly favourable but not sufficient in the W_2C; hence bubbles are only observed in W grains and interfaces and not within bulk W_2C.

1. Introduction

Materials considered for nuclear reactor environments must perform under extreme conditions, including simultaneous radiation damage, elevated temperature, and mechanical stress. Helium (He) is the by-product generated in fission [1] and fusion [2] reactions. Due to the extremely low solubility in most materials, He tends to coalesce to form gas stabilised voids or cavities (bubbles), significantly degrading the physical properties of the materials [3]; therefore, characterisation of the He behaviour in solids is one of the steps to predict the material performance under irradiation. Helium-ion implantation is the prevailing technique to mimic nuclear-reaction induced radiation damage of materials by creating radiation-damage-like lattice defects, allowing examination of the interaction of the injected He with structure imperfections [4–6]. Post-implantation microstructural analysis by transmission electron microscopy (TEM) of cavity density, size, and spatial distributions is used for determining the physical origins of mechanical property degradation. Up to now, helium-implanted tungsten (W) has been experimentally and theoretically probed for varying conditions of temperature and He fluence [7,8]. On the other hand, He implantation effects on W_2C and multi-phase, polycrystalline W-based composites are generally unknown.

In a deuterium-tritium fusion reaction, plasma-facing materials (PFMs) must withstand high energy neutron bombardment and hydrogen isotope ion (plasma) exposure, combined by high thermal flux and continuous production of He through (n, p) and (n, α) nuclear reactions in PFMs. The contribution of He produced from neutron-induced reaction depends very much on the choice of the PFMs [9]. Metallic tungsten (W) and its carbides are some of the candidates proposed as fusion-relevant materials because of their high melting point, high thermal conductivity, low physical sputtering yield and low hydrogen isotope retention [10,11]. After five full-power years of neutron irradiation of W, we can expect to get 30 atomic parts per million (appm) He through neutron capture and α particle emission (n,α) [9], with an additional 600 appm due to tritium decay with the assumption of 1 at.% tritium retention

---

[*] Corresponding author.
E-mail address: andreja.sestan@ijs.si (A. Šestan).

https://doi.org/10.1016/j.actamat.2021.117608
1359-6454/

[12]. As also transmutation of carbon under neutron irradiation results in He production [9], the carbon present in bulk might even further increase the predicted He concentration in the material. Helium will influence the macroscopic properties of the material, such as tensile strength, creep and fatigue behaviour or swelling [13,14], while emitted α-particles, having energies of the order of MeV, will cause displacement damage in the crystal lattice [9,15]. At elevated irradiation temperature, rapid He accumulation along the grain boundaries and dislocations will promote inter-granular fracture known as helium embrittlement, leading to pronounced surface blistering and exfoliation [15,16]. Additionally, sintered W is characterised by high porosity and low recrystallization temperature. To address this issue, the incorporation of transition-metal ceramic particles (TiC, TaC and W$_2$C) into the W matrix was suggested to suppress recrystallization and consequent grain growth at high temperatures [17–21].

The primary objective of the present research was to provide experimental insight into the behaviour of W/W$_2$C composite under helium implantation and its effect on the microstructure of the multi-phase material, micrometres below the surface. The sample consolidated by field-assisted sintering technique (FAST) was He-implanted at room temperature (RT) and subsequently annealed at 1873K for 20 min to mimic the short temperature excursions above 1500K that can be expected in high heat loads and particle flux areas in the fusion reactor [22]. The microstructure features of the He-irradiated samples were examined by scanning electron microscopy (SEM), while transmission electron microscopy (TEM) was used to assert the He-implantation-induced defects. The experimental observations of He bubble formation in the W/W$_2$C composite were complemented by first-principles based density functional theory (DFT) calculations to establish a fundamental understanding of He clustering, migration and dissolution in W and W$_2$C.

2. Materials and methods

2.1. Starting materials

The W/W$_2$C composite was densified by FAST under moderate vacuum (30 – 50 Pa), as described in detail in [21]. The starting materials were commercially available pure tungsten powder (99.9 % purity with particle size < 1.5 µm, Global Tungsten & Powder) and submicron WC particulates (99 % purity with particle size in the range 0.15-0.2 µm, Sigma-Aldrich); the impurity contents of both powders, as provided by the supplier, are listed in the Supplementary information file (Table S I). In the final consolidated product, the phases were identified as *bcc* tungsten (W) and trigonal di-tungsten carbide (ε-W$_2$C) [21,23]. Before the He-implantation experiment, the W/W$_2$C composite was mechano-chemically polished to a flat, defect-free finish. The final size of the polycrystalline composite samples was a disk approx. Ø 15 mm × 2 mm.

2.2. Helium implantation experiments

The W/W$_2$C composite samples were mounted perpendicular to the ion beam and implanted at room temperature with 1 MeV ^{4}He$^+$ ions using a tandem-type ion accelerator (Tandetron, HVEE - High Voltage Engineering Europa B.V.) [24]. The implantation spot was 3×5 mm^2 in size, and an estimated amount of He atoms in the implantation zone was 1.2×10^{16}, resulting in a He ion fluence of 8×10^{16} He cm^{-2}. The He ion depth distribution and damage profile were calculated using Stopping and Range of Ions in Matter (SRIM) software [25], run in SRIM Kinching-Pease for bulk W target with displacement energy of E_d=90 eV, predicting He implantation depth of 1.4 μm at above-mentioned implantation conditions, with the maximum He concentration of ≈3.5 at. % (35,000 appm), while creating about 0.6 displacement per atom (dpa), on average.

2.3. Annealing

After He implantation, the samples were annealed at 1873 K for 20 minutes with a 5 K/min heating rate in a high-temperature vacuum furnace (Astro, Thermal Technology LLC.). Before each experiment, the furnace was thoroughly purged with Ar (HiQ 4.8, 99.998% pure) and evacuated (20 – 35 Pa). During annealing, the temperature was monitored by conventional thermocouples up to 1837 K, and above this value by the pyrometer.

2.4. Electron microscopy

2.4.1. Scanning electron microscopy

The surface morphology alterations and other effects induced by He-ions were studied using a focused ion beam - scanning electron microscope (FIB-SEM, Helios Nanolab 650i, FEI), operated at 15 kV. The cross-section trenches were made by focused ion beam (FIB) utilising Ga$^+$ ions. Quantitative microstructural analysis in the Scanning Electron Microscope was performed by electron backscatter diffraction (EBSD, Hikari Super, EDAX AMETEK and Nordlys II, Oxford Instruments plc) and interpreted by the OIM Matrix^{TM} and Channel 5^{TM} (HKL Technology, Inc.) analysis software.

2.4.2. Transmission electron microscopy

Atomic-scale observations, crystal structure and phase composition of the He-implanted samples were characterised in a 300 keV transmission electron microscope (TEM, Titan Themis G^2, Thermo Fisher Scientific). In scanning operation mode, micrographs were recorded by a high-angle annular dark-field detector (HAADF; Fischione Instruments, Model 3000) with a semi-convergence angle of 23.8 mrad and a camera length of 100 mm, resulting in inner and outer semi-collection angles of 73 and 200 mrad, respectively. For selected area electron diffraction (SAED) experiments, conventional 200 kV TEM (JEM-2100, Jeol Inc.) was used, equipped with a slow-scan CCD camera (Orius SC1000, Gatan Inc.). Bright-field scanning transmission electron microscopy (BF-STEM) was performed by 200 kV STEM (JEM-2010F, Jeol Inc.). TEM micrographs were processed by Digital Micrograph, ImageJ [26] and QGIS [27] software packages. Transparent thin foils for transmission electron microscopy (TEM) experiments were prepared using a site-specific focused ion beam (FIB) lift-out technique (Helios Nanolab 600i, Thermo Fisher Scientific). The initial lift-out was done by using 30 keV Ga$^+$ ions, while during milling and final thinning, the accelerating voltage was decreased to 5 keV to mitigate re-deposition and surface damage of the sample.

2.5. Theoretical background and computational concepts

To understand the dissolution behaviour of He in W and W$_2$C, we looked into the presence of possible trapping sites in the bulk of these materials. Tungsten is considered in its bcc ground state. The structure of W$_2$C is made up of a *hcp* tungsten sublattice, where one-half of the trigonal-prismatic interstices is occupied by carbon atoms in a specific way [28]. There are three possible sites for a single He atom in *bcc* tungsten, including the tetrahedral interstitial site (TIS), the octahedral interstitial site (OIS) and the W vacancy site (W-vac). To understand the preferable location for He in *bcc* W, we investigated the He solubility at the interstitial and substitutional sites using the following relation:

$$\Delta H_{He} = E(He\ in\ W) - E(W) - \mu_{He}, \tag{1}$$

where $E(He\ in\ W)$ and $E(W)$ are the DFT energies of supercells with and without He. The chemical potential of a He atom, μ_{He},

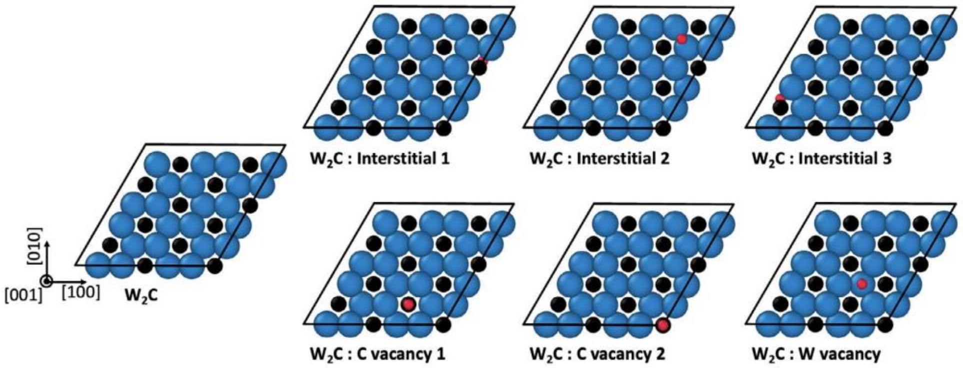

Fig. 1. Different positions in the ε-W_2C structure that can be occupied by a He atom (red spheres). The blue and black spheres represent W and C atoms, respectively.

is here considered as the energy of isolated He atoms in vacuum (i.e., a large supercell). To understand the He behaviour in ε-W_2C, the solubility of He at 0 K is determined (Eq. (2)) in different interstitial positions (IS-1, IS-2, IS-3), C vacancy sites (C vac-1, C vac-2) and W vacancy sites (W-vac) as shown in Fig. 1:

$$\Delta H_{He} = E(He\ in\ W_2C) - E(W_2C) - \mu_{He}, \tag{2}$$

where $E(He\ in\ W_2C)$ and $E(W_2C)$ are the DFT energies of a $2 \times 2 \times 2$ ε-W_2C supercell with and without He. The W vacancy formation energy in bcc W and W_2C is calculated as:

$$E^{form}_{W-vac} = \{E(W\ with\ W\ vac) + \mu_W\} - E(perfect\ W), \tag{3.1}$$

$$E^{form}_{W-vac} = \{E(W_2C\ with\ W\ vac) + \mu_W\} - E(perfect\ W_2C). \tag{3.2}$$

Here, μ_W is the energy of a W atom in a bcc cell. Similarly, the C vacancy formation energy in W_2C is calculated using:

$$E^{form}_{C-vac} = \{E(W_2C\ with\ C\ vac) + \mu_C\} - E(perfect\ W_2C), \tag{4}$$

where μ_C is the energy of a C atom in the octahedral site of *bcc* W, which is lower than the same in the tetrahedral site. The chemical potential reference of the C atom is considered under the assumption that the W_2C is precipitated from the C in the bcc W matrix. To analyze a potential agglomeration of He atoms, we calculate their effective binding energy in W and W_2C for different configurations with respect to the distance between He atoms:

$$E^b_{(He_1,He_2)} = \{E(He_1) + E(He_2)\} - \left\{E(He_1 + He_2) + E_{ref}\right\}. \tag{5}$$

Here, $E(He_1)$ and $E(He_2)$ are the energies of the supercell containing He_1 and He_2, respectively. $E(He_1 + He_2)$ is the energy of the supercell containing both He atoms. E_{ref} is the supercell without He_1 and He_2. All the supercells have the same size. Free surfaces of W and W_2C are modelled for evaluating the behaviour of He at open voids. The solubility of He at all the possible surface and sub-surface sites are investigated using similar equations as in Eqs. (1) and (2). A possible decohesion of bulk leading to free surfaces due to the presence of clusters of He atoms is also taken into account as a decohesion energy (γ^{He}_{dec}).

$$\gamma^{He}_{dec} = \gamma^{no-He}_{surf} - \left(\frac{N}{2A} \cdot \sum_N \Delta H^{He}_{bulk}\right) \tag{6}$$

Here, γ^{no-He}_{surf} is the surface energy of W or W_2C without any He atoms, since the latter will diffuse into the open vacuum, i.e., the chemical reservoir for the second term. ΔH^{He}_{bulk} is the solution enthalpy of each He atom in the cluster. Further, N is the number of He atoms in the considered cluster, and A is the area of the cell in which the clusters are present; the factor 2 is due to the formation of two surfaces upon decohesion.

2.6. Computational details

Density functional theory (DFT) calculations have been performed using the Vienna Ab-initio Simulation Package (VASP) [29,30]. The projector-augmented wave (PAW) [31,32] method is employed with an energy cut-off of 520 eV, which we find to be sufficient to converge the total energies of W and W_2C to 1 meV per atom. This cut-off is higher than in previous studies [33], yielding a difference in absolute values and justifying that some calculations for He in W have been repeated. Exchange-correlation is treated within the generalized gradient approximation (GGA) in the formulation of Perdew, Burke, and Ernzerhof (PBE) [34]. Brillouin zone integration is performed by the scheme of Monkhorst and Pack [35] using k-point grids of $8 \times 8 \times 8$ and $6 \times 6 \times 6$ for a supercell of $3 \times 3 \times 3$ W and $2 \times 2 \times 2$ of ε-W_2C, respectively. Partial band occupancies were considered using the smearing scheme of Methfessel and Paxton [36] with the smearing width of 0.2 eV. All the calculations were done at constant volume by relaxing the atomic positions unless otherwise indicated. The lattice constant of bulk *bcc* W is calculated to be 3.184 Å, and for ε-W_2C, it is found to be 5.249 and 4.773 Å. Comparison with other methods is given in the Supplementary information file (Table S II), and the values are in acceptable agreement. The minimum energy path (MEP) and the diffusion barrier for He in a body-centred cubic W matrix and trigonal W_2C are computed with the climbing image nudged elastic band (CI-NEB) method [37,38] as implemented in VASP, using the transition state theory tools (VTST) code [39]. The initial and final structures are created from $3 \times 3 \times 3$ bcc supercells (54 atoms) of W and $2 \times 2 \times 2$ supercells (72 atoms) of W_2C for the diffusion studies. A set of nine images or configurations are chosen in between the initial and final state to generate the minimum energy path for both W and W_2C. All the configurations are relaxed until a total force convergence of 0.05 eV/Å is achieved.

3. Results and discussion

3.1. Initial composite microstructure

The detailed microstructure analysis and phase composition of the starting composite material, the as-sintered W/W_2C composite, is reported in [21]. The results of EBSD analysis of the native, non-irradiated and non-annealed W/W_2C composite microstructure are summarised on Fig. 2. The composite has a bimodal grain size distribution: the W grains have a size range of 1.0 - 26.7 µm with a mean size of 7.5 µm in diameter (standard deviation (SD) 4.6), while the W_2C grain size ranges from 0.4 µm to 3.2 µm, with mean size 1.1 µm (SD 0.27); further details on the measurements are presented in the supplementary information file (Fig. S6). Most

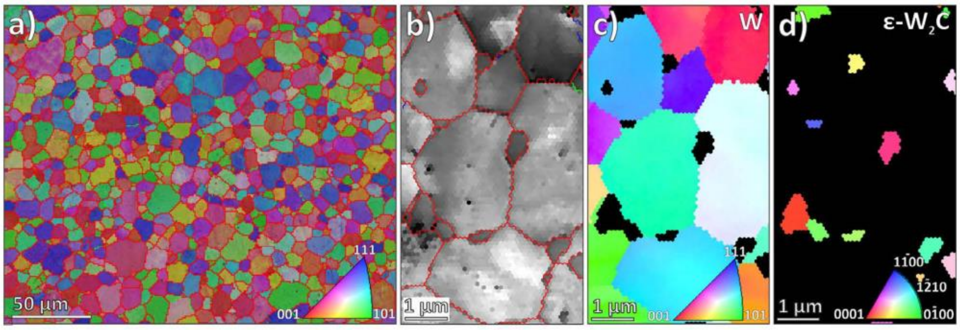

Fig. 2. Microstructure of native non-irradiated non-annealed W/W$_2$C composite sample. (a) EBSD band contrast image overlaid with an inverse pole figure (IPF-X) orientation coloured grain map and grain boundaries (green colour > 10° and red colour > 15°). (b) EBSD band contrast image overlaid with grain and phases boundaries. (c) W and (d) W$_2$C crystal grains, with colour keys for the IPF and <001> inverse pole figures in insets.

of the W grain boundaries have > 15° misorientation angle, and no orientation relationship between W and W$_2$C grains was observed (Fig. 2(a) and Fig. 2(b)). The W$_2$C phase is primarily found at the W grain boundaries, preferentially at triple junctions, as shown in Fig. 2(c) and Fig. 2(d)

3.2. Helium-induced microstructure alterations

For the microscopy studies, single-energy ion implantation was selected to produce a narrow subsurface damage region, deep enough to avoid the influence of the surface, and at the same time still accessible for the FIB sample preparation. The He-implantation was performed at room temperature, as it is reported to produce visible He bubbles only at the vicinity of He ion range in the material, while He-implantation at elevated temperatures results in He bubble formation throughout the entire irradiated region [40]. Fig. 3 show the SEM micrographs of the He implanted sample before annealing (Fig. 3a–c) and after annealing (Fig. 3d–f).

After room temperature He implantation and before annealing, a minor amount of surface defects was observed, as shown in Fig. 3(a); however, the 1 MeV He ion implanted sample does not show any swelling or other morphological features. In the SEM cross-section shown in Fig. 3(b), individual W grains are easily distinguishable by electron channelling contrast, caused by signal intensity variation resulting from changes in the angle of the incident electron beam and the crystal lattice of the investigated grains [1]. The interesting feature is a contrast enhancement inside single W grains (Fig. 3(b) and Fig. 3(c)), coinciding with the SRIM predictions for the He implantation depth (Fig. 4(b)). Such contrast variation is observed only in the implanted zone and not in the shielded, non-irradiated region of the sample. Based on the physical mechanism of electron channelling contrast generation, we relate this contrast enhancement to the crystal structure alteration induced by He implantation (further details can be found in the supplementary information file (Fig. S1-S4).

The thermal annealing of the room temperature He-implanted samples is used to study bubble evolution at a given He content [7]. In W, when implanted above the lattice displacement energy (90 eV), He will form tightly bound configurations with vacancies [41]. At temperatures below 550 K, vacancies are immobile and do not cluster [42], although the vacancy clusters can also be created during irradiation. The formation of the He bubbles was observed over the minimum concentration of 600 appm [43], and He is retained in the matrix up to 2273 K [16], mainly because of the high de-trapping energy that is necessary to release He from vacancy complex [44], e.g. to overcome the He-vacancy bond formed during implantation [45]. On the other hand, if implanted below the lattice displacement energy responsible for defects generation, He is fully released from the W matrix already at 1873 K due to the lack of suitable trapping sites [41]. Based on these assumptions, the temperature of annealing was set at 1873 K.

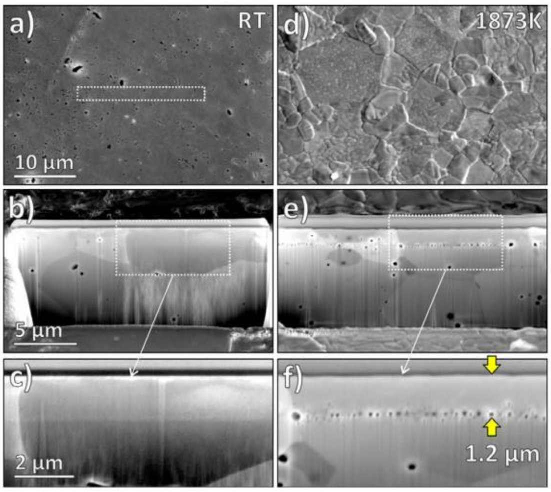

Fig. 3. Secondary electron (SE) SEM micrographs: (a) the irradiated sample surface, with a marked area for the FIB cross-section. (b) The enhanced contrast inside a single W grain coincides with the He implantation depth; with the magnified marked region in (c). The same FIB cross-section was investigated after the annealing; (d) the surface of the sample was recorded in the immediate vicinity of the original cross-section, as the location in (a) was already etched by FIB. The observation of the same cross-section in (b) after the annealing (d) show that the bubble network developed at a depth of implantation damage peak at 1.2 µm; the marked region is magnified in (f).

After annealing at 1873 K for 20 min, the surface of the sample shows a reduction of defects and grain boundary grooving, as seen in Fig. 3 (d). In the cross-section, the microstructure evolution of the irradiated sample shows the formation of the bubble network coinciding with the SRIM predictions for the peak damage depth at ~1.2 µm below the surface (Fig. 3(e) and Fig. 3(f)). After annealing, the electron channelling contrast in the implanted region is consistent with the rest of the W grain, as seen on Fig. 3(f).

An electron-transparent TEM sample was prepared by FIB from the He-irradiated and annealed W/W$_2$C composite sample to analyse and quantify the nano-scale radiation damage, He-bubble formation and their effect on the composite microstructure.

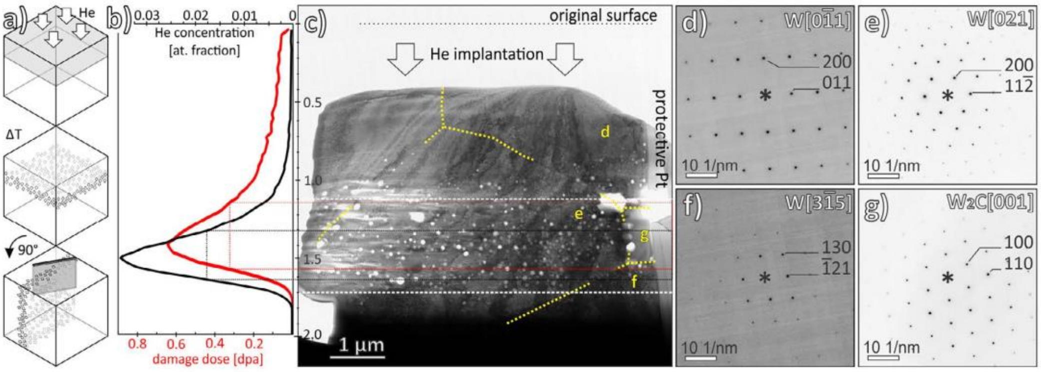

Fig. 4. (a) Outline of the sample history: He implantation, annealing, cross-section and lamella positioning. (b) SRIM simulation of the depth distribution of ^{4}He concentration (black curve) and damage dose distribution (red curve) for the implantation fluence of 8×10^{16} He cm^{-2} in W. (c) Overview TEM micrograph, with marked main He bubble region between 1.1 µm and 1.7 µm (white dotted lines); the vertical scale is corrected for a tilt angle. The grain boundaries are marked outside the main implantation zone by yellow lines. The grains were identified by SAED as *bcc* W (d, e and f) and *hcp* ε-W_2C (g). The striations around bubbles, especially on the left side, are due to the curtaining effect of the FIB ion-milling. Around W_2C grain (region g), a large hole developed during FIB milling, as materials with high milling rates will mill faster, and the lamella will be thinner in those regions.

Fig. 4 shows the TEM sample procedure and the overview TEM micrograph with outlined main features. The bulk sample was first cut perpendicularly to expose the bubble formation zone. The TEM lamella was cut from the intersection of the bubble network with W and W_2C grains, as schematically displayed in Fig. 4(a); the details on the sample micro-location and procedures are listed in the supplementary information file (Fig. S7 and S8). The TEM lamella was prepared at an angle to enhance the otherwise only 0.5 µm thick main implantation region, a procedure that must be considered when measuring the actual implantation depth from the TEM micrographs.

In the TEM sample, the main implantation zone is easily recognisable by heavy bubble accumulation, as shown in Fig. 4(c), consistent with the reports on polycrystalline W implantation at room temperature [40]. The maximum concentration of bubbles has been observed between 1.1 µm and 1.7 µm, which coincides with the damage distribution peak depth calculated by SRIM (Fig. 4(b): He concentration FWHM (black lines) = 1.30-1.62 µm and dpa FWHM (red lines) = 1.12-1.55 µm). In the next step, the crystal structure of the individual grains in the W/W_2C composite was identified by selected area electron diffraction (SAED) presented in Fig. 4(d-f). The crystal structure of the larger grains corresponds to body-centred cubic *(bcc)* W. Smaller grains were identified as primitive trigonal/rhombohedral *hcp* ε-W_2C (Fig. 4(g)). The main implantation zone intersects several W-W grain boundaries, as well as a W|W_2C phase boundary.

As the thin TEM lamella was prepared at an angle, it was possible to analyse the bubble formation in detail concerning their density, spatial distribution, and their relation to the subgrain features, as shown in Fig. 5(a). The bubbles are observed in a projection, and a Feret diameter was used to measure their size [46]. The overall bubble size, presented in Fig. 5(f) shows bimodal size distribution typical for two different generation processes, where smaller mode peaks at 15-35 nm and the larger one corresponds to bubbles > 50 nm in size. Due to such large size variation and to determine the local bubble size distribution, the sample was segmented into several sectors regarding the main implantation zone, which is marked at 1.1-1.7 µm below the surface on Fig. 5(a). Above the main implantation zone, towards the surface (Fig. 5(d)), the bubbles are in the range of 20 to 30 nm (Fig. 5(i)); in the main implantation zone (Fig. 5(c)), the average bubble size is 60-80 nm (Fig. 5(j)), and below the implantation zone, the bubble size again decreases to 30-50 nm (Fig. 5(k)). Outside the main implantation zone, the bubbles are limited to structure defects and grain boundaries (GBs) (Fig. 5(c, d)). In the main implantation zone on the W-W grain boundaries (Fig. 5(b)), the average bubble size is in the range of 30 - 50 nm (Fig. 5(g)), while several bubbles found at the W|W_2C phase boundary are exceptionally large (Fig. 5(e)), with a diameter of about 200-400 nm as shown in Fig. 5(h); besides related to the interface, no other bubbles were detected inside the W_2C grain.

Investigations of He implantation in polycrystalline W report typical bubble sizes in the range of several nm (e.g. [43]), while in our material, they are by order of magnitude larger. The final bubble size is a result of He bubble evolution and can be separated into two distinct phases: bubble nucleation and initial growth during He implantation and bubble coarsening during annealing [7]. During the implantation stage at low temperatures, the thermal dissociation from He atom traps is negligible, and the nucleation and initial growth of bubbles are driven by the presence of He trapping sites and extended defects such as grain boundaries [7,15]. The bubble coarsening during annealing is in the literature explained by two qualitatively different mechanisms: bubble migration and coalescence, and Ostwald ripening [7]. He bubbles coarsening results in bubble growth, while at the same time, their density is decreased. Additionally, at elevated T >1500 K, He clusters have a higher probability to merge with the pre-existing bubble, resulting in accelerated bubble growth [47].

In a perfect defect-free lattice and under consistent He implantation, the bubbles should be evenly distributed in the implantation zone. Upon annealing, the bubbles would form a uniform distribution net when following the thermodynamic precipitation strictly, with each bubble equally separated from the neighbouring bubble, forming a bubble supercell constellation. In our realistic sample, even in the main implantation zone, the bubble distribution near the GBs differs from the bulk grain, as shown in Fig. 6(a). To assess this discrepancy, we considered the analysed lamella as a finite Euclidean plane, where bubbles represent a given set of points, and perform centroidal tessellation to determine bubble density and separation. The resulting Voronoi diagram on Fig. 6(b) illustrates the interdependence between bubbles in the W grains, structure defects and grain boundaries. The majority of the bubbles are separated for 100 nm or less, as seen on the nearest-neighbour distribution graph in Fig. 6(c). Moreover, bubbles have a non-random, clustered spatial repartition, as we can deduct when comparing the experimental data with the calculated

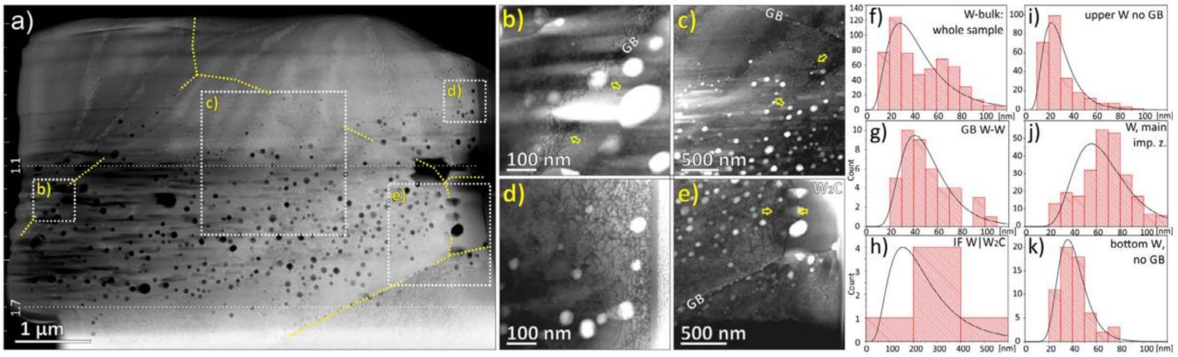

Fig. 5. a) HAADF-STEM overview micrograph, with marked GBs (yellow lines) and regions of BF-STEM insets (white squares): b) bubbles at the W-W GB; c) bubbles outside the main implantation zone are limited to GBs (yellow arrows); d) He bubbles in the W grain outside main implantation zone, near sample surface; e) large elongated bubbles on inclined W|W$_2$C interface (arrows mark upper and bottom contact). Ferret diameter of bubbles per different regions; f) entire analysed sample, g) only bubbles on the W-W grain boundaries, h) bubbles on W|W$_2$C interface, i) upper W without GB, j) all bubbles in the main W implantation zone, k) bubble size below the main implantation zone.

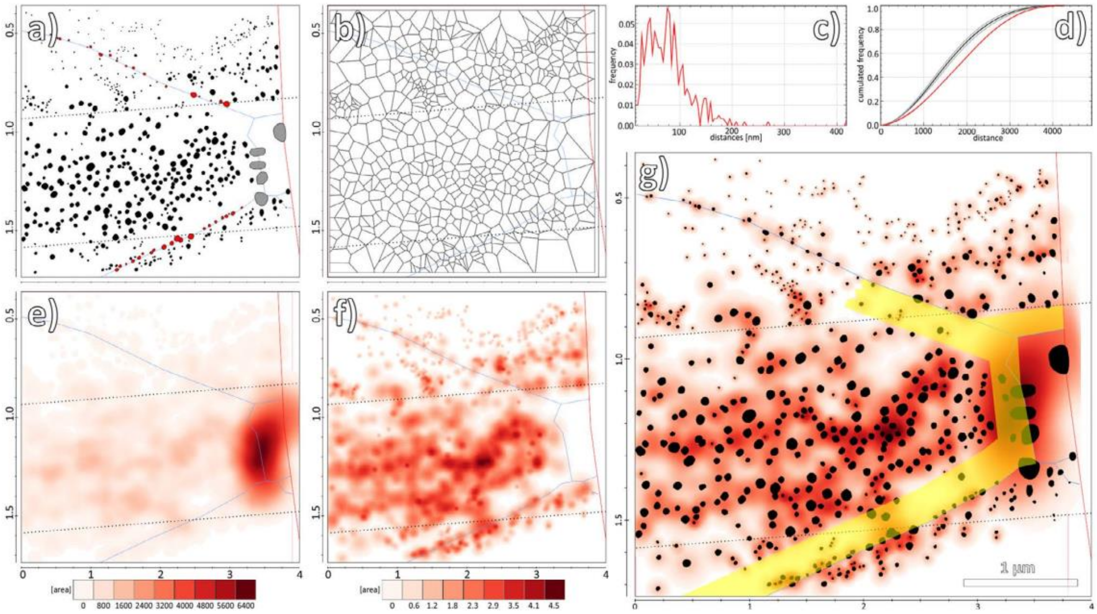

Fig. 6. (a) Spatial distribution of bubbles (N=615), red bubbles are on the W-W grain boundaries; blue lines mark the grain and phase boundaries, and dotted near-horizontal lines mark the main implantation zone. (b) Voronoi diagram, with underlined main features from TEM micrographs. (c) The cumulative distribution function of the distance between a bubble and its nearest neighbour. (d) Bubble distribution pattern compared to Spatial Distribution Index - a normalized measure of the difference between the observed point distribution and a completely random one. The black line indicates the average distribution for random patterns, the grey lines indicate the 95 % confidence interval, and the red line corresponds to the distribution of the observed bubble pattern. The observed distribution lies right of the confidence interval, indicating a clustered organization. (e) Heatmap based on Kernel Density Estimation, with an area of underlying bubbles as weight; (f) same, but calculated without the bubbles on the W|W$_2$C interface, to enhance the influence of the GBs and defects. g) Cumulative heatmap and bubble outlines; yellow zone marks the 150 nm thick void denuded zone developed next to GBs.

cumulative distribution function of spatial distribution index, included as Fig. 6(d).

As Voronoi polygons consider only the spatial arrangement of the bubbles, the Kernel Density Estimation (KDE) algorithm [27] was used to interpret the interplay between the size of bubbles (their "weight") and their spatial distribution. From generated KDE heatmaps display in Fig. 6(e) and Fig. 6(f), we can conclude that the highest He concentration coincides with the centre of the projected implantation zone. It is important to note that bubble growth at the grain boundaries suppresses further He supply to the bubbles and hence to their arrested growth and confinement, an effect observed in materials with a high density of sinks [48,49]. In our sample, a considerable void denuded zone (VDZ) developed around defects, with an average thickness of ≈150 nm, outlined on Fig. 6(g). Helium is detrimental to properties of both metals and ceramics alike, and the bubble formation, surface blistering and exfoliation due to helium have been reported in various transition-metal ceramics [15]. In contrast to W, in W$_2$C grain, no defects and consequently no bubbles were observed besides exceptionally large bubbles at the phase (Fig. 5(e) and Fig. 6(g)). The evolution

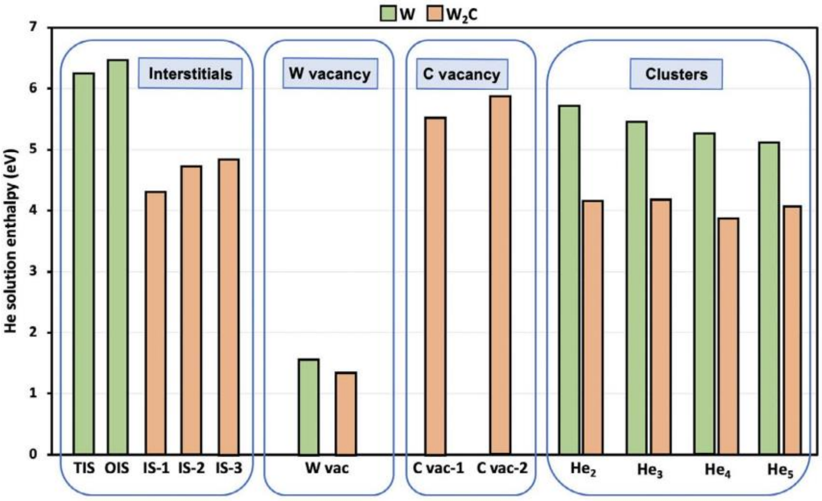

Fig. 7. Solution enthalpy of He in different interstitial sites, C vacancy sites and W vacancy sites in bcc W and W_2C. The reduced solution enthalpy of interstitials (TIS in W & IS-2 in W_2C) due to clustering is given in the clusters portion of the figure. The green bars correspond to W, and orange bars correspond to solubility in W_2C.

Table 1
Binding energy of He clusters in W_2C carbide and W (in eV).

	W		
Cluster size	54 atoms (present work): TIS spherical morphology (eV)	128 atoms (Becquart *et al.* [33]): spherical morphology (eV)	
He_2	0.97	1.03	
He_3	2.31	2.39	
He_4	3.68	3.90	
He_5	5.57	5.54	
	W_2C		
Cluster size	108 atoms (3 × 2 × 2 supercell): linear morphology (eV)	72 atoms (2 × 2 × 2 supercell): spherical morphology (eV)	
He_2	(IS-2 & IS-3) 1.15	(IS-1 & IS-2) 0.104	(IS-1 & IS-1) 0.76
He_3	(IS-2 & IS-3 & IS-2) 1.72	(IS-1 & IS-2 & IS-3) 1.02	(IS-1 & IS-1 & IS-2) 0.61
He_4	(IS-2 & IS-3 & IS-2 & IS-3) 3.42	(IS-1 & IS-2 & IS-3 & IS-2) 2.32	(IS-1 & IS-1 & IS-2 & IS-2) 1.44
He_5	(IS-2 & IS-3 & IS-2 & IS-3 & IS-2) 3.38	(IS-1 & IS-2 & IS-3 & IS-2 & IS-3) 3.29	(IS-1 & IS-1 & IS-2 & IS-2 & IS-3) 3.19

of bubbles at GBs is controlled by fluxes of He atoms to such sites, which constitute effective local He production rates there, and these fluxes are controlled by the bubble evolution within the bulk of the matrix. Thus, the bubble evolution at extended defects is strongly coupled to that in the bulk [7].

3.3. DFT simulation on helium behaviour in W and W_2C

To explore the fundamental aspects leading to the anomalous He bubble formation in the W/W_2C composite material after ion implantation and annealing, we studied the energetics and kinetics of isolated He atoms, and He clusters in W and ε-W_2C using first-principles based DFT calculations as given in Fig. 7, Table 1 and Table 2.

3.3.1. Helium behaviour in W and W_2C

(a) Solubility studies of isolated He atoms. Upon investigating the solubility profile of He in W, we find that the previously reported preference of the tetrahedral among the interstitial sites in *bcc* W [33,50] is due to the larger available Voronoi volume compared to the octahedral site (Fig. 7 and Fig. S12). The larger interstitial volume is also confirmed through a hard-sphere model analysis [50]. The energetically most favourable location for He in bcc W is the W vacancy site, which again follows the trend that the solution enthalpy of He is proportional to the corresponding Voronoi volumes (Fig. S12 in supplementary material). In fact, the reduction of the He energy from interstitial to a W vacancy site is larger than the W vacancy formation energy (Eq. (3.1) and (3.2)) (Table S III in supplementary material). Still, the energetics of resulting W self-interstitials make this scenario rather unlikely. However, it is worth to mention that vacancies are also created during the irradiation, and the He will be by default bound to these irradiation-induced defects.

In W_2C, He prefers to occupy any of the three interstitial positions (for IS-1, ΔH_{He} = 4.32 eV) rather than the most favourable C-vacancy position (for C vac-1, ΔH_{He} = 5.54 eV) (Eq. 4). This is again a volumetric effect because the Voronoi volume is larger in the interstitial site (for IS-1, 8.98 Å^3) as compared to the C vacancy site (for C vac-1, 8.52 Å^3). Out of all the available sites, the most suitable one for He in W_2C is a W vacancy site due to its bigger

Table 2
Possible diffusion paths and corresponding migration energies of He in W and W_2C (eV). The migration of He atoms from IS-1 to another IS-1 site is a non-repetitive process, unlike the IS-2−> IS-3−> IS-2 path.

	Migration energy of He in W (eV)			
Diffusion path	Present work	Previous DFT studies	Previous empirical methods	Experimental
TIS → TIS	0.08	0.06[a], 0.07[b]	0.02[d]	0.28[f],
TIS → OIS → TIS	0.26	0.22[b], 0.23[c]	0.18[d]	0.24-0.32[g]
	Migration energy of He in W_2C (eV)			
Diffusion path	Present work			
IS-1 → IS-1	0.143			
IS-2 → IS-3 → IS-2	0.138			

[a] Becquart et al. [33],
[b] Zhou et al. [50],
[c] Zhou et al. [51],
[d] Li et al. [52],
[f] Amano and Seidman [53],
[g] Wagner and Seidman [54].

interstitial volume (13.77 Å^3). Compared to bcc W, it is easier to create a W vacancy in the carbide (Table S III in supplementary material). Combined with the fact that the sum of W vacancy formation plus He substitution is energetically more favourable than placing He in interstitial sites, it might be a possible scenario that isolated He atoms generate and occupy W vacancies during ion implantation in W_2C. Because of the high solution enthalpy value of He in W (6.25 eV at TIS), we conclude that these He atoms are found as insoluble atoms in bcc W. Thus, He incorporation into metal W is energetically unfavourable, suggesting a high propensity to form bubbles. While the solution enthalpy value is also positive for He in ceramic W_2C, the smaller absolute value suggests a lower propensity to form bubbles.

(b) Binding energy between He atoms and cluster formation. The effective binding energies of He in bcc W and ε-W_2C, which is mainly caused by elastic distortions of the host lattice, are investigated as per Eq. (5) to understand the clustering tendency and self-trapping behaviour of He. Table I summarizes the binding energy of He clusters in W_2C carbide and W. According to Becquart *et al.* [33], the most attractive He-He binding energy between two He atoms separated by a distance of 1.50 Å is 0.96 eV and 1.03 eV in a 54 and 128 atoms supercell of W, respectively. Similar results have been obtained in our current study, with He-He binding energy in tetrahedral sites of bcc W as 0.97 eV in a 54 atoms supercell (Table 1). Conducting similar investigations in ε-W_2C provided the conclusion that there is a positive binding energy indicating an attractive interaction for He atoms located in nearest neighbour positions. As the distance between He atoms increases, the interaction between them decreases. The most positive binding energy is between a He-He pair in IS-2 & IS-3 sites that are at a distance of 1.55 Å (first column in Table 1). More details of possible arrangements chosen for He-He binding energies in ε-W_2C and the corresponding He-He final distances after relaxation are shown in the supplementary file (Table S IV). The binding energy between He atoms in W_2C is slightly more attractive than the same in bcc W, as given in Table 1. The attractive binding energy results in the reduction of the solution enthalpy of He atoms (Fig. 7), making the He atoms relatively even more soluble in W_2C than in bcc W. Thus, the thermodynamic driving force for bringing He atoms into the gas phase is slightly reduced in W_2C compared to W, although the large positive solution enthalpies indicate that this is not the dominant mechanism.

The cluster binding energies per atom in W are found to increase with the cluster size, indicating the preference of forming large clusters (Table 1). Considering the fact that there are 12 TIS available in a bcc W unit cell and that the clustering profile of He in bcc W yields a preference of clusters with up to five atoms in one unit cell itself, the He clusters show a compact morphology in the structure.

The He-clustering tendency in W_2C is found to be possible up to a cluster size of four atoms, as the binding energy decreases for the He_5 configuration (Table 1). These four He atoms are distributed over a 2 × 1 × 1 unit cell of the carbide in a linear chain-like morphology, suggesting a less compact character of the clusters. In the presence of a W vacancy next to IS-2 sites, the clustering tendency is suppressed in W_2C, as single He atoms are strongly trapped in the metal vacancy site.

(c) Migration behaviour of helium atoms. The transport of He atoms is one of the key mechanisms for bubble nucleation and growth. Two possible diffusion paths are studied for the migration of a He atom from one tetrahedral site to another in bcc W. The minimum energy path of He atoms via an octahedral saddle site is found to have a diffusion barrier of 0.261 eV. Due to such a high migration barrier, the mobility of atoms through the octahedral saddle point is restricted. The diffusion barrier of He migrating between nearest neighbour tetrahedral sites (1.1 Å) without an octahedral site as saddle point is much smaller with a value of 0.08 eV. The results are in agreement with previous literature (Table 2), including the work of Becquart et al., Ref. [33]. They have explained the deviation in *ab-initio* migration energy from experimental values by the self-trapping caused by the large binding energy between He atoms in W (see discussion above).

Migration barriers for both considered diffusion paths in W_2C (Table 2) are slightly larger, having a value of approx. 0.14 eV. However, also in this case, the clustering of He atoms can result in a self-trapping, which is due to the high number of potential configurations hard to quantify. Therefore, it can be concluded that from a kinetic perspective, there is no difference in the propensity of bubble formation in W and W_2C.

(d) Decohesion and surface adsorption of He in W and W_2C. He bubbles are expected to form preferentially at interfaces since they can act as He trapping sites and the reduced W-W bond energies promote the formation of new surfaces. Indeed, anomalously large He bubbles are observed at the W|W_2C interfaces in the experiment but studying their formation mechanisms by computer simulations does not seems feasible. Instead, we focus on the experimentally more interesting differences in bubble formation in the interior of the W and W_2C grains. In order to analyze the corresponding decohesion, the behaviour of He at two different surfaces is studied for both W and W_2C.

With the consideration that the (110) surface is the most stable for W, we have investigated the solubility of He in all the relevant

Table 3
Decohesion energy of W and W_2C surfaces due to the presence of He clusters. The cluster of size five or less can be present in the unit cell of W [110] surface. Clusters of size up to three He atoms are formed within a unit cell area of W_2C [0001], unlike He_4, which is formed at a 2 × 1 × 1 surface of W_2C [0001]. Hence the corresponding area in respective cases is considered for determining the He coverage.

Cluster size	Surface energy, γ_{surf}^{no-He} (J/m^2)	Decohesion energy, γ_{dec}^{He} (J/m^2)
	W *bcc* [110] surface	
He_1	3.28	-0.21
He_2	3.28	-3.41
He_3	3.28	-6.46
He_4	3.28	-9.41
He_5	3.28	-12.28
	W_2C *hcp* [0001] surface	
He_1	2.60	1.22
He_2	2.60	0.01
He_3	2.60	-1.21
He_4	2.60	0.13

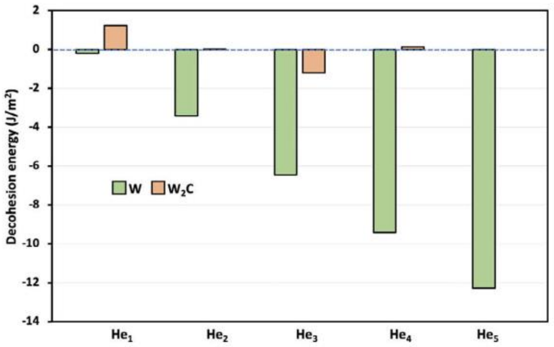

Fig. 8. The decohesion energy of free surfaces of W (110) corresponding to green and W_2C [0001] corresponding to orange bars, are plotted as a function of a number of He atoms forming clusters.

surface and sub-surface sites. It turns out that these two layers do not provide stable configurations for He atoms, which prefer to diffuse into the vacuum region. From the 2nd atomic layer onwards, the solution enthalpy is close to the bulk value of 6.2 eV. Wang *et al.* [55], who reported similar results for the W (110) surface, also speculated that He clusters could easily form next to surfaces due to higher binding energy and a longer self-trapping range as compared to the bulk. We obtain the He behaviour at the W (100) surface to be similar, with the additional effect that the dissolution of He from the surface sites in W (100) causes a surface reconstruction and a reduction of the surface energy (from 4.05 J/m^2 to 3.97 J/m^2). Similar to He at W (110), all the surface and subsurface sites are energetically unfavourable for He in W (100) as compared to a diffusion to vacuum. For understanding the dissolution behaviour of He in W_2C, the hcp (1000) and (0001) surfaces are studied. Among them, W_2C (0001) has the lower surface energy. Similar to He atoms at W surfaces, even in carbide, the surface and sub-surface sites are not stable for He in both surfaces, and He escapes to vacuum, providing a solution enthalpy of 0 eV. Hence, single He atoms will release an energy equivalent to their solution enthalpy in the bulk whenever a free surface is formed. Considering the clustering tendency of He in the bulk, all atoms in a cluster (like He_4 or more) would collaboratively contribute in such a way to the reduction of the surface formation energy.

Thus, the decohesion energy of surfaces due to the presence of the most likely cluster of He atoms (He_5 in W and He_4 in W_2C) is calculated following Eq. (6). According to Table 3 and Fig. 8, the decohesion energy of the most stable surface in W is -12.28 J/m^2 and the same in W_2C is 0.13 J/m^2. In the case of W_2C, the clusters with a size of three He atoms or less are formed within a unit cell and He_4 onwards are formed in a 2 × 1 × 1 cell. It is more likely to find clusters with a size of four He atoms distributed over two cells than finding He_3 in every unit cell. Moreover, considering the clustering tendency in W_2C (Table 1), the probability of finding clusters of He_2 or He_4 is very high as compared to He_3 or He_5. Hence the negative decohesion energy for He_3 in W_2C is non-substantial. Therefore, the impact of He on generating free surfaces or a crack within the grain interior is substantially higher in W as compared to the carbide. In order to evaluate the tendency of He related to bubble formation, one has to take into account that the decohesion needs to affect more unit cells than the one containing the He clusters. Therefore, the driving force for bubble formation actually needs to be a weighted average of the surface energy and the He-supported decohesion energy. This average can easily be negative in the case of W. In the case of W_2C, the already positive decohesion value for a cluster with two or four He atoms will become even more positive when applying a weighted average with He free surfaces.

As deduced from experimental data, the behaviour of He in metallic W and ceramic W_2C is fundamentally different. The large accumulation of He on the phase boundary can present a severe obstacle for the applications of such materials as PFMs. The excess He accumulation on the interface will eventually cause the degradation of the structural stability of the material such as surface swelling and blistering and, in the extreme case, the loss of cohesion between W and W_2C grains, inflicting the fall-out of the W_2C grains from the composite. We have to underline that although the He implantation is widely accepted as a proxy for fusion reactor conditions, in a real working environment, we can expect synergistic effects of α-particles, neutrons and T-D fuel, all at elevated temperatures. We assume that the other cermet composites will behave similarly under He implantation, requiring further research and experimental evidence.

4. Conclusions

The implantation of ^{4}He into W/W_2C at room temperature, with subsequent annealing, was performed to study bubble evolution at a given He content. After annealing at 1873 K for 20 min, visible bubbles, which can be observed in cross-section SEM, appear in the sub-surface region at a depth of ~1.2 µm. The detailed TEM analysis of as-implanted and post-annealed sample shows bubbles throughout the as-prepared lamella, but surprisingly not in W_2C grain. These experimental observations were the motivation for theoretical calculations, which suggests a high propensity to form bubbles in metal W and a lower propensity to form bubbles in ceramic W_2C.

After the room temperature He implantation, the implantation zone depth can be already assessed from the SEM contrast variation observed in the cross-sections, a method that can significantly facilitate investigations of the ion-induced damage in materials. The observation of the composite sample, after the annealing at 1873 K for 20 minutes, shows that the He implantation dose was low enough to avoid surface blistering, but high enough to result in bubble formation in W grains and at W-W grain boundaries. Furthermore, oversized bubbles evolved at the W|W_2C interface. The bubbles can be observed in the whole implanted region, but they are concentrated and achieve the maximum size in the main implantation zone, 1.2 µm below the surface. The detailed TEM analysis of bubbles shows monomodal, non-random bubble distribution (30-80 nm) in W-grains and W-W grain boundaries. The distance between bubbles nearest-neighbour is < 100 nm. There is no significant difference in bubble size between bulk W and W-W GB;

on the other hand, large bubbles (200-400 nm) developed at the phase boundary, accompanied by an extensive void denuded zone (VDZ) with an average width of ≈150 nm.

In order to understand the bubble formation in W and the absence of bubbles in W$_2$C observed in experiments, we studied the solution energetics, clustering tendency, diffusion kinetics and decohesion caused by He atoms in W and W$_2$C. In both phases, He will primarily be incorporated into interstitial sites. Compared to He in a vacuum, this is an energetically highly unfavourable configuration, and there is a strong driving force for He to form bubbles. This driving force is substantially lower in W$_2$C but still clearly present. Nevertheless, in both W and W$_2$C, a single He atom is not sufficient for the nucleation of a bubble due to the large surface energy connected to the decohesion process.

There are two alternative mechanisms for W to lower its solution enthalpy. One is to form a W vacancy and occupy this position. Due to the lower vacancy formation energy in W$_2$C compared to W, this mechanism is more likely in the carbide and further reduces the driving force for bubble formation in this phase. Despite the high diffusion rate of self-interstitials in W [56], the large formation energy of Frenkel pairs makes the relevance of such a process questionable. The second mechanism is the clustering of He atoms, which is in W highly favourable. Clusters of up to five He atoms can form with a spherical morphology, which are hard to dissociate. Though there is strong binding energy among He atoms, the reduced solution enthalpy is still highly positive. In W$_2$C, clusters of four atoms or less can form in chain-like configurations, reducing the solution enthalpies again to lower numbers than in W.

More important than the solution enthalpy of individual W atoms is, however, their collaborative effect on the formation of free surfaces during decohesion. This process might be considered more favourable in W$_2$C than in W due to the lower surface formation energy in the pure phase. However, the substantially higher driving force for every He atom in W to reach a gaseous state, as well as the much more compact configuration of He clusters in W, invert the picture. We found that the decohesion of bulk W into free surfaces is energetically highly favourable in the presence of He clusters, while the driving force of He in W$_2$C is not sufficient to form free surfaces. This explains why a bubble formation is only observed inside W grains and not within W$_2$C. The comparative DFT study applied in this manuscript can be effectively adapted to other material systems to study the tendency for bubble formation.

Authors and their contribution list

The authors confirm contribution to the paper as follows: A. Š.: experiment design, manuscript draft, SEM and EBSD, and data curation; L. S.: DFT calculation and interpretation, manuscript drafting; S. M.: He-implantation experiment, design, simulations, and interpretation; M. K.: He-implantation experiment, design, and interpretation; J. Z.: TEM analyses and interpretation of the data; C. H. L.: electron microscopy and manuscript editing; G. D.: experiment design and manuscript editing; T. H.: interpretation of the DFT data and manuscript editing; M. Č.: manuscript editing and PhD supervisor; S. N.: contributed to the design of the project and supervised the project; P. J.: material development and selection, initial experiment design and manuscript editing.

Declaration of Competing Interest

The authors declare that they have no known competing financial interests or personal relationships that could have appeared to influence the work reported in this paper.

Acknowledgments

Katharina Hengge is greatly acknowledged for her help with the FIB preparation of the TEM samples. Barbara Šetina Batič is acknowledged for her help with the EBSD analyses. L.S. and T.H. acknowledge fruitful discussions with Prof. Dr. J. Neugebauer. A.Š. acknowledges financial support within the EUROfusion education & training scheme. This work has been carried out within the framework of the EUROfusion Consortium and has received funding from the Euratom research and training programme 2014-2018 and 2019-2020 under grant agreement No 633053. The views and opinions expressed herein do not necessarily reflect those of the European Commission. A.Š., J.Z., S.M., C.L. and G.D. acknowledge the support from Slovenian Research Agency and Deutscher Akademischer Austauschdienst, BI-DE/19-20-002; No. 57450885: "Investigation of helium retention in plasma facing materials using advanced analytical methods". Part of this work was supported by the Max-Planck partner group High performance materials headed by J.Z. and A.Š. P.J. and S.N. acknowledge the support from the Slovenian Research Agency (Contracts No. 1000-17-0106, J2-8165, P2-0087-2 and P2-0405-5). M. Č. acknowledge the support by European Union's Horizon 2020 research and innovation programs under grant agreement No 823717 –ESTEEM3.

Supplementary materials

Supplementary material associated with this article can be found, in the online version, at doi:10.1016/j.actamat.2021.117608.

References

[1] L.A. Giannuzzi, J.R. Michael, Comparison of channeling contrast between ion and electron images, Microsc. Microanal. 19 (2013) 344–349, doi:10.1017/S1431927612014286.
[2] N. Yoshida, H. Iwakiri, K. Tokunaga, T. Baba, Impact of low energy helium irradiation on plasma facing metals, J. Nucl. Mater. (2005) 946–950, doi:10.1016/j.jnucmat.2004.10.162.
[3] E.E. Bloom, F.W. Wiffen, The effects of large concentrations of helium on the mechanical properties of neutron-irradiated stainless steel, J. Nucl. Mater. 58 (1975) 171–184, doi:10.1016/0022-3115(75)90103-8.
[4] S. Das, Recent advances in characterising irradiation damage in tungsten for fusion power, SN Appl. Sci. 1 (2019) 1614, doi:10.1007/s42452-019-1591-0.
[5] S. Das, H. Yu, E. Tarleton, F. Hofmann, Hardening and Strain Localisation in Helium-Ion-Implanted Tungsten, Sci. Rep. 9 (2019) 1–14, doi:10.1038/s41598-019-54753-3.
[6] C.A. Taylor, J.D. Sugar, D.B. Robinson, N.C. Bartelt, R.B. Sills, K. Hattar, Using In Situ TEM Helium Implantation and Annealing to Study Cavity Nucleation and Growth, Jom 72 (2020) 2032–2041, doi:10.1007/s11837-020-04117-4.
[7] H. Trinkaus, B.N. Singh, Helium accumulation in metals during irradiation - Where do we stand? J. Nucl. Mater. (2003) 229–242, doi:10.1016/j.jnucmat.2003.09.001.
[8] K.D. Hammond, Helium, hydrogen, and fuzz in plasma-facing materials, Mater. Res. Express. 4 (2017) 104002, doi:10.1088/2053-1591/aa8c22.
[9] M.R. Gilbert, J.C. Sublet, Neutron-induced transmutation effects in W and W-alloys in a fusion environment, Nucl. Fusion. 51 (2011) 43005, doi:10.1088/0029-5515/51/4/043005.
[10] W D.S.E. Lassner, Tungsten: properties, chemistry, technology of the element, alloys, and chemical compounds, Springer US, New York, 2000, doi:10.5860/choice.37-2788.
[11] R.A. Pitts, S. Carpentier, F. Escourbiac, T. Hirai, V. Komarov, S. Lisgo, A.S. Kukushkin, A. Loarte, M. Merola, A. Sashala Naik, R. Mitteau, M. Sugihara, B. Bazylev, P.C. Stangeby, A full tungsten divertor for ITER: Physics issues and design status, J. Nucl. Mater. 438 (2013) S48–S56, doi:10.1016/j.jnucmat.2013.01.008.
[12] M. Shimada, B.J. Merrill, Tritium decay helium-3 effects in tungsten, Nucl. Mater. Energy. 12 (2017) 699–702, doi:10.1016/j.nme.2016.11.006.
[13] S. Wang, X. Zhu, L. Cheng, W. Guo, M. Liu, C. Xu, Y. Yuan, E. Fu, X.Z. Cao, G.H. Lu, Effect of heavy ion pre-irradiation on blistering and deuterium retention in tungsten exposed to high-fluence deuterium plasma, J. Nucl. Mater. 508 (2018) 395–402, doi:10.1016/j.jnucmat.2018.05.082.
[14] Y. Katoh, L.L. Snead, L.M. Garrison, X. Hu, T. Koyanagi, C.M. Parish, P.D. Edmondson, M. Fukuda, T. Hwang, T. Tanaka, A. Hasegawa, Response of unalloyed tungsten to mixed spectrum neutrons, J. Nucl. Mater. 520 (2019) 193–207, doi:10.1016/j.jnucmat.2019.03.045.
[15] H. Ullmaier, The influence of helium on the bulk properties of fusion reactor structural materials, Nucl. Fusion. 24 (1984) 1039–1083, doi:10.1088/0029-5515/24/8/009.

[16] S.B. Gilliam, S.M. Gidcumb, N.R. Parikh, D.G. Forsythe, B.K. Patnaik, J.D. Hunn, L.L. Snead, G.P. Lamaze, Retention and surface blistering of helium irradiated tungsten as a first wall material, J. Nucl. Mater. 347 (2005) 289–297, doi:10.1016/j.jnucmat.2005.08.017.

[17] P. Jenuš, A. Ivekovič, M. Kocen, A. Šestan, S. Novak, W 2 C-reinforced tungsten prepared using different precursors, Ceram. Int. 45 (2019) 7995–7999, doi:10.1016/j.ceramint.2018.11.187.

[18] S. Antusch, D.E.J. Armstrong, T. Ben Britton, L. Commin, J.S.K.L. Gibson, H. Greuner, J. Hoffmann, W. Knabl, G. Pintsuk, M. Rieth, S.G. Roberts, T. Weingaertner, Mechanical and microstructural investigations of tungsten and doped tungsten materials produced via powder injection molding, Nucl. Mater. Energy. 3-4 (2015) 22–31, doi:10.1016/j.nme.2015.04.002.

[19] X.Y. Tan, L.M. Luo, Z.L. Lu, G.N. Luo, X. Zan, J.G. Cheng, Y.C. Wu, Development of tungsten as plasma-facing materials by doping tantalum carbide nanoparticles, Powder Technol 269 (2015) 437–442, doi:10.1016/j.powtec.2014.09.039.

[20] G.M. Song, Y. Zhou, Y.J. Wang, The microstructure and elevated temperature strength of tungsten-titanium carbide composite, J. Mater. Sci. 37 (2002) 3541–3548, doi:10.1023/A:1016583611632.

[21] S. Novak, M. Kocen, A. Šestan Zavašnik, A. Galatanu, M. Galatanu, S. Tarancón, E. Tejado, J.Y. Pastor, P. Jenuš, Beneficial effects of a WC addition in FAST-densified tungsten, Mater. Sci. Eng. A. 772 (2020) 138666, doi:10.1016/j.msea.2019.138666.

[22] J.W. Coenen, S. Antusch, M. Aumann, W. Biel, J. Du, J. Engels, S. Heuer, A. Houben, T. Hoeschen, B. Jasper, F. Koch, J. Linke, A. Litnovsky, Y. Mao, R. Neu, G. Pintsuk, J. Riesch, M. Rasinski, J. Reiser, M. Rieth, A. Terra, B. Unterberg, T. Weber, T. Wegener, J.H. You, C. Linsmeier, Materials for DEMO and reactor applications - Boundary conditions and new concepts, Phys. Scr. 2016 (2016) 14002, doi:10.1088/0031-8949/2016/T167/014002.

[23] A. Šestan, J. Zavašnik, M.M. Kržmanc, M. Kocen, P. Jenuš, S. Novak, M. Čeh, G. Dehm, Tungsten carbide as a deoxidation agent for plasma-facing tungsten-based materials, J. Nucl. Mater. 524 (2019) 135–140, doi:10.1016/j.jnucmat.2019.06.030.

[24] M. Kelemen, A. Založnik, P. Vavpetič, M. Pečovnik, P. Pelicon, A. Hakola, A. Lahtinen, J. Karhunen, K. Piip, P. Paris, M. Laan, K. Krieger, M. Oberkofler, H. van der Meiden, S. Markelj, Micro-NRA and micro-3HIXE with 3He microbeam on samples exposed in ASDEX Upgrade and Pilot-PSI machines, Nucl. Instruments Methods Phys. Res. Sect. B Beam Interact. with Mater. Atoms. 404 (2017) 179–184 “www.srim.org. J. Ziegler”, www.srim.org, (n.d.), doi:10.1016/j.nimb.2017.01.072.

[26] C.A. Schneider, W.S. Rasband, K.W. Eliceiri, NIH Image to ImageJ: 25 years of image analysis, Nat. Methods. 9 (2012) 671–675, doi:10.1038/nmeth.2089.

[27] QGIS Development Team, QGIS Geographic Information System, Open Source Geospatial Foundation Project (2014) http://qgis.osgeo.org, Qgisorg http://www.qgis.org/.

[28] D.V. Suetin, I.R. Shein, A.L. Ivanovskii, Structural, electronic properties and stability of tungsten mono- and semi-carbides: A first principles investigation, J. Phys. Chem. Solids. 70 (2009) 64–71, doi:10.1016/j.jpcs.2008.09.004.

[29] G. Kresse, J. Hafner, Ab initio molecular dynamics for open-shell transition metals, Phys. Rev. B. 48 (1993) 13115–13118, doi:10.1103/PhysRevB.48.13115.

[30] G. Kresse, J. Furthmüller, Efficient iterative schemes for ab initio total-energy calculations using a plane-wave basis set, Phys. Rev. B - Condens. Matter Mater. Phys. 54 (1996) 11169–11186, doi:10.1103/PhysRevB.54.11169.

[31] P.E. Blöchl, Projector augmented-wave method, Phys. Rev. B. 50 (1994) 17953–17979, doi:10.1103/PhysRevB.50.17953.

[32] D. Joubert, From ultrasoft pseudopotentials to the projector augmented-wave method, Phys. Rev. B - Condens. Matter Mater. Phys. 59 (1999) 1758–1775, doi:10.1103/PhysRevB.59.1758.

[33] C.S. Becquart, C. Domain, Migration energy of He in W revisited by Ab initio calculations, Phys. Rev. Lett. 97 (2006) 196402, doi:10.1103/PhysRevLett.97.196402.

[34] J.P. Perdew, K. Burke, M. Ernzerhof, Generalized gradient approximation made simple, Phys. Rev. Lett. 77 (1996) 3865–3868, doi:10.1103/PhysRevLett.77.3865.

[35] H.J. Monkhorst, J.D. Pack, Special points for Brillouin-zone integrations, Phys. Rev. B. 13 (1976) 5188–5192, doi:10.1103/PhysRevB.13.5188.

[36] M. Methfessel, A.T. Paxton, High-precision sampling for Brillouin-zone integration in metals, Phys. Rev. B. 40 (1989) 3616–3621, doi:10.1103/PhysRevB.40.3616.

[37] G. Henkelman, B.P. Uberuaga, H. Jónsson, Climbing image nudged elastic band method for finding saddle points and minimum energy paths, J. Chem. Phys. 113 (2000) 9901–9904, doi:10.1063/1.1329672.

[38] G. Henkelman, H. Jónsson, Improved tangent estimate in the nudged elastic band method for finding minimum energy paths and saddle points, J. Chem. Phys. 113 (2000) 9978–9985, doi:10.1063/1.1323224.

[39] M Akmaliyah, 済無No Title No Title, J. Chem. Inf. Model. 53 (2013) 1689–1699.

[40] M. Cui, T. Shen, L. Pang, Y. Zhu, P. Jin, C. Liu, X. Fang, Z. Wang, He ion implantation induced He bubbles and hardness in tungsten, Nucl. Mater. Energy. 15 (2018) 232–236, doi:10.1016/j.nme.2018.05.004.

[41] P.E. Lhuillier, T. Belhabib, P. Desgardin, B. Courtois, T. Sauvage, M.F. Barthe, A.L. Thomann, P. Brault, Y. Tessier, Trapping and release of helium in tungsten, J. Nucl. Mater. 416 (2011) 13–17, doi:10.1016/j.jnucmat.2010.12.042.

[42] K.D. Rasch, R.W. Siegel, H. Schultz, Quenching and recovery investigations of vacancies in tungsten, Philos. Mag. A Phys. Condens. Matter, Struct. Defects Mech. Prop 41 (1980) 91–117, doi:10.1080/01418618008241833.

[43] V.N. Chernikov, J.V. Lakhotkin, H. Ullmaier, H. Trinkaus, P. Jung, H.J. Bierfeld, Helium-induced swelling in tungsten during postimplantation annealing, J. Nucl. Mater. 212-215 (1994) 375–381, doi:10.1016/0022-3115(94)90089-2.

[44] A. Debelle, M.F. Barthe, T. Sauvage, R. Belamhawal, A. Chelgoum, P. Desgardin, H. Labrim, Helium behaviour and vacancy defect distribution in helium implanted tungsten, J. Nucl. Mater. 362 (2007) 181–188, doi:10.1016/j.jnucmat.2007.01.021.

[45] A. De Backer, P.E. Lhuillier, C.S. Becquart, M.F. Barthe, Modelling of the implantation and the annealing stages of 800 keV 3He implanted tungsten: Formation of nanovoids in the near surface region, J. Nucl. Mater. 429 (2012) 78–91, doi:10.1016/j.jnucmat.2012.05.024.

[46] J.C. Russ, J.C. Russ, The Image Processing Handbook, CRC Press, 2002, doi:10.1201/9781420040760.

[47] J. Wang, D. Liu, W. Dang, Z. Guo, W. Song, Segregation and coalescence behavior of helium bubbles in tungsten, J. Nucl. Mater. 544 (2021) 152732, doi:10.1016/j.jnucmat.2020.152732.

[48] X.Y. Liu, B.P. Uberuaga, D. Perez, A.F. Voter, New helium bubble growth mode at a symmetric grain-boundary in tungsten: Accelerated molecular dynamics study, Mater. Res. Lett. 6 (2018) 522–530, doi:10.1080/21663831.2018.1494637.

[49] A. Atkinson, Grain-boundary diffusion: An historical perspective, J. Chem. Soc. Faraday Trans. 86 (1990) 1307–1310, doi:10.1039/FT9908601307.

[50] H.B. Zhou, Y.H. Li, G.H. Lu, Modeling and simulation of helium behavior in tungsten: A first-principles investigation, Comput. Mater. Sci. 112 (2016) 487–491, doi:10.1016/j.commatsci.2015.09.019.

[51] H.B. Zhou, Y.L. Liu, S. Jin, Y. Zhang, G.N. Luo, G.H. Lu, Towards suppressing H blistering by investigating the physical origin of the H-He interaction in W, Nucl. Fusion. 50 (2010) 115010, doi:10.1088/0029-5515/50/11/115010.

[52] X.C. Li, X. Shu, Y.N. Liu, Y. Yu, F. Gao, G.H. Lu, Analytical W-He and H-He interatomic potentials for a W-H-He system, J. Nucl. Mater. 426 (2012) 31–37, doi:10.1016/j.jnucmat.2012.03.039.

[53] J. Amano, D.N. Seidman, Diffusivity of 3He atoms in perfect tungsten crystals, J. Appl. Phys. 56 (1984) 983–992, doi:10.1063/1.334039.

[54] A. Wagner, D.N. Seidman, Range profiles of 300- and 475-eV He+4 ions and the diffusivity of He4 in tungsten, Phys. Rev. Lett. 42 (1979) 515–518, doi:10.1103/PhysRevLett.42.515.

[55] J. Wang, Y. Zhang, H.B. Zhou, S. Jin, G.H. Lu, First-principles investigation of helium dissolution and clustering at a tungsten (1 1 0) surface, J. Nucl. Mater. 461 (2015) 230–235, doi:10.1016/j.jnucmat.2015.03.026.

[56] C.S. Becquart, C. Domain, An object Kinetic Monte Carlo Simulation of the dynamics of helium and point defects in tungsten, J. Nucl. Mater. 385 (2009) 223–227, doi:10.1016/j.jnucmat.2008.11.027.

Supplementary information file

Non-uniform He bubble formation in W/W_2C composite: Experimental and *ab-initio* study

Andreja Šestan[1,2,3], Lekshmi Sreekala[2], Sabina Markelj[1], Mitja Kelemen[1], Janez Zavašnik[1,2], Christian H. Liebscher[2], Gerhard Dehm[2], Tilmann Hickel[2,4], Miran Čeh [1,3], Saša Novak[1,3], Petra Jenuš[1]

[1]Jožef Stefan Institute, Jamova c. 39, 1000 Ljubljana, Slovenia
[2]Max-Planck-Institut für Eisenforschung, Max-Planck-Straße 1, 40237 Düsseldorf, Germany
[3]Jožef Stefan International Postgraduate School, Jamova c. 39, 1000 Ljubljana, Slovenia
[4]Federal Institute for Materials Research and Testing (BAM), Richard-Willstätter-Straße 11, 12489 Berlin, Germany

Introduction

This Supplementary information file consists of intermediate results, calculations, and extended explanation of either experimental analyses, data manipulation, or presentations. The information presented here is supporting the main findings and conclusions of the manuscript.

Content of this file:

Supplementary information file

1. Chemical composition of the starting powders

Table S1: Chemical composition as declared by the manufacturers for tungsten (W, MPO7R; Global Tungsten & Powder, USA), and tungsten carbide powders (WC, Sigma-Aldrich, USA).

W		WC	
impurity	ppm	impurity	ppm
O	1050	V	26
Al	< 10	Al	60
Ca	1	Ca	1
Co	< 1	Co	26
Cr	2	Cr	3885
Cu	1	Cu	0.5
Fe	2	Fe	29
K	2	K	1.1
Mg	< 1	Mg	4
Mn	2	Mn	3.3
Mo	9	Mo	0.5
Na	2	Na	3.2
Ni	3	Ni	1.1
Pb	< 5	Pb	1.2
S	1	Ti	0.3
		Zr	1.6

2. Calculated structure parameters for W and W_2C.

Table S2: Calculated structure parameters for bcc W and ε-W_2C. Previous experimental and theoretical results are listed for comparison.

System	Method	Lattice parameters (Å)		
		a	b	c
W	Present work	3.184	3.184	3.184
	Other DFT works	3.174^{a}, 3.171^{b}	3.174^{a}, 3.171^{b}	3.174^{a}, 3.171^{b}
	Expt.	3.165^{c}	3.165^{c}	3.165^{c}
W_2C	Present work	5.249	5.249	4.773
	Other DFT works	5.253^{d},5.357^{e}	5.253^{d},5.357^{e}	4.772^{d},4.706^{e}
	Expt.	5.184^{f}	5.184^{f}	4.721^{f}

^{a}[1] (energy cut off = 350 eV), ^{b} Ref.[2] (energy cut off = 400 eV), ^{c} Ref.[3], ^{d} Ref.[4], ^{e} Ref.[5], ^{f} Ref.[6]

Supplementary information file

3. Optical investigations of the samples after the He implantation experiments

For the characterisation of the samples after the implantation experiments, an optical microscope (OM, Zeiss Imager.Z1m, Zeiss GmbH) in reflective mode was used. The colour variation of the surface was a clear indication of the irradiated zone, hence allowing the manufacturing of the FIB cross-section wells in the representative locations, marked on Fig. . The surface contamination is originated from the residual carbon in the vacuum chamber being deposited by action of high energy ion beam, during long exposure times. At this point, we speculated that the brownish surface coloration of the irradiated zone is only superficial.

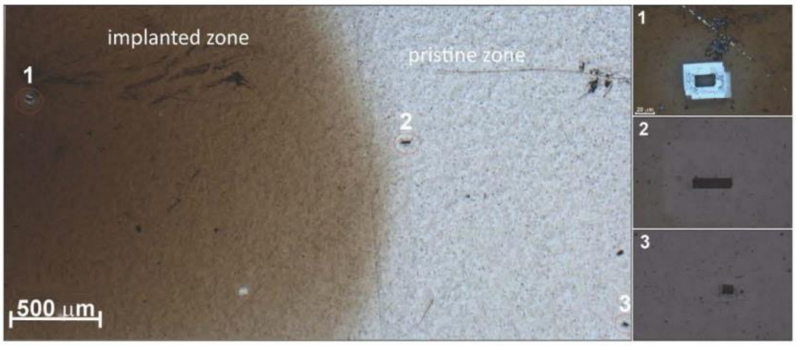

Fig. S1: (1) Optical microscopy of the interface between irradiated (left) and pristine (right) sample surface after the He-irradiation experiment, before annealing. The markings (1, 2, 3) are of FIB cross-section positions.

4. Electron microscopy of the He-irradiated samples

After the implantation experiment, several FIB cross-sections were made in and outside the implantation zone, marked on Fig. , to assess the effect of He implantation on the sample. First, the edge-region was investigated (marked #2 on Fig.), to determine the reason for the dark coloration or the implantation zone. As is turns out, the coloration observed by OM is due to the surface carbon contamination, most probably due to surface contamination by hydrocarbons. The observations of the material in the cross-sections, made in the edge of implantation zone, showed no surface contamination effect on the underlying microstructure (Fig. S1).

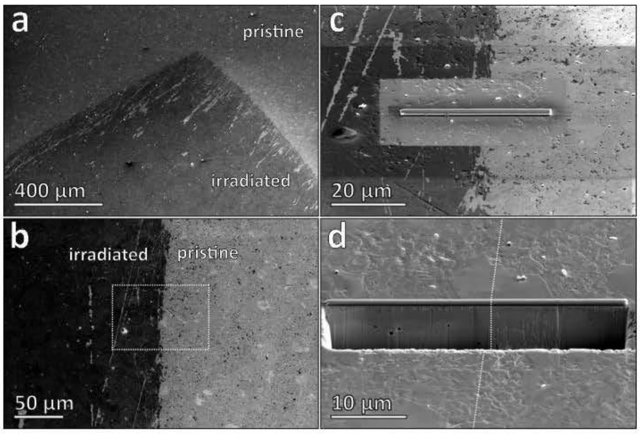

Fig. S1: (a) SE-SEM micrograph of the contact between implanted and pristine sample (marked #2 on Fig.). (b) Sharp interface between implanted and pristine W surface. The difference in contrast is due thin surface carbon contamination present on the implantedd surface. Dotted square marks the region in (c), where the thin surface carbon contamination is removed even by electrons used for SEM image formation, and (d) even more when bombarding the surface by Ga+ ions during FIB ion milling. In the cross-section, no structural differences could be observed between irradiated and shielded, pristine sample. Dotted white line marks the original interface between irradiated and pristine sample.

On the micrographs recorded in the cross-sections, the most prominent feature is the variation of the image contrast as a result of electron channelling, originating in the high-energy fraction of the backscattered electrons. Here, the secondary electron images were acquired with Everhart–Thornley Detector (EDT), sensitive for the low-energy (< 50 eV) electrons. Still, one needs to stress that besides SEs and low-energy BSE, also high-energy BSEs are collected[7].

In the cross-sections in the central implantation zone (marked #1 on **Error! Reference source not found.**), additional contrast enhancement inside the single W grains was observed in the first few µm below the sample surface (Fig. S2(a, b)). Such feature was observed only inside implantation zone, while in the non-irradiated regions the contrast inside W grains appear uniform (marked #3 on Fig. e.g. Fig. S2(c, d)). As the thickness of the contrast variation zone coincided with the SRIM simulation prediction for the peak damage distribution depth, we speculated that it can be an effect of W crystal structure damage induced by He implantation.

Supplementary information file

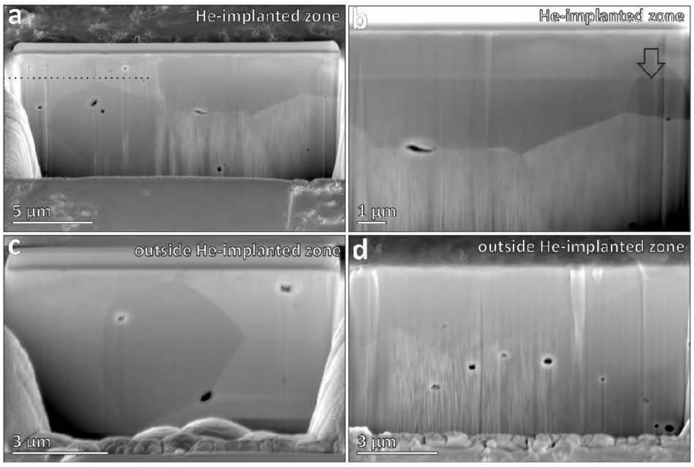

Fig. S2: (a, b) FIB cross-section made inside the implantation zone (position 1), showing the enhancement of the contrast inside single W grains, which corresponds to the He implantation depth. In contrast, the cross-section made outside the implantation zone, such as (c) on position 3, show no contrast variation. (d) The electron channelling contrast is uniform everywhere outside the main implantation zone.

As the FIB cross-section were made before and after the annealing of the sample, it was possible to track the microstructure evolution at the identical location. The sample was annealed at 1873K for 20 minutes, and again investigated in SEM. With the help of the OM map, the identical locations were found, and the FIB cross-section trenches were re-polished to remove the Pt contamination and surface morphology due to grain boundary grooving (Fig. S3). The initial observed variation of the contrast inside single W grain after the He implantation coincides with the formation of the He bubbles distribution network after the annealing.

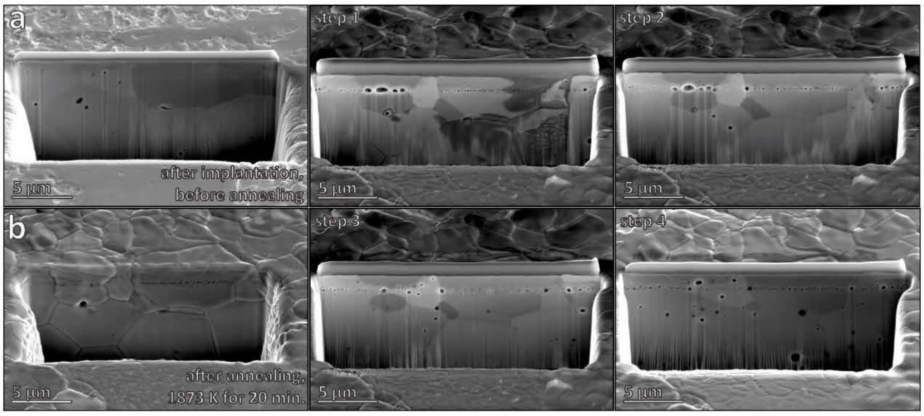

Fig. S3: a) FIB cross-section after implantation, before annealing. (b) Same cross-section location after annealing for 20 minutes at 1873K, showing recovery of the grains on the surface; note the complete removal of the protective Pt deposit. The cross-section was re-polished in several steps (1-4) until satisfactory surface quality was achieved.

5. Simulation of the electron penetration into the bulk W and W_2C

Penetration of electrons in W and W_2C as a function of accelerating voltage used for generation of primary electron beam in SEM is comparably shallow, is only about 60 nm at 5kV, 200 nm at 15 kV, 400 nm at 20 kV, 600 nm at 25 kV and 800 nm at 30 kV.

These penetration depths estimations are used for the interpretation of the SEM and EBSD results, and in the process of surface quality inspection during the sample preparation.

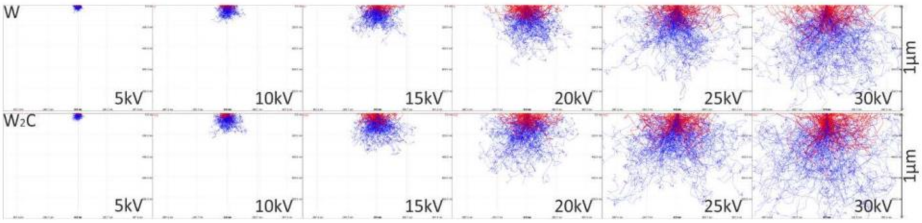

Fig. S4: Electron penetration depth in pure W and W_2C bulk as a function of accelerating voltage, blue lines: secondary electrons, red lines: backscattered electrons. Simulated made with Casino v2.51 software [8].

6. EBSD analysis of the initial composite microstructure

From the low and large-area EBSD maps (mag. ×500 and ×2000), a grain size distribution histogram was calculated (Fig.). For W, 906 grains were considered (Fig. S6(a)), and for W_2C 248 grains were identified, analysed and recalculated (Fig. S6(b)). Scanning electron microscopy (SEM) was performed with a JEOL JSM 6500-F microscope (JEOL, Tokyo, Japan), and JEOL JSM 7600-F microscope (JEOL, Tokyo, Japan) equipped with an electron backscattered diffraction (EBSD) detector Nordlys II (Oxford Instruments, Abingdon, UK). Data processing and analysis were performed with the Channel 5™ (HKL Technology, Inc.).

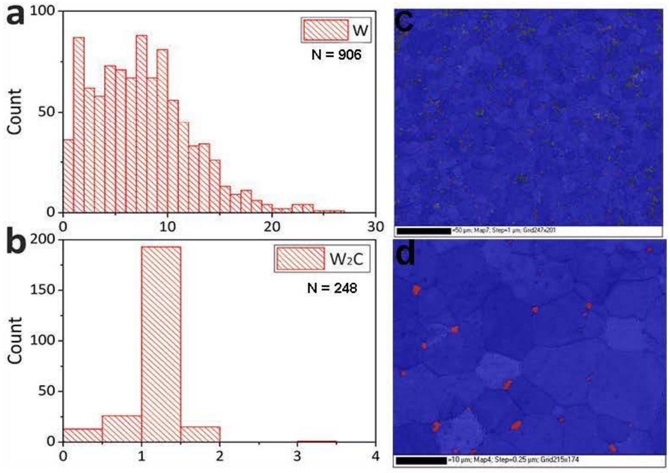

Fig. S5: Grain size distribution histogram for (a) W (N=906) and (b) W_2C (N=248) composite. Colour map of the W (blue (c and d)) and W_2C (red (c and d)) crystal grains at large-area (c) and small area (b) scan.

7. Setting the region of interest (ROI) for micro-to-nano scale hierarchical investigation

The thin foils for TEM were prepared by FIB. As the size of such prepared samples is only several microns, we first have to determine the region of interest for a site-specific FIB lift-out technique for subsequent TEM analyses. We combined SEM and EBSD techniques, and the details of the specimen preparation are summarised as follows. First, the implanted bulk sample was cut in half by a diamond wire saw, approx. at the middle of the implantation zone (Fig. S6(a)). In the next step, both halves were bonded face-to-face by epoxy resin, exposing the implantation zone in cross-section (Fig. S6(b)). The sandwiched sample was prepared by standard metallographic procedures described in[8]. After polishing and surface treatment, the implantation zone was determined by SEM (Auriga Crossbeam, Carl Zeiss Microscopy) (Fig. S6(c)). The phase composition (W and W_2C) and their spatial distribution in the implantation zone were assessed by electron-backscatter diffraction (EBSD; TEAM EBSD, Hikari Super, OIM Analysis software, EDAX AMETEK) (Fig. S6(d)). All SEM experiments were conducted at an accelerating voltage of 20 kV, and during the image post-processing, data with a confidence index lower than 0.1 were omitted.

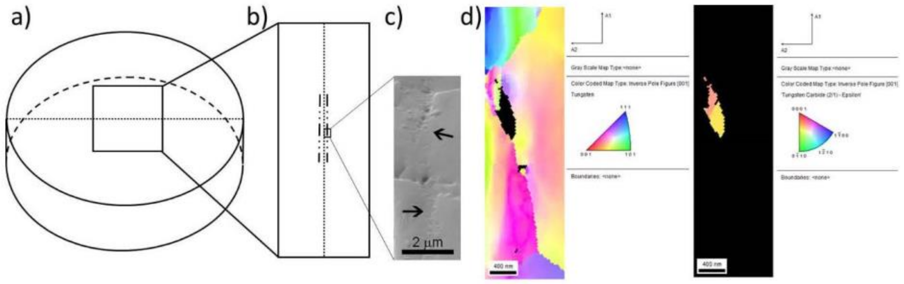

Fig. S6: (a, b) Bulk sample formatting and cross-section preparation. (c, d) SEM and EBSD analyses before the FIB thin foil preparation. SEM image of post-annealed He-implanted sample, with the bubble region marked with arrows with the corresponding EBSD phase-map composition. The indexation is for W (left) and W_2C (right).

After locating the intersection of all three features of interest, namely the grain boundary between both phases (W and W_2C) and the implantation zone, a thin electron transparent foil by FIB was prepared (Fig. S7). As the focus of the TEM lamella was to observe the interface between both phases, the lamella was positioned at an angle of 70° regarding the implantation zone. Hence, the angle correction must be implemented to calculate the depth of the He bubble zone in the TEM lamella.

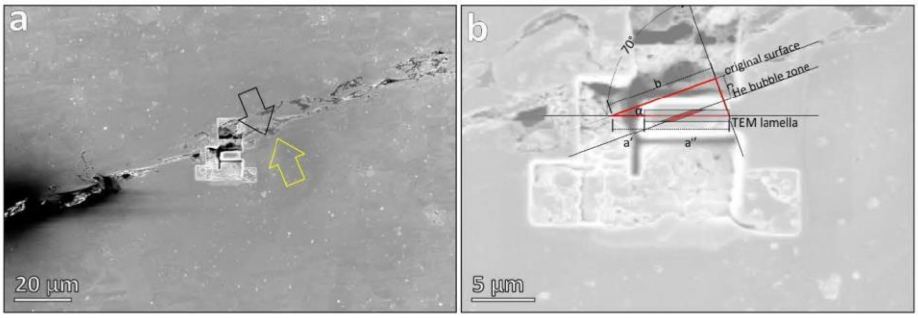

Fig. S7: (a) SEM micrograph of the intermediate step of TEM lamella FIB lift-out; yellow arrow point on the He bubble zone, and black arrow marks the original sample surface. (b) Schematics of the relationship between original sample surface, He bubble zone, and TEM lamella, with marked parameters for the angular corrections calculations.

The implantation depth, corrected for the tilt angle, was calculated using the following parameters measured from the (Fig. S7): α = 20 °, a' = 1.16 µm, and a" = 4.5 µm. From the TEM micrograph in Fig. 4(c) in the main article file, the top of He bubble region was measured as a_1" = 1.8 µm and the bottom of implantation region as a_2" = 3.7 µm. It is noted that to all measured distances, corrected for a tilt angle, a value of a_{corr}' (missing distance to the original surface, corrected for tilt angle) has to be added.

$$a'_{corr} = \sin(20) \times a' = 0.3967\ \mu m$$

$$a_{corr}'' = \sin(20) \times a'' = 1.5391\ \mu m$$

$$a_1'' = \sin(20) \times 1.8\ \mu m = 0.6156\ \mu m$$

$$a_2'' = \sin(20) \times 3.7\ \mu m = 1.2655\ \mu m$$

$$a''_1 + a''_1 = 0.6156\ \mu m + 0.3967\ \mu m = 1.0123\ \mu m$$

$$a''_2 + a''_1 = 1.2655\ \mu m + 0.3967\ \mu m = 1.6622\ \mu m$$

Therefore, the He bubble region on TEM lamella is observed between 1.0 µm and 1.6 µm, which is in good agreement with the SRIM calculation.

8. TEM analysis of W and W_2C grains

The investigation of the microstructure evolution, crystal structure and defects of annealed He-implanted sample was conducted by 200 kV transmission electron microscope (JEM-2100, Jeol Inc.) using analytical double-tilt Be holder. For each grain, the sample was tilted around α and β axis to the low-index zone axis (ZA). When in appropriate position, a selected-area aperture was used to record the diffraction pattern, which was indexed regarding the reference crystal structures and lattice parameters for W [9], and W_2C [10] (Fig. S8, second column).

The TEM micrograph of the grain was first recorded in bright-field mode (BF-TEM), where aperture is placed over the central diffraction spot, hence only directly transmitted electrons contribute to the image contrast while diffracted electrons are cut-off by the aperture (Fig. S8, first column). The set of two different diffractions was used for generation of off-axis dark-field micrographs, presented in the following columns, with marked corresponding *g*-vectors.

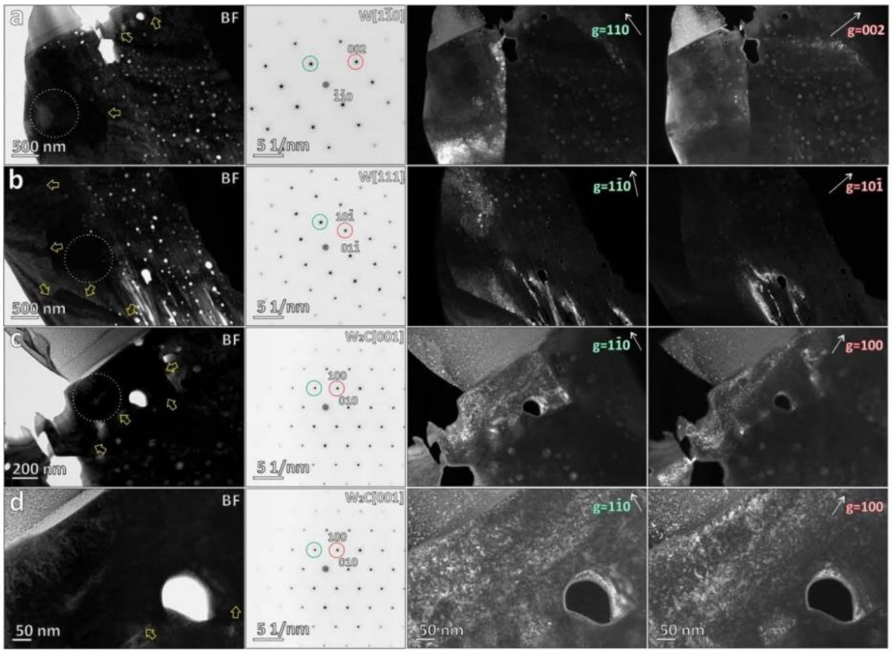

Fig. S8: Overview TEM micrographs recorded over (a, b) W grains, (c) W - W_2C grains contact, and (d) over the W_2C grain. Table present in the first column an overview BF-TEM micrograph, with yellow arrows marking the grain boundaries. The white dotted circle marks the region where an SAED patterns were recorded over the investigated grains and are presented in the second column (inverted). The diffraction spots are indexed for W and W_2C, using reference structure data. Green and red circles denote the aperture position used for DF-TEM micrographs, presented in the following two columns.

9. Construction of Voronoi diagram, polygons and cells

TEM micrographs were processed by QGIS software package [11]. Voronoi diagram was used for partitioning of a plane into regions close to each of a given set of objects. We considered the analysed lamella as a finite Euclidean plane, where bubbles represent a given set of points (p_k). With a finite set of points $\{p_1, ..., p_n, n = 615\}$, we partitioned the plane into regions in which the generating point of each cell is also its centroid, and each cell comprises of all points where the distance to p_k is ≤ to its distance to any other p_k (centroidal Voronoi tessellation).

The process of experimental TEM micrograph analysis is summarised in Fig. S9. Starting with the HAADF-STEM micrograph in Fig. S9(a), all the features identified in the image were vectorised Fig. S9(b). In the next step, the centroid was set in the geometrical centre of each void (Fig. S9(c), grey dots); the area of the void was calculated and set as an attribute to each centroid. Following, the centroids were connected following the Delaunay triangulation (Fig. S9(d)). As the Voronoi diagram of a set of points is dual to its Delaunay triangulation, in the final step, the Voronoi cells were constructed (Fig. S9(e)), and with overlaid voids (Fig. S9(f)) show an interplay between structure defects and voids position.

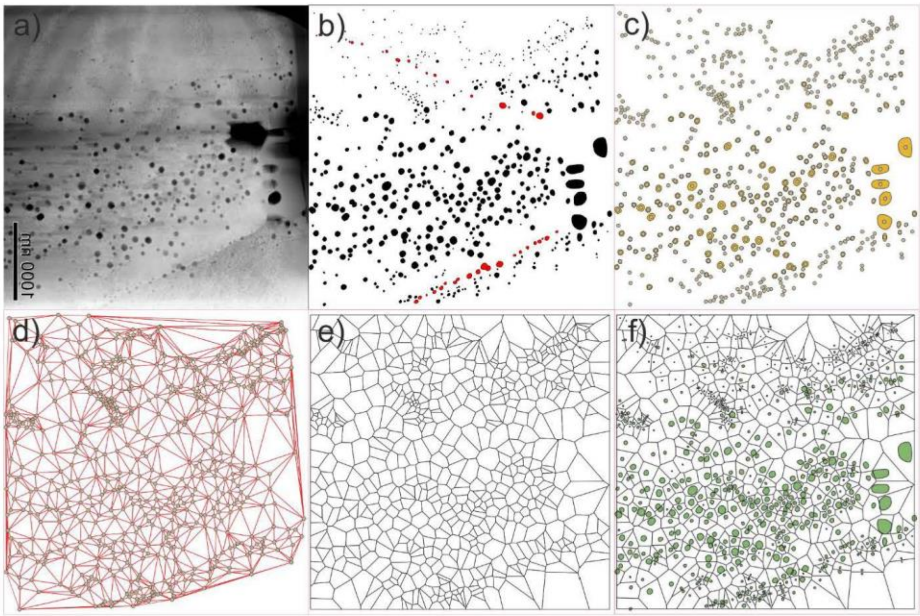

Fig. S9: Starting image, intermediate treatment and the results of the processing of the TEM images.

10. Construction of Kernel Density Estimation (KDE) maps

TEM micrographs were processed by QGIS software package [11]. Kernel density estimation (KDE) is a statistical non-parametric method for estimating the probability density function of a random variable, where data smoothing, based on a finite data sample, is needed due to inferences with the population.

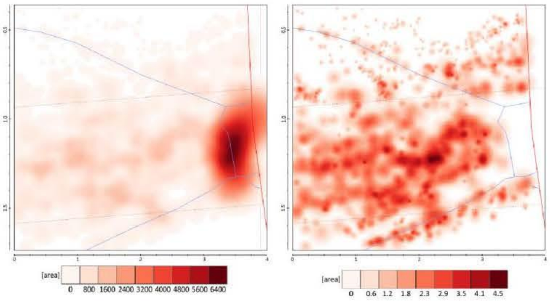

Fig. S10: KDE heatmap considering all voids, using their size as attribute (left), and KDE heatmap without the voids developed on the phase boundary, only in W (right). The area heatmap is constructed in px, where 1 px = 1.56 nm.

11. Calculated vacancy formation energies for W and W_2C.

Table S3: Calculated vacancy formation energies of W and C sites.

Vacancy formation energy (eV)			
W	W_2C		
W vac	W vac	C vac-1	C vac-2
3.26	1.54	2.16	2.27

12. Voronoi volume of different sites in W and W_2C

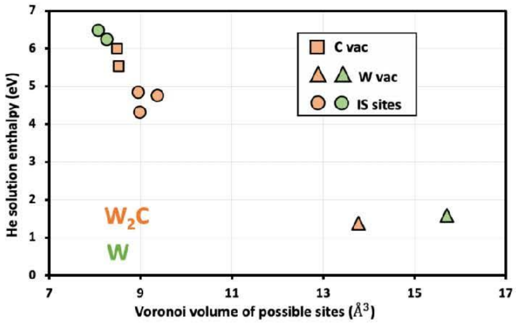

Fig. S11: The correlation between Voronoi volume of different sites in W (green) and W_2C (orange) and corresponding solution enthalpies are plotted.

13. Binding energy of He-He in W and W$_2$C carbide

Table S4: Binding energy of He-He in W and W$_2$C carbide (in eV) with the final distance between them are given. The calculations were done using a 54 atom supercell for W and 72 and 108 atoms supercells of W$_2$C with He atoms in the interstitial sites according to the distance between them. Other possible arrangements of He-He interactions are given in [1].

He$_1$ for interaction energy	He-He final atoms (Å)	Binding energy(eV)
W		
TIS	1.50 (TIS)	0.97
W$_2$C		
IS-1	1.47 (IS-1)	0.760
	2.44 (IS-2)	0.104
	3.79 (IS-3)	0.030
IS-2	1.55 (IS-3)	1.154
	1.56 (IS-2)	1.060
	2.44 (IS-1)	0.104
	4.19 (IS-1) (2x3x2 cell)	-0.028

14. References

[1] C.S. Becquart, C. Domain, Migration energy of He in W revisited by Ab initio calculations, Phys. Rev. Lett. 97 (2006) 196402. https://doi.org/10.1103/PhysRevLett.97.196402.

[2] S.C. Lee, J.H. Choi, J.G. Lee, Energetics of He and H atoms with vacancies in tungsten: First-principles approach, J. Nucl. Mater. 383 (2009) 244–246. https://doi.org/10.1016/j.jnucmat.2008.09.017.

[3] P.E. Tomaszewski, Structural phase transitions in crystals I. database, Phase Transitions. 38 (1992) 127–220. https://doi.org/10.1080/01411599208222899.

[4] A.S. Kurlov, A.I. Gusev, Phase equilibria in the W–C system and tungsten carbides, Russ. Chem. Rev. 75 (2006) 617–636. https://doi.org/10.1070/rc2006v075n07abeh003606.

[5] F.Z. Abderrahim, H.I. Faraoun, T. Ouahrani, Structure, bonding and stability of semi-carbides M 2C and sub-carbides M 4C (M=V, Cr, Nb, Mo, Ta, W): A first principles investigation, Phys. B Condens. Matter. 407 (2012) 3833–3838. https://doi.org/10.1016/j.physb.2012.05.070.

[6] M.F. Morks, Y. Gao, N.F. Fahim, F.U. Yingqing, Microstructure and hardness properties of cermet coating sprayed by low power plasma, Mater. Lett. 60 (2006) 1049–1053. https://doi.org/10.1016/j.matlet.2005.10.073.

[7] J.R.M. Joseph Goldstein, Dale E. Newbury, David C. Joy, Charles E. Lyman, Patrick Echlin, Eric Lifshin, Linda Sawyer, Scanning Electron Microscopy and X-ray Microanalysis: Third Edition, Springer US, 2012. https://doi.org/10.1007/978-1-4615-0215-9.

[8] A. Šestan, J. Zavašnik, M.M. Kržmanc, M. Kocen, P. Jenuš, S. Novak, M. Čeh, G. Dehm, Tungsten carbide as a deoxidation agent for plasma-facing tungsten-based materials, J. Nucl. Mater. 524 (2019) 135–140. https://doi.org/10.1016/j.jnucmat.2019.06.030.

[9] H.E. Swanson, E. Tatge, Standard X-ray diffraction powder patterns. National Bureau of Standards (US), Circular. (1953) 62.

[10] Y. Li, Y. Gao, B. Xiao, T. Min, Z. Fan, S. Ma, L. Xu, Theoretical study on the stability, elasticity, hardness and electronic structures of W-C binary compounds, J. Alloys Compd. 502 (2010) 28–37. https://doi.org/10.1016/j.jallcom.2010.04.184.

[11] QGIS Development Team, QGIS Geographic Information System. Open Source Geospatial Foundation Project. http://qgis.osgeo.org, Qgisorg. (2014). http://www.qgis.org/.

Chapter 5

Conclusions

In the scope of the thesis, I investigated three main research topics with one common point: the material microstructure relation to macroscopic physical properties, such as structural integrity and behaviour at elevated temperatures or He irradiation. The benchmarking material for the research was W, and W/W_2C composite developed and proposed for fusion applications by a Slovenian research group within the European Fusion Programme (K7 – JSI). The results obtained during the research contribute to the fundamental understanding of W and W/W_2C materials properties and advance the development of metal-ceramic composite materials with adequate physical properties intended for fusion applications.

The most time-consuming part of the thesis was the development of the sample preparation protocols for microstructural analysis of tungsten and tungsten-based composites. The obtained clean and pristine surface allowed the implementation of research methods to provide reliable and reproducible results with high accuracy and statistical significance to evaluate their macroscopic properties and interlink them with the macroscopic physical properties required for successful PFMs applications.

The W and W/W_2C materials used in this research were produced by unconventional, field-assisted sintering technique (FAST). The initial materials exhibit some drawbacks, such as the formation of the carbide shell formed on the contact with the graphite tool, identified as a mixture of tungsten and tungsten carbide, which implies the necessary metalworking of the consolidated samples before use. The investigation of the samples also revealed the formation of oxygen-rich W phases along the GBs, identified as monoclinic WO_2 (SG: $P2_1/c$). As the thermal stability of the oxide phase is below the operation window of intended use, the presence of oxides should be prevented in the final material. A direct carburisation process by carbon-rich tungsten compounds (WC) was explored and successfully applied to reduce the in-situ tungsten-oxide formation. The optimum theoretical amount of WC introduced in the initial powder mixture to prevent the *in-situ* formation of WO_2 was determined by thermodynamic and kinetic calculations. A surplus amount of WC leads to a thermally stable ε-W_2C (SG: $P\bar{3}1m$) secondary phase. From the binary W-C phase diagram (Figure 1), one can see that the eutectic reaction will occur at 2988 K (L ↔ W + β-W_2C), which is much lower than the melting point of W (~3695 K). This eutectic composition is expected to form at W/W_2C interfaces, leading to an increase in homologous temperature and enhanced diffusion at the interfaces. Moreover, at 1923 K, a disordered-ordered transformation reaction occurs (W + β-W_2C↔ W + ε-W_2C). We can assume that it will remain thermally stable once the ε-W_2C phase is formed.

After the material optimization, we explored the behaviour of the W/W_2C composite material under He irradiation as a proxy for the exposure to running plasma. The implantation of ^{4}He into W/W_2C at room temperature, with subsequent annealing, was performed to study the He bubble evolution as a function of a given He content. After post-implantation high-temperature annealing at 1873 K, we observe a formation of the He bubbles at a depth of ~1.2 µm under the surface. The sub-surface region with damaged crystal structure can be identified already in cross-section SEM from the variation of the backscattered electron channelling contrast. The detailed TEM analysis of the as-implanted and post-annealed sample shows bubbles throughout the sample, but surprisingly not in the W_2C grain. These experimental observations were the motivation for theoretical calculations, which show that He will be primarily incorporated into interstitial sites in both phases, W and W_2C. Still, a single He atom is not sufficient for the nucleation of a bubble due to the large surface energy connected to the decohesion process. To lower its solution enthalpy, an alternative mechanism for W and W_2C is proposed by helium atoms clustering. Spherical clusters of up to five He atoms can form in W and are extremely hard to dissociate. In the case of W_2C, clusters of four He atoms or less can form in chain-like configurations, reducing the solution enthalpies again to lower values than in W. Furthermore, experimental results confirmed by DFT calculation show He ability to form helium bubbles in the W grain interior but not within the W_2C grain. On these premises, we can rationalise that phase boundaries will act as trapping sites for helium; still, the lack of bubble partitioning at the interface can restrict the applications of such materials as PFMs.

References

[1] J. W. Coenen *et al.*, "Materials for DEMO and reactor applications - Boundary conditions and new concepts," *Phys Scr*, vol. 2016, no. T167, p. 14002, 2016, doi: 10.1088/0031-8949/2016/T167/014002.

[2] J. W. Coenen *et al.*, "Materials for DEMO and reactor applications - Boundary conditions and new concepts," in *Physica Scripta*, Jan. 2016, vol. 2016, no. T167, p. 014002. doi: 10.1088/0031-8949/2016/T167/014002.

[3] Y. Ueda *et al.*, "Baseline high heat flux and plasma facing materials for fusion," *Nuclear Fusion*, vol. 57, no. 9, p. 92006, 2017, doi: 10.1088/1741-4326/aa6b60.

[4] H. Bolt *et al.*, "Materials for the plasma-facing components of fusion reactors," *Journal of Nuclear Materials*, vol. 329–333, no. 1-3 PART A, pp. 66–73, Aug. 2004, doi: 10.1016/J.JNUCMAT.2004.04.005.

[5] R. A. Pitts *et al.*, "A full tungsten divertor for ITER: Physics issues and design status," *Journal of Nuclear Materials*, vol. 438, no. SUPPL, p. Supplement: p. S48-S56., 2013, doi: 10.1016/j.jnucmat.2013.01.008.

[6] H. Bolt *et al.*, "Materials for the plasma-facing components of fusion reactors," *Journal of Nuclear Materials*, vol. 329–333, no. 1-3 PART A, pp. 66–73, Aug. 2004, doi: 10.1016/J.JNUCMAT.2004.04.005.

[7] Y. Sakoi, M. Miyamoto, K. Ono, and M. Sakamoto, "Helium irradiation effects on deuterium retention in tungsten," *Journal of Nuclear Materials*, vol. 442, no. 1–3, pp. S715–S718, Nov. 2013, doi: 10.1016/J.JNUCMAT.2012.10.003.

[8] W.-D. S. E. Lassner, *Tungsten: properties, chemistry, technology of the element, alloys, and chemical compounds*, vol. 37, no. 05. New York: Springer US, 2000. doi: 10.5860/choice.37-2788.

[9] J. Fan *et al.*, "Micro/nano composited tungsten material and its high thermal loading behavior," *JNuM*, vol. 455, no. 1–3, pp. 717–723, 2014, doi: 10.1016/J.JNUCMAT.2014.09.037.

[10] G. M. Kalinin, "High-Z plasma-facing and related materials," *Journal of Nuclear Materials*, vol. 179–181, no. PART 2, pp. 1193–1198, 1991, doi: 10.1016/0022-3115(91)90320-7.

[11] M. Rieth *et al.*, "Tungsten as a Structural Divertor Material," *Advances in Science and Technology*, vol. 73, pp. 11–21, Oct. 2010, doi: 10.4028/WWW.SCIENTIFIC.NET/AST.73.11.

[12] G. Kalinin *et al.*, "ITER R&D: Vacuum Vessel and In-vessel Components: Materials Development and Test," *Fusion Engineering and Design*, vol. 55, no. 2–3, pp. 231–246, 2001.

[13] S. Antusch *et al.*, “Mechanical and microstructural investigations of tungsten and doped tungsten materials produced via powder injection molding,” *Nuclear Materials and Energy*, vol. 3–4, pp. 22–31, 2015, doi: 10.1016/j.nme.2015.04.002.

[14] M. R. Gilbert and J. C. Sublet, “Neutron-induced transmutation effects in W and W-alloys in a fusion environment,” *Nuclear Fusion*, vol. 51, no. 4, p. 43005, Apr. 2011, doi: 10.1088/0029-5515/51/4/043005.

[15] M. Shimada and B. J. Merrill, “Tritium decay helium-3 effects in tungsten,” *Nuclear Materials and Energy*, vol. 12, pp. 699–702, 2017, doi: 10.1016/j.nme.2016.11.006.

[16] H. Ullmaier, “The influence of helium on the bulk properties of fusion reactor structural materials,” *Nuclear Fusion*, vol. 24, no. 8, pp. 1039–1083, 1984, doi: 10.1088/0029-5515/24/8/009.

[17] S. Wang *et al.*, “Effect of heavy ion pre-irradiation on blistering and deuterium retention in tungsten exposed to high-fluence deuterium plasma,” *Journal of Nuclear Materials*, vol. 508, pp. 395–402, Sep. 2018, doi: 10.1016/j.jnucmat.2018.05.082.

[18] Y. Katoh *et al.*, “Response of unalloyed tungsten to mixed spectrum neutrons,” *Journal of Nuclear Materials*, vol. 520, pp. 193–207, Jul. 2019, doi: 10.1016/j.jnucmat.2019.03.045.

[19] Z. X. Tian, W. Xiao, F. R. Wan, and W. T. Geng, “Binary effect of He and H on the intra- and inter-granular embrittlement in Fe,” *Journal of Nuclear Materials*, vol. 407, no. 3, pp. 200–204, 2010, doi: 10.1016/j.jnucmat.2010.10.016.

[20] S. B. Gilliam *et al.*, “Retention and surface blistering of helium irradiated tungsten as a first wall material,” *Journal of Nuclear Materials*, vol. 347, no. 3, pp. 289–297, 2005, doi: https://doi.org/10.1016/j.jnucmat.2005.08.017.

[21] L. H. Rumbaugh, R. B. Roberts, and L. R. Hafstad, “Nuclear transmutations of the lithium isotopes,” *Physical Review*, vol. 54, no. 9, pp. 657–680, 1938, doi: 10.1103/PhysRev.54.657.

[22] K. O. E. Henriksson, K. Nordlund, A. Krasheninnikov, and J. Keinonen, “The depths of hydrogen and helium bubbles in tungsten: A comparison,” *Fusion Science and Technology*, vol. 50, no. 1, pp. 43–57, 2006, doi: 10.13182/FST06-A1219.

[23] F. Sefta, K. D. Hammond, N. Juslin, and B. D. Wirth, “Tungsten surface evolution by helium bubble nucleation, growth and rupture,” *Nuclear Fusion*, vol. 53, no. 7, p. 73015, 2013, doi: 10.1088/0029-5515/53/7/073015.

[24] T. J. Dolan and A. Parrish, *Introduction*, vol. 19. Springer, London, 2013. doi: 10.1007/978-1-4471-5556-0_1.

[25] J. R. Stephens, “Effects of interstitial impurities on the low-temperature tensile properties of tungsten,” 1964. Accessed: Dec. 13, 2021. [Online]. Available: https://books.google.com/books?hl=en&lr=&id=onoXxD1ytMkC&oi=fnd&ots=Oc1AXXAzOY&sig=WjnXZQDDSk_tZb-jbjjmKvgVo7w

[26] “Pintsuk: Tungsten as a plasma-facing material - Google Scholar.” https://scholar.google.com/scholar_lookup?title=Tungsten%20as%20a%20plasma-facing%20material&pages=551-581&publication_year=2012&author=Pintsuk%2CG. (accessed Dec. 14, 2021).

[27] P. Jenuš, A. Iveković, M. Kocen, A. Šestan, and S. Novak, “W 2 C-reinforced tungsten prepared using different precursors,” *Ceram Int*, vol. 45, no. 6, pp. 7995–7999, 2019, doi: 10.1016/j.ceramint.2018.11.187.

[28] L.-M. L. Xiao-Yue Tan Ze-Long Lu, Guang-Nan Luo, Xiang Zan, Ji-Gui Cheng, Yu-Cheng Wu, “Development of tungsten as plasma-facing materials by doping tantalum carbide nanoparticles,” *Powder Technol*, vol. 269, pp. 437–442, 2015.

[29] G. M. Song, Y. Zhou, and Y. J. Wang, “The microstructure and elevated temperature strength of tungsten-titanium carbide composite,” *J Mater Sci*, vol. 37, no. 16, pp. 3541–3548, 2002, doi: 10.1023/A:1016583611632.

[30] S. Novak *et al.*, “Beneficial effects of a WC addition in FAST-densified tungsten,” *Materials Science and Engineering A*, vol. 772, p. 138666, 2020, doi: 10.1016/j.msea.2019.138666.

[31] A. S. Kurlov and A. I. Gusev, *Tungsten Carbides: Structure, Properties and Application in Hardmetals*, vol. 184, no. 184. 2013. doi: 10.1007/978-3-319-00524-9.

[32] H. A. Wriedt, “The O-W (oxygen-tungsten) system,” *Bulletin of Alloy Phase Diagrams 1989 10:4*, vol. 10, no. 4, pp. 368–384, Aug. 1989, doi: 10.1007/BF02877593.

[33] I. Campbell, *High-temperature materials and technology.* New York: Wiley, 1967.

[34] Y. Li *et al.*, “Theoretical study on the stability, elasticity, hardness and electronic structures of W-C binary compounds,” *J Alloys Compd*, vol. 502, no. 1, pp. 28–37, Jul. 2010, doi: 10.1016/j.jallcom.2010.04.184.

[35] G. Gottstein, “Physical Foundations of Materials Science,” *Physical Foundations of Materials Science*, 2004, doi: 10.1007/978-3-662-09291-0.

[36] D. V. Suetin, I. R. Shein, and A. L. Ivanovskii, “Structural, electronic properties and stability of tungsten mono- and semi-carbides: A first principles investigation,” *Journal of Physics and Chemistry of Solids*, vol. 70, no. 1, pp. 64–71, Jan. 2009, doi: 10.1016/j.jpcs.2008.09.004.

[37] A. Bakaev, G. Bonny, N. Castin, D. Terentyev, and V. A. Bakaev, “Impact of interstitial impurities on the trapping of dislocation loops in tungsten,” *Scientific Reports 2021 11:1*, vol. 11, no. 1, pp. 1–11, Jun. 2021, doi: 10.1038/s41598-021-91390-1.

[38] G. Hachet, L. Ventelon, F. Willaime, and E. Clouet, “Screw dislocation-carbon interaction in BCC tungsten: an ab initio study,” *Acta Mater*, vol. 200, pp. 481–489, Nov. 2020, doi: 10.1016/J.ACTAMAT.2020.09.014.

[39] A. P. Sutton and R. W. Balluffi, *Interfaces in crystalline materials.* Oxford ;New York: Clarendon Press ;;Oxford University Press, 1995.

[40] “Electron Backscatter Diffraction in Materials Science Second Edition”, doi: 10.1007/978-0-387-88136-2.

[41] L. Priester, “Grain Boundaries,” vol. 172, 2013, doi: 10.1007/978-94-007-4969-6.

[42] P. Lejcek, “Grain Boundary Segregation in Metals,” vol. 136, 2010, doi: 10.1007/978-3-642-12505-8.

[43] E. S. Solntceva, M. L. Taubin, N. A. Bochkov, V. A. Solntsev, and A. A. Yaskolko, “Use of tungsten single crystals to enhance nuclear reactors structural elements properties,” *undefined*, vol. 41, no. 17, pp. 7206–7212, May 2016, doi: 10.1016/J.IJHYDENE.2016.02.019.

[44] I. R. Birss, “Helium production in reactor materials. Review paper,” *Journal of Nuclear Materials*, vol. 34, no. 3. North-Holland, pp. 241–259, Mar. 1970. doi: 10.1016/0022-3115(70)90192-3.

[45] H. B. Zhou, X. Ou, Y. Zhang, X. Shu, Y. L. Liu, and G. H. Lu, “Effect of carbon on helium trapping in tungsten: A first-principles investigation,” *Journal of Nuclear Materials*, vol. 440, no. 1–3, pp. 338–343, 2013, doi: 10.1016/j.jnucmat.2013.05.070.

[46] J. Xu, C. Wang, W. Zhang, C. Ren, H. Gong, and P. Huai, “Atomistic simulations of the interactions of helium with dislocations in nickel,” *Nuclear Materials and Energy*, vol. 7, pp. 12–19, May 2016, doi: 10.1016/J.NME.2016.02.007.

[47] E. E. Bloom, “The challenge of developing structural materials for fusion power systems,” *Journal of Nuclear Materials*, vol. 258–263, no. PART 1 A, pp. 7–17, Oct. 1998, doi: 10.1016/S0022-3115(98)00352-3.

[48] R. L. Klueh and M. P. Tanaka, “Steels for Fusion Reactor Applications,” *JOM 1985 37:10*, vol. 37, no. 10, pp. 16–23, Oct. 2012, doi: 10.1007/BF03258764.

[49] R. J. M. Konings and R. E. Stoller, “Comprehensive Nuclear Materials,” *Comprehensive Nuclear Materials: Second Edition*, pp. 1–4653, Jul. 2020, doi: 10.1016/c2017-1-02873-8.

[50] P. Cavaliere, B. Sadeghi, and A. Shabani, “Spark Plasma Sintering: Process Fundamentals,” *Spark Plasma Sintering of Materials*, pp. 3–20, 2019, doi: 10.1007/978-3-030-05327-7_1.

[51] J. A. Webb, I. Charit, and D. P. Butt, “Microstructural Evolution and Related Kinetics During Pulsed Electric Current Sintering of Tungsten,” *Spark Plasma Sintering of Materials*, pp. 265–289, 2019, doi: 10.1007/978-3-030-05327-7_10.

[52] Fritz. Thümmler, R. Oberacker, and E. Institute of Materials (London, “An introduction to powder metallurgy,” p. 332, 1993.

[53] R. L. Coble, “Sintering Crystalline Solids. I. Intermediate and Final State Diffusion Models,” *J Appl Phys*, vol. 32, no. 5, p. 787, Jun. 2004, doi: 10.1063/1.1736107.

[54] O. Guillon *et al.*, “Field-Assisted Sintering Technology/Spark Plasma Sintering: Mechanisms, Materials, and Technology Developments,” *Adv Eng Mater*, vol. 16, no. 7, pp. 830–849, Jul. 2014, doi: 10.1002/ADEM.201300409.

[55] Z. A. Munir, U. Anselmi-Tamburini, and M. Ohyanagi, “The effect of electric field and pressure on the synthesis and consolidation of materials: A review of the spark plasma sintering method,” *Journal of Materials Science 2006 41:3*, vol. 41, no. 3, pp. 763–777, Feb. 2006, doi: 10.1007/S10853-006-6555-2.

[56] J. R. Stephens, “EFFECTS OF INTERSTITIAL IMPURITIES ON THE LOW-TEMPERATURE TENSILE PROPERTIES OF TUNGSTEN.” Jun. 01, 1964.

[57] W. G. Fahrenholtz, E. J. Wuchina, W. E. Lee, and Y. Zhou, “Ultra-High Temperature Ceramics: Materials for Extreme Environment Applications,” *Ultra-High Temperature Ceramics: Materials for Extreme Environment Applications*, vol. 9781118700785, pp. 1–441, Nov. 2014, doi: 10.1002/9781118700853.

[58] J. P. Mercier, G. Zambelli, and W. Kurz, “Microstructures,” *Introduction to Materials Science*, pp. 239–259, 2002, doi: 10.1016/B978-2-84299-286-6.50016-0.

[59] S. M. Mukhopadhyay, “Sample Preparation for Microscopic and Spectroscopic Characterization of Solid Surfaces and Films,” *Sample Preparation Techniques in Analytical Chemistry*, pp. 377–411, Oct. 2003, doi: 10.1002/0471457817.CH9.

[60] A. Šestan *et al.*, “Non-uniform He bubble formation in W/W2C composite: Experimental and ab-initio study,” *Acta Mater*, vol. 226, p. 117608, Mar. 2022, doi: 10.1016/J.ACTAMAT.2021.117608.

[61] M. Kelemen *et al.*, “Micro-NRA and micro-3HIXE with 3He microbeam on samples exposed in ASDEX Upgrade and Pilot-PSI machines,” *Nucl Instrum Methods Phys Res B*, vol. 404, pp. 179–184, 2017, doi: 10.1016/j.nimb.2017.01.072.

[62] D. L. Bish and J. Edward. Post, “Modern powder diffraction,” p. 369, 1989.

[63] S. Rubino, S. Akhtar, P. Melin, A. Searle, P. Spellward, and K. Leifer, “A site-specific focused-ion-beam lift-out method for cryo Transmission Electron Microscopy,” *J Struct Biol*, vol. 180, no. 3, pp. 572–576, Dec. 2012, doi: 10.1016/J.JSB.2012.08.012.

[64] D. B. Williams and C. B. Carter, “Transmission electron microscopy: A textbook for materials science,” *Transmission Electron Microscopy: A Textbook for Materials Science*, pp. 1–760, 2009, doi: 10.1007/978-0-387-76501-3/COVER.

[65] J. R. M. Joseph Goldstein, Dale E. Newbury, David C. Joy, Charles E. Lyman, Patrick Echlin, Eric Lifshin, Linda Sawyer, *Scanning Electron Microscopy and X-ray Microanalysis: Third Edition*. Springer US, 2012. doi: 10.1007/978-1-4615-0215-9.

[66] J. Zavašnik, A. Šestan, and V. Shvalya, “Microscopic techniques for the characterisation of metal-based nanoparticles,” *Comprehensive Analytical Chemistry*, vol. 93, pp. 241–284, Jan. 2021, doi: 10.1016/BS.COAC.2021.02.006.

[67] C. A. Schneider, W. S. Rasband, and K. W. Eliceiri, “NIH Image to ImageJ: 25 years of image analysis,” *Nat Methods*, vol. 9, no. 7, pp. 671–675, 2012, doi: 10.1038/nmeth.2089.

[68] QGIS Development Team, “QGIS Geographic Information System. Open Source Geospatial Foundation Project. http://qgis.osgeo.org,” *Qgisorg*, 2014. http://www.qgis.org/

[69] A. Šestan, P. Jenuš, S. N. Krmpotič, J. Zavašnik, and M. Čeh, “The role of tungsten phases formation during tungsten metal powder consolidation by FAST: Implications for high-temperature applications,” *Mater Charact*, vol. 138, pp. 308–314, 2018, doi: 10.1016/j.matchar.2018.02.022.

[70] G. Lee, J. McKittrick, E. Ivanov, E. O.-I. J. of, and undefined 2016, “Densification mechanism and mechanical properties of tungsten powder consolidated by spark plasma sintering,” *Elsevier*.

[71] D. J. Palmer, P. G. Dickens, and IUCr, “Tungsten dioxide: structure refinement by powder neutron diffraction,” *urn:issn:0567-7408*, vol. 35, no. 9, pp. 2199–2201, Sep. 1979, doi: 10.1107/S0567740879008785.

[72] A. Šestan *et al.*, “Tungsten carbide as a deoxidation agent for plasma-facing tungsten-based materials,” *Journal of Nuclear Materials*, vol. 524, pp. 135–140, 2019, doi: 10.1016/j.jnucmat.2019.06.030.

[73] S. Chanthapan, A. Kulkarni, J. Singh, C. Haines, and D. Kapoor, “Sintering of tungsten powder with and without tungsten carbide additive by field assisted sintering technology,” *Int J Refract Metals Hard Mater*, vol. 31, pp. 114–120, Mar. 2012, doi: 10.1016/J.IJRMHM.2011.09.014.

[74] A. Šestan *et al.*, “Non-uniform He bubble formation in W/W2C composite: Experimental and ab-initio study,” *Acta Mater*, vol. 226, p. 117608, Mar. 2022, doi: 10.1016/J.ACTAMAT.2021.117608.

Bibliography

Publications Related to the Thesis

Journal articles

[1] A. Šestan, L. Sreekala, S. Markelj, M. Kelemen, J. Zavašnik, C. Liebscher, G. Dehm, T. Hickel, M. Čeh, S. Novak, and P. Jenuš, "Non-uniform He bubble formation in W/W_2C composite: Experimental and ab-initio study," *Acta Materialia*, vol. 226, p. 117608, 2022.

[2] A. Šestan, J. Zavašnik, M. Maček, M. Kocen, P. Jenuš, S. Novak, M. Čeh, and G. Dehm, "Tungsten carbide as a deoxidation agent for plasma-facing tungsten-based materials," *Journal of Nuclear Materials*, vol. 524, pp. 135–140, 2019.

[3] A. Šestan, P. Jenuš, S. N. Krmpotič, J. Zavašnik, and M. Čeh, "The role of tungsten phases formation during tungsten metal powder consolidation by FAST: Implications for high-temperature applications," *Materials Characterization*, vol. 138, pp. 308–314, 2018.

Other Publications

Journal articles

[1] J. Zavašnik, A. Šestan, and S. Škapin, "Degradation of asbestos – reinforced water supply cement pipes after a long-term operation," *Chemosphere*, vol. 287, p. 131977, 2022.

[2] D. Vengust, B. Jančar, T. Sever, A. Šestan, V. Bobnar, Z. Kutnjak, N. Daneu, D. Suvorov, M. Spreitzer, "Improved environmental stability of thermoelectric ceramics based on intergrowths of $Ca_3Co_4O_9$—$Na_{0.75}CoO_2$" *Ceramics international*, vol. 47, no. 8, pp. 11687-11693, 2021.

[3] S. Novak, M. Kocen, A. Šestan, A. Galatanu, M. Galatanu, S. Tarancón, E. Tejado, J. Y. Pastor, and P. Jenuš, "Beneficial effects of a WC addition in FAST-densified tungsten," *Materials Science and Engineering A*, vol. 772, p. 138666, 2020.

[4] S. Markelj, T. Schwarz-Selinger, M. Pečovnik, W. Chrominski, A. Šestan, and J. Zavašnik, "Deuterium transport and retention in the bulk of tungsten containing helium: The effect of helium concentration and microstructure," *Nuclear Fusion*, 60-10, 2020.

[5] P. Jenuš, A. Iveković, M. Kocen, A. Šestan, and S. Novak, "W_2C-reinforced tungsten prepared using different precursors," *Ceramics international*, vol. 45, no. 6, pp. 7995–7999, 2019,.

[6] D. Vengust, B. Jančar, A. Šestan, M. Ponikvar Svet, B. Budič, and D. Suvorov, "Chemical decomposition as a likely source of ambient and thermal instabilities of layered sodium cobaltate," *Chemistry of Materials*, vol. 25, no. 23, pp. 4791–4797, 2013.

Published scientific conference contribution

[1] A. Pačevski, J. Zavašnik, A. Šestan, A. Luković, I. Jelić, A. Kremenović, A. Zdravković, S. Erić, D. Bajuk-Bogdanović, "Micro-to nanoscale textures of ore minerals: methods of study and significance," *Proceedings,* XIII International Mineral Processing and Recycling Conference, MPRC, Grozdanka D. Bogdanović (ed.), Milan Trumić (ed.). 8-10 May 2019, Belgrade, Serbia, 2019.

Published scientific conference contribution abstract (invited lecture)

[1] S. Markelj, T. Schwarz-Selinger, M. Pečovnik, A. Šestan, W. Chromiński, "Influence of helium concentration and bubbles on deuterium retention and transport in the bulk of tungsten," *17th Internationa Conference on Diffusion in Solids and Liquids,* DSL2021, 28 June - 2 July, Malta, 2021.

[2] P. Jenuš, A. Iveković, M. Kocen, A. Abram, A. Šestan, S. Novak, "W_2C-reinforced tungsten: a promising candidate for DEMO divertor materials," *TMS 2021 Virtual: 150th annual meeting & exhibition:* Orlando, Florida, March 15-18, 2021.

[3] S. Markelj, T. Schwarz-Selinger, M. Pečovnik, M. Kelemen, J. Zavašnik, A. Šestan, "Influence of He concentration on duterium retention and transport in the bulk of tungsten," *Final program & abstracts of oral*, IBA 2019, 24th International Conference on Ion Beam Analysis, 13-18 October, Antibes, French riviers, pp. 101, 2019.

[4] A. Šestan, M. Kocen, J. Zavašnik, P. Jenuš, S. Novak, M. Čeh, "Effects of different sample preparation techniques of W-based composite for plasma-facing materials on electron microscopy characterization," *Andreja Gajović (ed.). Book of abstracts.* 13th Multinational Congress on Microscopy, September 24-29, Rovinj, Croatia. Zagreb: Ruđer Bošković Institute: Croatian Microscopy Society, pp. 101-103, 2017.

[5] P. Jenuš, A. Iveković, M.j Kocen, A. Šestan, J. Zavašnik, S. Novak, "Fabrication and characterization of W-W_2C nanocomposites: possible candidates for divertor," *Conference abstract book.* Nano-S&T, BIT's Annual World Congress of Nano Science & Technology-2016, October 26-28, 206, Singapore, Singapore, pp. 306, 2016

[6] B. Jančar, D. Vengust, G. Dražić, A. Šestan, D. Suvorov, "Integrown thermoelectric layered cobaltates," *Book of abstracts & souvenir.* Delhi: Janvani Prakashan Pvt. Ltd., pp. 39-40, 2014.

[7] B. Jančar, D. Vengust, G. Dražić, A. Šestan, D. Suvorov, "Integrown thermoelectric layered cobaltates," in: Dragan Uskoković (ed.), Velimir Radmilović (ed.). *Programme and the book of abstracts.* Sixteenth Annual Conference YUCOMAT 2014, Herceg Novi, Montenegro, September 1-5, Belgrade: Materials Research Society of Serbia, p.p. 12, 2014.

Published scientific conference contribution abstract

[1] S. Markelj, T. Schwarz-Selinger, P. Jenuš, A. Iveković, S. Novak, M. Kelemen, E. Punzón Quijorna, A. Šestan, A. Abram, "Deuterium retention in displacement damaged tungsten-based samples with tungsten carbide inclusions," *30th NENE 2021: 30th International Conference Nuclear Energy for New Europe, September 6-9, Bled,*

Slovenija: book of abstracts. Ljubljana: Društvo jedrskih strokovnjakov Slovenije: = Nuclear Society of Slovenia, pp. 95, 2021.

[2] S. Novak, P. Jenuš, M. Kocen, A. Abram, A. Šestan, S. Markelj, M. Kelemen, A. Galatanu, E. Tejado, J. Y. Pastor, G. Pintsuk, "WC as reinforcement for tungsten or matrix material for DEMO divertor," *Abstracts.* ICFRM-19, International Conference on Fusion Reactor Materials, October 27-November 1, La Jolla, California, 2019.

[3] P. Jenuš, M. Kocen, A. Abram, A. Šestan, A. Galatanu, M. Galatanu, S. Tarancón, E. Tejado, J. Y. Pastor, S. Novak, "W_2C-reinforced tungsten: a promising candidate for DEMO divertor armour material," *Book of abstracts.* PFMC2019, 17th International Conference on Plasma Facing Materials & Components for Fusion Applications, 20-24 May 20-24, Eindhoven, The Netherlands, 2019.

[4] A. Šestan, J. Zavašnik, S. Markelj, M. Kelemen, "Influence of He implantation and post-annealing on microstructure in tungsten matrix composites," *iPlasmaNano - X, September 15-20, Poreč, Croatia*, 2019.

[5] P. Jenuš, M. Kocen, A. Abram, A. Šestan, A. Galatanu, E. Tejado, J. Y. Pastor, M. Wirtz, G. Pintsuk, S. Novak, "W_2C-reinforced tungsten: a promising candidate for high-heat-flux material," *Scientific program.* 14th International Symposium on Fusion Nuclear Technology, ISFNT-14, 22-27 September, Budapest, Hungary, pp. 67, 2019.

[6] P. Jenuš, A. Šestan, M. Kocen, A. Galatanu, T. Garrido, E. M. Pastor, J. Ygnacio, S. Novak, "W_2C reinforced tungsten: thermo-mechanical and microstructural properties," *Book of abstracts.* 30th Symposium on Fusion Technology, September 16-21, Giardini Naxos, Sicily, Italy, pp. 672, 2018.

[7] M. Kocen, P. Jenuš, A. Šestan, S. Novak, "Layered W-WC composites prepared by FAST," *Book of Abstracts.* 30th edition of the Symposium on Fusion Technology (SOFT 2018), 16^{th} to 21^{st} September 2018, Giardini Naxos, Giardini Naxos: SOFT, pp. 414, 2018.

[8] M. Kocen, P. Jenuš, A. Šestan, S. Novak, "Capturing the Sun in a tungsten "box"," in: Miha Dežman (ed.), et al. *Zbornik = Proceedings.* 10. študentska konferenca Mednarodne podiplomske šole Jožefa Stefana in 12. dneva mladih raziskovalcev (Konferenca KMBO), 10. in 11. maj 2018, Ljubljana, Slovenija = 10th Jožef Stefan International Postgraduate School Students' Conference and 12th Young Researchers' Day 10th and 11th May, Piran, Slovenia. Ljubljana: Mednarodna podiplomska šola Jožefa Stefana: = Jožef Stefan International Postgraduate School: Inštitut Jožef Stefan: = Jožef Stefan Institute, pp. 50, 2018.

[9] A. Šestan, S. Markelj, M. Kelemen, M. Kocen, J. Zavašnik, P. Jenuš, S. Novak, M. Čeh, "Microstructural changes of W and W—W_2C composite due to He-implantation," *16th International Conference on Plasma-Facing Materials and Components, MC16, May 16th - 19th, Düsseldorf, Germany, 2017.*

[10] M. Kocen, P. Jenuš, A. Šestan, S. Novak, "Preparation and characterization of W-based composites for fusion application. In: *16th International Conference on Plasma-Facing Materials and Components*," MC16, May 16th - 19th, Düsseldorf, Germany, 2017.

[11] M. Kocen, P. Jenuš, A. Šestan, S. Novak, "Comparison of spark plasma and conventional sintering for consolidation of W-based composites for DEMO divertor," *Book of abstracts.* 26th International Conference Nuclear Energy for New Europe, NENE 2017, Bled, Slovenia, September 11-14, Ljubljana: Društvo jedrskih strokovnjakov Slovenije: = Nuclear Society of Slovenia, pp. 109, 2017.

[12] P. Jenuš, M. Kocen, A. Šestan, J. Zavašnik, S. Markelj, M. Kelemen, S. Novak, "Microstructural and mechanical characterization of W-based composites for DEMO divertor," in: *Book of abstracts.* 26th International Conference Nuclear Energy for New Europe, NENE 2017, Bled, Slovenia, September 11-14, Ljubljana: Društvo jedrskih strokovnjakov Slovenije: = Nuclear Society of Slovenia, pp. 116, 2017.

[13] P. Jenuš, A. Iveković, M. Kocen, A. Šestan, J. Zavašnik, S. Novak, "W—W_2C composites prepared with in-situ synthesis of W_2C nanoparticles from various," in: *NANOAPP 2017, Nanomaterials & Application,* 14-18 June, Bled, Slovenia, 2017.

[14] M. Kocen, P. Jenuš, S. Novak, A. Šestan, "Inhibition of W grain growth in W - based material for fusion application," in: M. Godec (ed.), et al. *Program in knjiga povzetkov = Program and book of abstracts.* 25. mednarodna konferenca o materialih in tehnologijah, 16.-19. oktober, Portorož, Slovenija = 25th International Conference on Materials and Technology, 16-19 October, Portorož, Slovenia, Ljubljana: Inštitut za kovinske materiale in tehnologije, pp. 96. 2017.

[15] P. Jenuš, A. Iveković, M. Kocen, A. Šestan, J. Zavašnik, S. Novak, "W_2C-reinforced W prepared with in-situ synthesis of W_2C nanoparticles from various carbon source," *Scientific program*, 13th International Symposium on Fusion Nuclear Technology, ISFNT-13, September 25-29, Kyoto, Japan, 2017.

[16] M. Kocen, P. Jenuš, A. Šestan, S. Novak, "Tungsten-based composite for extreme environments in fusion reactor," in: Majda Pavlin (ed.), et al. *Zbornik = Proceedings.* 9. študentska konferenca Mednarodne podiplomske šole Jožefa Stefana in 11. dan mladih raziskovalcev (Konferenca KMBO) = 9th Jožef Stefan International Postgraduate School Students' Conference and 11th Young researchers' Day, 19.-20. 4., Ljubljana, Slovenija, Ljubljana: Mednarodna podiplomska šola Jožefa Stefana: = Jožef Stefan International Postgraduate School: Inštitut Jožef Stefan: = Jožef Stefan Institute, pp. 53, 2017.

[17] A. Šestan, J. Zavašnik, A. Iveković, M. Kocen, S. Novak, M. Čeh, "TEM investigation of W-based composite as plasma-facing material (PFM)," S. Prpar Mihevc (ed.), M. Prunk (ed.), J. Pungerčar (ed.), *10th Young researchers' day, 31 March, Ljubljana: program and abstract book.* Ljubljana: Institut Jožef Stefan, pp. 44, 2016.

[18] A. Šestan, S. Markelj, M. Kelemen, M. Kocen, J. Zavašnik, P. Jenuš, S. Novak, M. Čeh, "Microstructural changes of W and W—W_2C composite due to He-implantation," *16th International Conference on Plasma-Facing Materials and Components, MC16, May 16th - 19th, Düsseldorf, Germany, 2017.*

[19] A. Šestan, M. Kocen, J. Zavašnik, S. Novak, P. Jenuš, M. Čeh, "Synthesis of W-base composite as a plasma facing material," *Book of abstracts.* 25th International Conference Nuclear Energy for New Europe, NENE 2016, Portorož, September 5-8, pp. 61, 2016.

[20] S. Novak, P. Jenuš, A. Iveković, M. Kocen, A. Šestan, J. Zavašnik, "Tungsten carbide particles-reinforced tungsten for divertor," *Book of abstracts.* 29th Symposium on Fusion Technology, SOFT 2016, September 5-9, 2016, Prague, Czech Republic, p. p. 439, 2016.

[21] A. Šestan, J. Zavašnik, P. Jenuš, S. Novak, M. Čeh, "Microstructure characterization of reinforce W-composite as plasma facing material," Matjaž Godec (ed.), et al. *Program in knjiga povzetkov = Program and book of abstracts.* 24. mednarodna konferenca o materialih in tehnologijah, 28.-30. September 2016, Portorož, Slovenija = 24th International Conference on Materials and Technology, 28-30 September 2016, Portorož, Slovenia. Ljubljana: Inštitut za kovinske materiale in tehnologije, pp. 201, 2016.

[22] A. Šestan, S. D. Škapin, V. Žunič, "TEM specimen preparation of the micrometre-sized anatase particles in order to observe their internal structure," *Book of tutorials and abstracts.* EMAS 2015, 14th European Workshop on Modern Developments and Applications in Microbeam Analysis, Portorož, Slovenia, 3 to 7 May 2015, Antwerpen: EMAS, pp. 397, 2015.

[23] A. Šestan, M. Gec, B. Jančar, "Hydrothermal synthesis of twin-based multiply branched rutile-type TiO_2," *Microscopy for global challenges: touching atoms, molecules, nanostructures and cells by multidimensional microscopy.* 18th International Microscopy Congress, 7-12 September 2014, Prague Czech Republic, pp. 1, 2014.

[24] B. Jančar, D. Vengust, G. Dražić, A. Šestan, D. Suvorov, "Intergrow structures of thermoelectrics cobaltates," *Program and abstracts book.* 9th Asian Meeting on Ferroelectricity, Asian Meeting on Electroceramics, AMF-AMEC-2014, October 26-30, 2014, Shanghai, China, pp. 116, 2014.

[25] B. Jančar, D. Vengust, A. Šestan, V. Bobnar, Z. Kutnjak, D. Suvorov, "Low-thermal-conductivity oxide thermoelectrics based on coherently intergrown cobaltates," *E-MRS 2013 spring meeting and exhibit.* Warrendale: Materials Research Society, 2013.

[26] B. Jančar, D. Vengust, A. Šestan, M. Logar, M. Maček, D. Suvorov, "Chemical peculiarities of $Na_{0.75}CoO_2$," *Book of abstracts: poster presentation.* ICT/ECT 2012, The 31st International & 10th European Conference on Thermoelectrics, July 9th-12th, 2012, Aalborg, Denmark, pp. 149, 2012.

[27] D. Vengust, A. Šestan, B. Jančar, D. Suvorov, "Degradation of sodium cobaltate under ambient conditions," *Book of abstracts: poster presentation.* ICT/ECT 2012, The 31st International & 10th European Conference on Thermoelectrics, July 9th-12th, 2012, Aalborg, Denmark, pp. 164, 2012.

[28] B. Jančar, D. Vengust, A. Šestan, M. Logar, D. Suvorov, "The chemistry of sodium cobaltate. In: *E-MRS 2012 Spring Symposium X: May 14th-18th 2012, Strasbourg, France.* Strasbourg: European Materials Research Society, 2012.

[29] B. Jančar, D. Vengust, A. Šestan, "Chemical peculiarities of layered sodium cobaltates," *Proceedings of the 9th European Conference on Thermoelectrics, 9th ECT, September 28-30, 2011, Thessaloniki, Greece.* New York: American Institute of Physics, 2012. AIP conference proceedings, vol. 1449, 2012.

[30] A. Šestan, D. Vengust, B. Jančar, D. Suvorov, "Degradation of layered sodium cobaltate," in: M. Godec (ed.). *Program in knjiga povzetkov = Program and book of abstracts.* 19. konferenca o materialih in tehnologijah, 22. - 23. november, Portorož = 19th Conference on Materials and Technology, 22-23 November, Portorož, Slovenia. Ljubljana: Inštitut za kovinske materiale in tehnologije, pp. 80, 2011.

Independent scientific component part or a chapter in a monograph

[1] J. Zavašnik, A. Šestan, and V. Shvalya, "Microscopic techniques for the characterisation of metal-based nanoparticles," Comprehensive Analytical Chemistry, vol. 93, pp. 241–284, Jan. 2021.

Biography

EDUCATION

- 2015-present: PhD student in Nanosciences and Nanotechnologies, Jožef Stefan International Postgraduate School, Slovenia,
- 2003-2010: B. Sc. in Chemistry and Chemical Engineering, University of Ljubljana, Slovenia (title: Mikrostrukturne karakteristike materialov na osnovi Ni-GDC in GDC pripravljenih po citratno nitratnem zgorevalnem postopku).

PROFESSIONAL POSITIONS HELD

- 2014-present: *technical associate*, Centre for Electron Microscopy and Microanalysis, Jožef Stefan Institute (on maternity leave from May 2019 - May 2020),
- 2017-2018: *guest scientist*, Max-Planck-Institut für Eisenforschung (MPIE), Düsseldorf, Germany,
- 2010-2013: *technical associate*, Advanced Materials Department, Jožef Stefan Institute.

RESEARCH FELLOWSHIPS

- 2017-2018: Erasmus^{+} Student mobility for traineeships: Max-Planck-Institut für Eisenforschung (MPIE), Düsseldorf, Germany,
- 2015-present: Eurofusion scholarship: The Education work package - WPEDU, EUROfusion.

AWARDS

- 2010: Diploma award for exceptional academic achievement, contributed to the sustainable development of the society in the Republic of Slovenia.

PROFESSIONAL TRAINING

- 2015 – Introduction to EDS/WDS X-Ray microanalysis and EBSD (workshop), Ljubljana, Slovenia,
- 2014 – Advanced techniques in TEM sample preparation (training), Prague, Czech Republic.

RESEARCH PROJECTS

- 2021 – 2026: *project group leader* on Max-Planck-Gesellschaft awarded project Extreme Energy Materials (https://www.mpie.de/4581684/extreme_energy_materials) (https://www.mpie.de/4580830/new-partner-group-on-high-performance-materials),
- 2021 – 2024: *researcher* on EUROfusion project Detection of defects and hydrogen by ion beam analysis in channelling mode for fusion – DeHydroC (https://f2.ijs.si/en/projects/20211021115250844/detection-of-defects-and-hydrogen-by-ion-beam-analysis-in-channelling-mode-for-fusion-%E2%80%93-dehydroc),
- 2019 – 2021: *co-PI* (principal investigator) of a bilateral project between IJS and Max-Planck-Institut für Eisenforschung (Germany): Investigation of Helium retention in plasma facing materials using advanced analytical methods (BI-DE/19-20-002),
- 2018 – 2019: *co-PI* of a bilateral project between IJS and University of Belgrade (Serbia): Micro- to nanoscale textures of ore minerals: methods of study and significance (BI-RS/18-19-035).